Gap statistics and density crossovers in confined particles with power-law interactions

A Thesis

Submitted to the

Tata Institute of Fundamental Research, Mumbai

Subject Board of Physics

for the degree of Doctor of Philosophy

by

Saikat Santra

International Centre for Theoretical Sciences

Tata Institute of Fundamental Research

September, 2024

Final version submitted on January, 2025

DECLARATION

This thesis is a presentation of my original research work. Wherever contributions of others are involved, every effort is made to indicate this clearly, with due reference to the literature, and acknowledgment of collaborative research and discussions.

The work was done under the guidance of Professor Anupam Kundu at the International Centre for Theoretical Sciences, Tata Institute of Fundamental Research, Bengaluru. Professor Manas Kulkarni served as co-supervisor.

Saikat Santra
28-01-2025
Saikat Santra

In my capacity as the formal supervisor of record of the candidate's thesis, I certify that the above statements are true to the best of my knowledge.

Anupam Kundu

Anupam Kundu

Date: 28/01/2025

ACKNOWLEDGEMENTS

First and foremost, I sincerely thank my supervisor, Prof. Anupam Kundu for guiding me through every step of my PhD journey, from giving presentations to writing papers. He dedicated a significant amount of time to this and I have learned a great deal from him that will benefit my future research career. I am also grateful to him for involving me in several interesting projects during my time at ICTS. Additionally, my co-supervisor, Prof. Manas Kulkarni provided valuable guidance and supervision. He involved me in many fascinating projects and his regular check-ins were essential for keeping me on track.

Besides my supervisors, Prof. Abhishek Dhar had a great impact on my research by pointing out key details and correcting mistakes during our discussions, which was very helpful for writing and explaining my work. Prof. Chandan Dasgupta's experience in physics helped me avoid unnecessary explorations. I also appreciate Prof. Adhip Agarwala and Prof. Subhro Bhattacharjee for their guidance during my first project, where I was introduced to research. Adhip's ability to simplify difficult problems was particularly impressive. Special thanks go to Prashant Singh for his support on projects unrelated to my thesis work, which introduced me to the broad area of stochastic processes.

My batchmates—Jitendra, Saurav, Chandramouli, Aditya Sharma, Saumav, Pabitra, Praneet, Arko, Biprarshi, Basudeb, Junaid, Divya, Srasti, Aditya Vijaykumar, Sarthak, Tuneer, Priyadarshi, Shivam, Omkar, Bhanu, Mahaveer, Anup, Souvik, Udeepta, and Mukesh— were incredibly supportive. I have learned a lot from them, both academically and personally. During our coursework, the discussions on the green boards significantly enhanced my understanding of the subjects, thanks to Jitendra, Saurav, Aditya Sharma, Praneet, and Pabitra. Learning from talented juniors, especially Godwin, Rajarshi, Tamoghna, Alan, and Bikram further enriched my understanding of physics. I am especially grateful to Jitendra who consistently helped me with both numerical and theoretical problems. Finally, I want to thank all my friends, juniors, and seniors at ICTS for keeping a positive academic environment throughout my PhD journey.

The academic office staff— Jeeva, Pavana, Deepali, Nidhi, and Veena deserve recognition for their prompt assistance with academic tasks, from securing signatures from my mentor to getting extensions for completing my PhD. Their efficiency allowed me to focus on my research without worrying about these details. I also want to thank Jenny

in the administration office for her impressive handling of administrative matters.

Gratitude is also due to the ICTS Director, Prof. Rajesh Gopakumar, for supporting my academic travels with the Director's Excellence Grant. I also appreciate Prof. Anupam Kundu and Prof. Abhishek Dhar for additional financial support through their Knowledge Excellence Grant and J. C. Bose Grant respectively. I am grateful to the entire accounts team at ICTS for handling matters related to my salary, and travel grants efficiently. Madhulika, Ramya, and Ashwini were particularly helpful in these tasks.

List of Figures

1.1 Schematic representation of a 1D system with five particles, illustrating all-to-all interactions as described in Eq. (1.3). Each particle is connected to every other particle via dashed blue lines, indicating that all particles are interacting with each other. 23

1.2 Schematic representation of a 1D system with five particles, illustrating short-ranged interactions as described in Eq. (1.7) with $d = 2$. Each particle can interact with up to two particles on its left and two on its right, if available. Interactions are depicted by connecting lines between particles; a line indicates that the particles are interacting, while the absence of a line indicates no interaction. For example, the first (leftmost) particle can only interact with the second and third particles, but not with the fourth or fifth. In contrast, the third particle can interact with all particles shown, as it has two particles on either side. 27

2.1 Schematic phase diagram of the behavior of the gap distribution. We find four regimes in $k \in (-2, \infty)$, where the gap distribution has different scaling properties. In the region $(-2, -1) \cup (0, \infty)$ the scaling limit is achieved by using mean and the variance of gap only. The scaling function for $k \in (-2, -1) \cup (1, \infty)$ is Gaussian whereas it is non-Gaussian in $k \in (0, 1)$. In the regime $k \in (-1, 0)$ we are unable to obtain a scaling limit. . 35

2.2 Mean (left) and variance (right) of mid gap as a function of system size for $k = 2(\bullet), 1.5(\circ), 0.5(\square), 0^{+}(\blacksquare), -0.5\ (\blacktriangle), -1(\blacktriangledown)$ and $-1.5(*)$. Solid lines correspond to their corresponding power-law fitting (Eq. 2.9). The slopes in (a) are $a_k = 0.5, 0.57, 0.6, 0.5, 0.33, 0, -1$ and in (b) are $b_k = 2, 1.97, 1.42, 1, 0.63, 0, -1$, for decreasing k. These are consistent with Eq. (2.8) and Eq. (2.9) as elucidated in Fig. 2.3. The error bars are negligible [98]. In (a) the data for $k = -1.5$ is scaled by a factor 500. A total number of $\sim 10^8$ MC samples are used for the computations. 36

2.3 Comparison of the exponents a_k and b_k (symbols) obtained from simulations (MC), from MH and FT calculations, with Eqs. (2.8) (dashed line) and (2.9) (dotted line). In the inset we plot $\left(a_k - \frac{b_k}{2}\right)$ which quantifies the relative fluctuations $\sigma_\Delta/\langle\Delta\rangle$ in the MC data. To extract b_k the largest system sizes used were $N = 2048$ for MC, 4096 for MH and 16384 for FT. All the error bars are smaller than the point symbols [98]. 37

2.4 Schematic description of the discretization of the integral in the action $\delta\Sigma$. 41

2.5 Comparison of actual values of the variance of mid-gap calculated using all three techniques, MC, MH and FT for $\beta = 1$. 43

2.6 Plot of distributions $P_N(s)$ for different values of k and N. Except for the 1DOCP (b) and log-gas (d), for other values of k, we do not see convergence in N which naturally implies that it is different from $P_2(s)$ and hence there is no generalization of WS. 44

2.7 Plot of $\tilde{P}_N(\tilde{s})$ for different values of k and N. The distributions for $k = \pm 1.5$ are fitted with a Gaussian over two standard deviations (insets). This is generally observed for $k \notin [-1, 1]$. The distributions for $k = \pm 0.5$ are very different from Gaussian and this is generally the case for $k \in [-1, 1]$. 46

2.8 Relative fluctuations $\frac{\sigma_{\Delta_i}}{\langle\Delta_i\rangle}$ are shown as a function of i for different system sizes N as well as for different k in the regime $-1 \leq k \leq 0$ for two different system sizes ($N = 256$ in pink solid line and $N = 512$ in blue dashed line). For -1 < k < 0, from our numerics we find that $a_k - b_k/2$ is slightly different from zero, possibly due to finite size effects, hence we get a system size dependence in the relative fluctuation as well. (Inverse temperature β is taken to be unity.) 47

2.9 The distributions of the i-th normalized gap $p_N^{(i)}(s) = \langle\delta(s - s_i)\rangle$ are shown in the regime $-1 \leq k \leq 0$. It is clear that $p_N^{(\mathrm{i})}(s)$ is independent of i. In these figures we have taken $N = 256$ at inverse temperature $\beta = 1$. 48

2.10 Comparison of the level spacing distribution using 'picket fence (PF)' approximation and the actual distribution using Monte-Carlo simulation (MC). The distribution using PF approximation is fitted with the Eq. (2.31) (Fit) with parameters $A = 410.354, B = 1.160, C = 4.441$. We observe that there is no convergence of the actual level spacing distribution (MC) with system size. (Inverse temperature β is taken to be unity.) 49

3.1 Demonstration of the crossover in the density profiles in (a) 1DOCP and (b) log-gas systems. For both the systems we plot the scaled density profile $\tilde{\varrho}_f(y) = N^\alpha \varrho_N(yN^\alpha)$ as functions of y [see Eq. (3.11)] for eight values of $f = n/8$ with $n = 1$ (red), 2 (dark-green), 3 (blue), 4 (brown), 5 (green), 6 (dark-pink), 7 (black), and 8 (violet). For 1DOCP model, the profile transitions from a flat profile at $f = 1$ to a delta function profile in the $f \to 0$ limit. The peaks of the delta functions on the z-axis are cut in order to display the features of the density profiles for f close to 1. For the log-gas, the density profile changes its shape [shown in figure (b)] from Wigner semi-circle at $f = 1$ to bell-shaped at small f. For both cases we observe that the total support of the density profile decreases as f is reduced. The plots of density profiles are obtained numerically for $N = 128$ for both systems. Details of the numerical simulation are provided in A.1. 57

3.2 Plots of numerically obtained density profiles (dashed lines) for (a) $f = \frac{9}{16}$ and (b) $f = \frac{3}{4}$ in 1DOCP. Collapse of data for different N verifies the scaling relation in Eq. (3.11) with $\alpha = 1$. The solid green lines represent the analytical prediction in Eq. (3.12). We observe good agreement between simulation and theory. With decreasing f, the size of the central region reduces and the edge regions grow. 62

3.3 (a) System size collapse of scaled density $\tilde{\varrho}_f(y) = N\varrho_N(x)$ for 1DOCP at $f = 7/16$. Data collapse for different N verifies the scaling relation in Eq. (3.11) with $\alpha = 1$ over almost the full range except for a small region around the origin. The green solid line represents a uniform profile on both the left and right edge parts, as described by Eq. (3.13). The inset displays a zoomed version of the central part, where we observe that under scaling $y = x/N$ the density profile for larger N becomes sharper and narrower which is consistent with the delta function in Eq. (3.13). (b) This figure plots the density profile in the central part [zoomed version of delta part in (a)] as functions of unscaled variable x for different N. We observe that the density profile in the central part approaches, with increasing N, to a Gaussian form as given in Eq. (3.32). Simulation data are obtained using $\beta = 1$. 66

3.4 These plots show system size collapse of the numerical density profiles (dashed lines) for different N in the log-gas model for (a) $f = \frac{3}{4}$ and (b) $f = \frac{7}{8}$. The good collapse verifies the scaling $\varrho_N(x) = \frac{1}{\sqrt{N}}\tilde{\varrho}_f(x/\sqrt{N})$ in Eq. (3.11). The solid green line plots the scaling function $\tilde{\varrho}_f(y)$ as given in Eq. (3.14). We observe good agreement between simulation and theory in the central regime (represented by solid black vertical lines at $y = \pm\tilde{\ell}$). Outside this regime, the agreement between theory and simulation is better for f close to one and declines as f is reduced from one. 69

3.5 Comparison of numerically obtained (scaled) density profiles for different system sizes (dashed lines) with the analytical predictions (green solid lines) for log-gas (a) with $f = 1/8$ and (b) with $f = 1/16$. Once again collapse of numerical data for different N verifies the scaling in Eq. (3.11) with $\alpha = 1/2$. The theoretical prediction for the form of the scaled density profile $\tilde{\varrho}_f(y)$ inside the central part $(-\tilde{\ell}, \tilde{\ell})$ is Gaussian as in Eq. (3.15) [for log-gas]. The central region $(-\tilde{\ell}, \tilde{\ell})$ (represented by two vertical solid black lines) can be found from the relation $\int_{-\tilde{\ell}}^{\tilde{\ell}} \tilde{\varrho}_f(y)dy = 1-2f$. Outside the central region, the equilibrium density profile $\tilde{\varrho}_f(y)$ is different from the central part and its approximate analytical formula is provided in Eq. (3.16). Although agreement between the analytical formula [Eq. (3.16)] for the density and the numerical density profile reduces as f is increased from zero, however, it captures the total support of the density profile quite accurately. 72

4.1 The total (scaled) density profiles $\tilde{\rho}(z)$ for different (small) system sizes with several values of the activity, $a = 0.01$ in (a), 0.1 in (b) and 1.0 in (c) show the crossover: from sharply peaked density profile in (a) at very small activity to bell-shaped density profile in (c) at very large activity via an intermediary WSc profile in (b). For all the panels, the flipping rate γ is kept fixed at 1. 84

4.2 The transition in the (scaled) density profile $\tilde{\rho}(z)$ is shown once again with the same set of parameters as in Fig. 4.1, but now for large system sizes. In (a), where the activity parameter $a = 0.01$, the peaks in the density profile smooth out with increasing system sizes, and the numerically obtained density profile approaches the WSc density profile. In the middle panel (b) with an activity parameter of $a = 0.1$, the density profile in the bulk approximately matches the WSc form but deviates at the edges. The deviation from the WSc profile increases with system size. The form as well as the support of the density profile has changed significantly in (c) with $a = 1.0$. The density forms a bell-shaped profile extending approximately to $[-aN, aN]$ (depicted separately in Fig. 4.3). However, it is important to note that the $\sqrt{N}$ scaling in the density profile remains consistent throughout the bulk. 85

4.3 Showing the total support of the density profile $\rho(x)$ approximates to $[-aN, aN]$ in the large activity limit. The steady-state density profiles are drawn as a function of x/N for three different system sizes which seem to converge and show a sharp drop at $x = aN$. Near the edges, the density profiles (dashed lines) decay as $\sim 1/x^3$ (red solid line). 86

4.4 Showing the crossover from a 'crystal' to 'liquid' in a system of 64 particles because of reducing the flip rate γ keeping the activity parameter a fixed at 0.025. For the system size $N = 128$ with $a = 0.025$, the system has already crossed over to the liquid state characterized by a smooth density profile. 87

4.5 Demonstration of the emergence of wing-like structures in the density profile within the strongly active region ($a = 0.25$) as a result of the reduced flipping rate, γ. 87

4.6 Numerically computed Lindemann's ratio η_i (points) as a function of i/N for different values of the flipping rate γ within a system comprising $N = 64$ particles. Three panels correspond to three different values of the speed v_0, $0.32, 0.64$ and 1.6 in (a),(b) and (c) respectively. Additionally, we have drawn a solid black (horizontal) line at 0.5 indicating the cases where the standard deviation of particle positions becomes exactly equal to 50% of the average distance to the nearest neighbor. For a quantitative distinction between the 'crystal' and 'liquid' phases, we use this as a reference line above which we consider the system to be in the 'liquid' phase and below which is in the 'crystal' phase. In the first two panels, the system remains in the 'crystal' phase regardless of the γ values analyzed. However, in the third panel with speed $v_0 = 1.6$, the system stays in the 'crystal' phase for higher values of γ ($\gamma \gtrsim 1$). Conversely, for smaller γ values ($\lesssim 0.5$), the Lindemann's ratio exceeds 0.5 at the center, indicating a 'liquid' phase. . 88

4.7 Lindemann's ratio η_i as a function of i/N for different values of the flipping rate γ is shown in Fig. 4.6, now within a system comprising $N = 128$ particles. Similar to the scenario of $N = 64$ in this case, the system remains in the 'crystal' phase for $v_0 = 0.32$ and 0.64 across all values of γ and shifts to the 'liquid' phase for $v_0 = 1.6$ when $\gamma \lesssim 0.5$. 89

4.8 Lower diagram depicts three distinct 'phases' in the active CM model within the parameter space represented by a and $1/\gamma$, with red, blue, and black points representing weakly active, intermediate and strongly active regimes respectively. Red points signify scenarios where Lindemann's ratio η_i at the center of the trap ($i = N/2$) is less than 0.5 (see Fig. 4.7). Blue points represent intermediate active regions where the Lindemann's ratio at the trap center exceeds 0.5, but the values of χ defined in Eq. (4.9) remain below 0.1 (see Table. 4.1). The strongly active regime (indicated by black points) corresponds to cases where the value of χ exceeds 0.1. Density profiles in the corresponding regimes are shown schematically in the top panels. Two different system sizes are represented: circles (○) correspond to $N = 64$, while triangles (▲) represent $N = 128$. Notice that the second transition (from blue to black) occurs at $a \sim \mathcal{O}(1)$, which is independent of N. In contrast, the first transition (from red to blue) occurs at a values that depend on N, as depicted by two schematic (dashed) lines for the different system sizes. 90

4.9 Numerically computed variance of particle positions $s_i^2 \equiv \langle x_i^2 \rangle - \langle x_i \rangle^2$ (points) in the steady-state of active CM model for different values of the flipping rate γ keeping the activity parameter a fixed at 0.05 in (a), 0.1 in (b) and 0.5 in (c) for the system size $N = 64$. The dashed blue line represents our theoretical expectation given in Eq. (4.33). In the first two panels, the matching between numerical and analytical results becomes more and more promising as the flipping rate γ is reduced from 1. However, in the last panel where the activity is very high, the approximation used in the theoretical calculation is not valid. Therefore, the theoretical formula is no longer correct. 94

4.10 Variance of the gap g_n^2 as defined in Eq. (4.45), is plotted as a function of n for two different values of the activity parameters, $a = 0.01$, 0.05, and 0.1, in panels (a), (b) and (c) respectively, within a system of 128 particles for three different choices of the flipping rate γ. The points represent the numerically computed variance of the gap, while the solid lines indicate the corresponding theoretical expectations given by Eq. (4.46) with $i = N/2$. The red dashed line represents the approximated theoretical form of g_n^2 given in Eq. (4.45) obtained in the $\gamma \to 0$ limit. For small values of n, the numerical results show good agreement with the theoretical predictions. . 100

A.1 This figure demonstrates how the density profiles change from one shape to another as f is reduced from 1 to 0 for four representative values of k: (a) $k = 1.5$, (b) $k = 0.5$, (c) $k = -0.5$ and (d)$k = -1.1$, chosen from the following ranges $k > 1$, $0 < k < 1$, $-1 < k < 0$ and $-2 < k < -1$. For each case except $k = -1.1$, we have plotted scaled density profiles $\varrho_f(y)$ for 8 values of f: $f = n/8$ with $n = 8, 7, ..., 1$ (from violet to red). To avoid congestion, for $k = -1.1$ we show density profiles only for five values of f corresponding to $n = 8, 7, 5, 4$ and 3 (from violet to blue). For $k = 1.5$ there is neither a change in the support nor in the shape. For $k = 0.5$, with decreasing f the repulsion among the particles reduces which causes them to gather near the centre of the trap. Consequently, the profile get squeezed from a dome shape at $f = 1$ to a hill shape at $f \to 0$. For $k = -0.5$, the equilibrium density profile changes drastically as compared to the previous two cases. The profile shows a crossover from a dome-shaped profile at $f \to 1$ limit to a bell-shaped profile at $f \to 0$. Near $f = 0$, the peaks of the bell-shaped profiles on the z-axis are cut in order to display the features of the density profiles for f close to 1. For $k = -1.1$, the density profile changes from a 'U' shaped profile at $f = 1$ to a bell-shaped profile at $f = 0$ passing through different other interesting shapes at intermediate values of f. 128

List of Tables

3.1 A table summarising the status of our results. The * in the second row indicates the fact that for $0 < f < 1/2$ the entropy can contribute in the central part of the density profile in the 1DOCP model. However the central region $[-\ell_N, \ell_N]$ shrinks to a point in terms of scaled variable $y = x/N$ in the $N \to \infty$ limit since $\ell_N \sim \sqrt{\log N}$ [see Eq. (3.30)]. 74

4.1 Table showing the values of χ (defined in Eq. (4.9), which measures the deviation of the steady-state density profile from the Wigner semi-circle profile, for system sizes $N = 64$ and 128. The table includes results for various combinations of the tumbling rate γ and the activity parameter a $(= v_0/N)$. By applying a cutoff of $\chi = 0.1$ to distinguish the transition from the intermediate activity region to the strongly active region, we observe that this transition is independent of system size. 91

A.1 System size dependence of the matrix elements M_{ij} and H_{ij} for different values of i and j. As we are interested mainly in the bulk part of the system we ignore such terms where $(i - j) \sim \mathcal{O}(N)$. 108

A.2 System size dependence of the matrix elements M_{ij}^{-1} and H_{ij}^{-1} for different values of i and j. Again we ignore such terms where $(i - j) \sim \mathcal{O}(N)$. . . 109

Contents

1 Introduction **21**

2 Gap statistics for confined particles with power-law interactions **31**

2.1 Results for mean and variance of bulk gap 35

2.2 Microscopic Hessian (MH) 37

2.3 Quadratic field theory (FT) 39

2.4 Results for distribution of gap 45

2.5 Interesting aspects of the gap statistics for $-1 \leq k \leq 0$ 46

2.6 Spacing distribution in the Calogero-Moser system 48

2.7 Summary and outlooks 49

3 Crossover in densities of confined particles with finite range of interaction **51**

3.1 Definitions and relevant previous results 54

3.1.1 Equilibrium density profile in the ATAC case ($d = N - 1$ *i.e.*, $f = 1$) 56

3.1.2 Equilibrium density profile in SR case ($d \sim \mathcal{O}(1)$ *i.e.*, $f = 0$) . . . 56

3.2 Summary of the results 57

3.3 Density crossover in 1DOCP ($V(x) = -|x|$) 60

3.3.1 Solution for $1/2 \leq f \leq 1$: 60

3.3.2 Solution for $0 < f < 1/2$: 61

3.4 Density crossover in log-gas ($V(x) = -\log|x|$). 67

3.4.1 Solution for f close to 1: 67

3.4.2 Solution for f close to 0: 69

3.5 Summary and outlook 74

4 Crystal to liquid cross-over in the active Calogero-Moser model 77

4.1 Model, observables and the summary of our findings 79

4.2 Density profile 83

4.2.1 Weakly active 83

4.2.2 Intermediate activity: 84

4.2.3 Strongly active 85

4.2.4 Discussion of crossovers 88

4.3 Variance and covariance of the particle displacements 91

4.3.1 Inverting the Hessian matrix $\mathbf{H}_{\mathrm{CM}}$ 93

4.3.2 Variance and covariance of particle positions in the large N limit . 95

4.3.3 Variance of interparticle distance 99

4.3.4 Validity of the approximation 100

4.4 Summary and outlook 101

5 Conclusions 103

A Appendix 107

A.1 Numerical details 107

A.2 System size scaling of the matrix elements M and H 108

A.3 Field theoretic description of FR Riesz gas and the derivation of the saddle point equations 109

A.3.1 For $1/2 \leq f \leq 1$: 111

A.3.2 For $0 < f < 1/2$ 113

A.4 Explicit solution of the saddle point equation for FR 1DOCP 115

A.4.1 The saddle point calculation for $1/2 \leq f \leq 1$: 115

A.4.2 The saddle point calculation for $0 < f < 1/2$: 118

A.5 Crossover in the density profiles in Riesz gas models for other values of k 126

Bibliography 127

Publications 145

Abstract: We consider the $N-$particle classical Riesz gas confined in a one-dimensional external harmonic trap. The constituent particles interact via pairwise repulsive power-law interaction potential of the form $\sim 1/r^k$, with r being the distance between two particles. In the first part of my thesis, we study the fluctuations in the system at thermal equilibrium by looking at the statistics of the gap between successive particles. This quantity is analogous to the well-known level-spacing statistics which is ubiquitous in several branches of physics. We show that the variance of bulk gap goes as N^{-b_k} and find the k dependence of b_k via direct Monte-Carlo simulations. We provide supporting arguments based on microscopic Hessian calculation and a quadratic field theory approach. We compute the gap distribution and study its system size scaling. In the second part of my thesis, we consider a generalized version of the Riesz gas where each particle can interact with a maximum of d neighboring particles on either side (left or right), if available. As suggested by prior studies, the equilibrium density profile of these particles is expected to undergo shape variations as d is changed. In this part, we investigate the crossover by tuning the parameter f (where $f = d/N$) from 1 to 0 in the large N limit, for two distinct interaction potentials: $V(x) = -|x|$ and $V(x) = -\log(|x|)$. These potentials correspond to the well-known 1-D one-component plasma ($k = -1$) and Dyson's log-gas ($k = 0^+$) respectively. We explicitly show the crossover by analytically computing the average density profile for any $f \in (0, 1]$ in the 1D plasma model, while for the log-gas model, we show the crossover numerically and provide approximate calculations for large (close to 1) and small (close to 0) f. In the final part of my thesis, we consider an active version of the Calogero-Moser system ($k = 2$) where the particles are associated with telegraphic noise with two possible states $\pm v_0$. We numerically compute the global density profile in the steady state which shows interesting crossovers. As the activity increases, we observe a change from a density with sharp peaks characteristic of a crystal phase to a smooth bell-shaped density profile, passing through an intermediary stage of a smooth Wigner semi-circle characteristic of a liquid phase. To understand the crossovers analytically, we compute the variance and covariance of particle positions in the steady state under the weak noise limit. It is achieved by using the method introduced in Touzo *et al.* [Phys. Rev. E **109**, 014136 (2024)] to study the active Dyson's Brownian motion.

Chapter 1

Introduction

Interacting particle systems in equilibrium exhibit intriguing emergent phenomena, such as phase transitions [1, 2], which are absent in non-interacting systems. For example, unlike an ideal gas with no interparticle interactions, a van der Waals gas, where particles experience repulsion at short distances and attraction at long distances, undergoes a transition between the liquid and gas phases [1, 2]. This transition is characterized by a discontinuity in density, indicative of a first-order phase transition. Statistical physics is essential in understanding such macroscopic properties in many-particle interacting systems. Recent advancements in experimental technologies have enabled not only the measurement of global properties like density profiles but also the tracking of individual particles [3, 4]. This allows for the study of more detailed characteristics such as position correlations and gap statistics (mean gap, fluctuation, distribution), thereby enabling access to the study of microscopic properties of a system. Gap statistics provide insights into fluctuations at the microscopic level, facilitating an understanding of local correlations within the system. In a one dimensional system comprising of N particles interacting via a general two-body interaction potential $V(x_i - x_j)$, with x_j being the position of the j^{th} particle, one defines the spacing distribution in thermal equilibrium as, $P_N(s) = \frac{1}{N-1}\sum_i \langle \delta(s - s_i) \rangle$, where $\langle ... \rangle$ denotes an average over Gibbs-Boltzmann distribution. Here s_i is the spacing between successive particles normalized by their averages, $s_i = \Delta_i / \langle \Delta_i \rangle$ with $\Delta_i = x_{i+1} - x_i$. The reason for such normalization is to focus on universal features while disregarding information about local densities.

The distribution $P_N(s)$ is a well studied object in random matrix theory (RMT) and

quantum chaos [5–10] where it corresponds to the distribution of the spacing between successive eigenvalues and energy levels $\{\lambda_i\}$ respectively. It is a general consensus that for an integrable quantum system the level-spacing statistics follows Poissonian statistics whereas for non-integrable systems it follows RMT [7,8]. One of the important results in RMT is the universal form of $P_N(s)$ in the large N limit for the three Gaussian ensembles: Gaussian orthogonal ensemble, Gaussian unitary ensemble and the Gaussian symplectic ensemble, corresponding to the Dyson indices $\beta = 1, 2$, and 4 respectively. One finds that $P_\infty(s)$ is accurately described by $P_2(s) = A_\beta s^\beta e^{-B_\beta s^2}$, known as the Wigner surmise, where A_β and B_β are β dependent constants [5,6]. For the Gaussian orthogonal ensemble, the joint distribution $P_{\rm joint}(\{\lambda_i\})$ of eigenvalues $\{\lambda_i\}$ has the following form

$$P_{\rm joint}(\{\lambda_i\}) \propto \left(\prod_{i<j} |\lambda_i - \lambda_j|\right) \exp\left[-\frac{1}{2}\sum_{i=1}^{N} \lambda_i^2\right], \tag{1.1}$$

which can be interpreted as the equilibrium Gibbs-Boltzmann measure, $P_{\rm joint}(\{\lambda_i\}) \propto \exp[-\beta E(\{\lambda_i\})]$ of an interacting gas of N particles at inverse temperature $\beta = 1$ with energy

$$E(\{\lambda_i\}) = \frac{1}{2}\sum_{i=1}^{N} \lambda_i^2 - \frac{1}{2}\sum_{i\neq j} \log(|\lambda_i - \lambda_j|). \tag{1.2}$$

The energy function $E(\{\lambda_i\})$ represents a gas of particles in one dimension denoted by their positions $\{\lambda_i\}$. These particles are confined in a harmonic trap and interact with each other via a repulsive logarithmic potential. This system is known in the literature as the log-gas [5, 6].

It has been proven that in the large N limit, the spacing distributions in log-gas is invariant (up to some scaling) even after changing the external confining potential from harmonic to any other convex analytic potentail [11]. Thus, it is natural to ask what would happen to this distribution if we change the form of interaction among the particles keeping them confined in harmonic trap. Specifically, we examine a system of particles interacting with every other particle via pairwise repulsive power-law interactions confined within a 1-D harmonic trap. We denote the positions of the particles on the line by $x_j, (j = 1, 2, ..., N)$. The system is known as Riesz gas and is described by the following

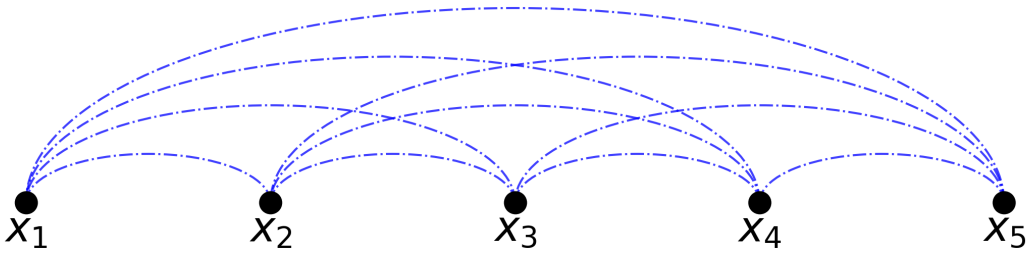

Figure 1.1: Schematic representation of a 1D system with five particles, illustrating all-to-all interactions as described in Eq. (1.3). Each particle is connected to every other particle via dashed blue lines, indicating that all particles are interacting with each other.

(potential) energy function [12, 13]

$$\mathcal{E}_k(\{x_i\}) = \sum_{i=1}^{N} \frac{x_i^2}{2} + \frac{J\ \mathrm{sgn}(k)}{2} \sum_{i \neq j} \frac{1}{|x_i - x_j|^k}, \tag{1.3}$$

where $J > 0$ denotes the strength of the interaction and $\mathrm{sgn}(k)$ ensures a repulsive interaction. Note that the $1/r^k$ interaction potential can be interpreted as the interaction between two charge particles separated by a distance r in $(k+2)$ dimensional space [14,15]. A system of particles with pairwise power-law interactions is described schematically in Fig. 1.1. The energy function in Eq. (1.3) can be broadly categorized into short-range and long-range interacting systems based on the parameter k. Since for $k > 1$, the interaction between particles decays faster than $1/r$ where r is the separation, this case is called short-range interaction. In contrast for $k < 1$, the interaction decays slowly with separation and is therefore called long-range interaction [16, 17]. As opposed to the short-range interactions, systems with long-range interaction exhibit a variety of counterintuitive phenomena, including non-equivalence of thermodynamic ensembles, negative specific heat, slow relaxation dynamics and anomalous heat transport, among others [16–28]. Note that while the first term in the energy function $\mathcal{E}_k(\{x_i\})$ tries to keep the particles close to the origin, the second term pushes the particles apart from each other. As a result of this competition, the particles are expected to settle over a finite region at any finite temperature. To ensure stability, the parameter k must be greater than -2, given that the confining potential is quadratic. Otherwise, the particles would fly off to infinity

due to strong repulsion among them. Special values of k in the Riesz gas described in Eq. (1.3) correspond to some important and well-studied models in the literature.

1. The interaction term in the energy function given in Eq. (1.3) reduces to a logarithmic interaction in the limit $k \to 0, J \to \infty$ keeping $J|k| = J_0$ fixed. The energy function in this case is given by

$$\mathcal{E}_0(\{x_i\}) = \sum_{i=1}^{N} \frac{x_i^2}{2} - \frac{J_0}{2} \sum_{i \neq j} \log(|x_i - x_j|), \tag{1.4}$$

   which is known as the Dyson's log-gas [29, 30]. From now on, we will refer to the log-gas as the $k = 0^+$ case of the Riesz gas, unless stated otherwise. The minimum energy configuration $\{y_i\}$, obtained by solving $\frac{\partial \mathcal{E}_0(\{x_i\})}{\partial x_i}|_{\{y_i\}} = 0$ for all $i = 1, \ldots, N$ are given by the zeros of the Hermite polynomials [31] for $J_0 = 1$. Consequently, the density profile of the particles follows the Wigner semi-circle form [5,6,32] in the large N limit. The distribution of the position of the rightmost (or equivalently the leftmost) particle is a well-studied object in the context of extreme value statistics. The typical distribution of this particle is described by the famous Tracy-Widom distribution [33–37]. Using its connection to random matrix theory, many interesting quantities have been extensively studied across various contexts, for example, extreme value statistics [35–37], index distribution [38], number variance [39], third-order phase transitions [37, 40, 41], non-interacting fermions [42–44], communication systems [45], and large-N gauge theory [46], to name a few.

2. The Riesz gas described by the energy function in Eq. (1.3) with $k = -1$ corresponds to the well-known 1-D one-component plasma (1DOCP) [47–50] where the particles interact through a truly 1-D Coulomb potential (linear in the separation between two particles)

$$\mathcal{E}_{-1}(\{x_i\}) = \sum_{i=1}^{N} \frac{x_i^2}{2} - \frac{J}{2} \sum_{i \neq j} |x_i - x_j|. \tag{1.5}$$

   This system, also known as the "jellium model" [51], comprises N charges of the same sign interacting with a uniform background of opposite charges, ensuring over-

all charge neutrality. This model serves as a paradigm for 1D charged plasma [52] and particularly interesting since numerous observables can be calculated analytically [47,48,53–55]. For example, recent studies include extreme value statistics and index istribution [49,50], truncated linear statistics [56], full counting statistics [57], as well as a third-order phase transition [49, 58].

3. The famous Calogero-Moser (CM) [59–68] model refers to the Riesz gas (Eq. (1.3)) with $k = 2$, thus it has the following energy function

$$\mathcal{E}_2(\{x_i\}) = \sum_{i=1}^{N} \frac{x_i^2}{2} + \frac{J}{2} \sum_{i \neq j} \frac{1}{(x_i - x_j)^2}. \tag{1.6}$$

   In this system, the constituent particles interact with repulsive inverse-square potential and are confined in a harmonic trap. The Hamiltonian dynamics of this system is integrable and has been well studied in the context of shocks [69, 70], generalized hydrodynamics [70–72], soliton physics [72, 73], out-of-time-order commutator [74]. A surprising result is that although the interaction potential in CM model is different from that in the log-gas, they share an identical minimum energy configuration and are hence given by the zeros of the Hermite polynomials [75]. Therefore, they share the same Wigner semi-circular density profile in the large N limit at finite temperature. Additionally, there are remarkable relations in the structure of the Hessian matrix that characterize small oscillations around the potential minimum [75].

4. Another well-known model is the hard rods model [76, 77], which represents a limiting case of $1/r^k$ repulsive interactions as $k \to \infty$. This interaction effectively implies that particles repel each other with infinite force upon contact, but otherwise, they do not interact at all. The dynamics of hard rods model is also integrable and has been known for a long time [78]. This model helps in understanding phase transitions and the impact of excluded volume effects on the thermodynamic properties of systems [76, 79]. Recently, there has been interest in breaking integrability by adding an external potential and studying how the system thermalizes. Interestingly, researchers have found that although adding an external harmonic potential

breaks the integrability in the hard rods model, the system fails to thermalize to Gibbs equilibrium [80, 81]. Instead, it reaches a stationary state [80, 81].

5. Interactions with other values of k have been possible to achieve in experiments- for example using Rydberg atoms [82–84] and cold atoms [85–87]. The ability to manipulate and control these systems with high precision has opened new avenues for exploring fundamental physics. For example, with Rydberg atoms, researchers can create and study large, strongly interacting systems with tunable interactions, providing insights into quantum many-body physics and phase transitions [88]. Furthermore, recent technological progress has made it possible to realize and investigate a variety of systems, including ions [88–90], dipolar Bose gases [91, 92], and coupled lasers [93]. Additionally, advances in absorption imaging techniques for cold atomic gases have made it possible to investigate both long and short-range interacting systems [91, 94–96]. Overall, these advancements in experimental technologies have significantly enhanced our ability to study and understand a wide range of physical systems, leading to new discoveries and deeper insights into the nature of matter and interactions.

Thus it is necessary to have a complete characterization of equilibrium and dynamical properties of such systems theoretically where Riesz gas offers a perfect platform. However, theoretical studies in this system currently are limited to only large-N field theory and average density profile for general k [97]. The knowledge of field theory turns out to be instrumental in many other studies, particularly in log-gas ($k = 0^+$) and 1DOCP ($k = -1$) systems, such as extreme value statistics [35, 36, 49, 50], number fluctuations [38, 39, 49, 50], large deviations [37, 49] etc., in equilibrium, especially in the large N limit. It is important to note that in all these works, the system has been studied using a coarse-grained description, focusing on macroscopic properties, thus involve many particles. In our first study, we examine the microscopic properties of these systems by looking at the statistics of the gap between successive particles [98]. We study the system size scaling of its mean and variance to characterize the system based on the power-law exponent k [98]. Additionally, we analyze the gap distributions to examine a potential generalization of the Wigner surmise.

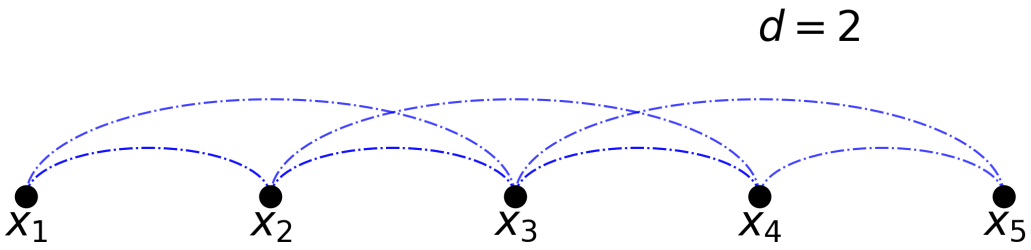

Figure 1.2: Schematic representation of a 1D system with five particles, illustrating short-ranged interactions as described in Eq. (1.7) with $d = 2$. Each particle can interact with up to two particles on its left and two on its right, if available. Interactions are depicted by connecting lines between particles; a line indicates that the particles are interacting, while the absence of a line indicates no interaction. For example, the first (leftmost) particle can only interact with the second and third particles, but not with the fourth or fifth. In contrast, the third particle can interact with all particles shown, as it has two particles on either side.

So far, our discussions have focused on systems with all-to-all coupling, where each particle interacts with every other particle. However, in many physical scenarios, interactions between particle pairs often get screened, resulting in effectively finite-ranged (FR) interactions. This naturally raises the question: what are the consequences of FR interactions on equilibrium properties, particularly within field theory and equilibrium density profiles? Recently, a generalized version of the Riesz gas has been introduced where constituent particles can only interact with $d \leq (N-1)$ neighboring particles on both sides, if any [99, 100] and is described by the energy function

$$\mathscr{E}_k(\{x_j\}) = \frac{1}{2}\sum_{i=1}^{N} x_i^2 + \frac{J\ \mathrm{sgn(k)}}{2} \sum_{\substack{i\neq j \\ |i-j|\leq d}}^{N} \frac{1}{\mid x_i - x_j \mid^k}, \ \forall\ k > -2. \tag{1.7}$$

Notice that, by varying the parameter d, one can tune the range of interaction from nearest-neighbor ($d = 1$) to all-to-all interacting ($d = N-1$). In a system of five particles, the energy function in Eq. (1.7) is schematically described in Fig. 1.2 for $d = 2$. When $d \sim \mathcal{O}(1)$, each particle interacts with only a few neighboring particles, making the system short-ranged. Interestingly, the corresponding field theory and equilibrium density profile in the short-ranged (SR) case [$d \sim \mathcal{O}(1)$] exhibit significant deviations

from those observed in the all-to-all coupling case, particularly for $k \leq 0$. In the SR case, the free energy functional is local in space for any $k > -2$, contrasting with the non-local free energy obtained in the all-to-all coupling scenario for $-2 < k < 1$. Equilibrium density profiles, obtained by solving relevant saddle point equations also show substantial differences for $k \leq 0$. For instance, in the 1DOCP, the equilibrium density profile in the SR case is a Gaussian which is infinitely extended. On the other hand in the all-to-all coupling case, the density profile is uniform and supported over a finite region. In the log-gas with short-ranged interaction, the density profile adopts a Gaussian shape instead of the Wigner semi-circle profile seen in the all-to-all coupling limit. Thus, one expects a crossover in density profile as one tunes the parameter d from $(N-1)$ to 1. One would also expect similar crossovers in the equilibrium density profile when the system's temperature varied from very low to very high values. At very low temperatures, the free energy functional is dominated by the energy functional, while the entropy term is subdominant in system size N. Thus, the equilibrium density profile is governed by the ground state (zero temperature) configuration. Conversely, at very high temperatures, the interactions among the particles become negligible and the entropy term competes with the confining harmonic potential, leading to a Gaussian density profile. Lowering the temperature of a system is similar to increasing the strength of interaction. These crossovers, due to changes in the strength of interaction or equivalently in temperature have been explored in the context of random matrix theory [101,102]. In Ref. [103], rather than varying the temperature or interaction strength, we explore how the crossover in the equilibrium density profile is influenced by adjusting the range of interaction through the parameter $f(= d/N)$. A thorough investigation of this inquiry has been conducted for two models: namely the 1DOCP and the log-gas.

Recently, researchers have begun to investigate the dynamics of interacting many-particle systems with power-law interactions [104–110]. However, there exist only a few analytical studies even in one spatial dimension [107–110]. In Ref. [107], the authors considered a system of particles on a line with all-to-all coupled power-law interactions, $V(r) \sim 1/r^k$ for $k > 0$. However, there was no external potential, making the system translationally invariant. By deriving macroscopic fluctuation theory-type equations, they analytically computed the temporal growth of the variance of particle positions

and the integrated current and found interesting distinction whether the system is short-ranged ($k > 1$) or long-ranged ($k < 1$). In Ref. [110], the Langevin dynamics of N particles in one dimension with 1D Coulomb interaction ($k = -1$) was considered, once again, without any external confining trap. By mapping to the Lieb-Liniger model of quantum bosons, the exact joint distribution of the particles was computed. This further led to the computation of the fluctuations of particle positions around their average positions, gap statistics, and more [110]. To the best of our knowledge, there are no analytical studies on non-equilibrium properties of Riesz gas in confinement except Refs. [108, 109]. In Ref. [108], an active version of Dyson's Brownian motion (DBM) model has been introduced in which the particles interact via pairwise repulsive logarithmic interaction and are confined in a harmonic trap. Additionally, the particles are subjected to a telegraphic noise. The overdamped Langevin equations of motion are given by

$$\frac{dx_i}{dt} = x_i - \sum_{j \neq i} \frac{1}{x_i - x_j} + v_0 \sigma_i(t) \quad \text{for } i = 1, 2, \ldots, N, \tag{1.8}$$

where the spin degrees of freedom σ_i, associated with each particle, alternate independently between two values, ± 1, at a constant rate γ and v_0 denotes the strength of the noise. In the limit where $v_0 \to \infty$ and $\gamma \to \infty$ with $v_0^2/2\gamma$ remaining finite, the motion of the particles described in Eq. (1.8) reduces to the DBM with diffusion constant $D = v_0^2/2\gamma$ [111]. In this limit, the equilibrium configuration of the particles coincides with the zeros of the Hermite polynomials, leading to a density profile that converges to a Wigner semi-circle [32]. For any finite values of v_0 and γ, the system will eventually reach a non-equilibrium steady state from arbitrary initial conditions. This behavior results from the interplay between the harmonic confining term, the repulsive logarithmic interaction and the active noise. Surprisingly, across a broad range of the activity strength v_0, the researchers have found that the density profile in the steady state maintains the shape of the Wigner semi-circle, similar to the DBM [5, 6]. To support these intriguing findings, the researchers also provided analytical arguments based on the computations of the covariance of particle positions [109]. As mentioned earlier, the famous Calogero-Moser model, where the particles are confined in a one-dimensional harmonic trap with a pairwise repulsive inverse square-law interaction potential, also shares the same Wigner

semi-circular density profile in their passive motion [109]. It would be interesting to see how the results of the active DBM obtained in Refs. [108, 109] get modified if the interaction is changed. In the last part of the thesis, we study the non-equilibrium dynamics of an active version of the Calogero-Moser model by analyzing the density profile and covariance in particle positions in the steady state.

In brief, the thesis addresses three main investigations. It is organized as follows. In chapter 2, we analyze gap statistics for a harmonically confined Riesz gas in thermal equilibrium, focusing on the mean and variance of the bulk gap, and the distributions. In chapter 3, we investigate the crossover in equilibrium density profiles resulting from variations in the interaction range, particularly for 1DOCP and log-gas. Shifting to a non-equilibrium setup, we study the Calogero-Moser system driven by active noises and explore the crossover in the density profile and compute covariances in particle positions (chapter 4).

Chapter 2

Gap statistics for confined particles with power-law interactions

The study of dynamics and thermodynamic properties of long-range interacting systems has generated lots of interest in the last few decades [20–26]. Examples of such systems include, but are not limited to, charged particles [14, 15], dipoles [14, 15], gravitational systems [18, 27], hydrodynamics [19], and cold atomic systems [87–89]. Often these systems are characterized by the two-particle interaction potential $V(r) \sim 1/r^k$ where r is the distance between two particles. The parameter k determines the range of interaction — smaller the value of k, larger the range of the interaction potential. One well-known example of a many-particle classical interacting system in one dimension is the harmonically confined Riesz gas consisting of N particles, described by the energy function given in Eq. (1.3). The non-trivial all-to-all coupling interactions makes this difficult but some progress has recently been made [35–37, 40, 41, 44, 49, 50, 91, 97, 112–117]. The system is considered to be in thermal equilibrium at inverse temperature β which implies that any configuration $\{x_i\}$ with energy function $\mathcal{E}_k(\{x_i\})$ has equilibrium Gibbs measure of the form

$$\mathcal{P}_G(\{x_i\}) = \frac{e^{-\beta \mathcal{E}_k\{x_i\}}}{\mathcal{Z}_N(\beta)}, \tag{2.1}$$

where the partition function $\mathcal{Z}_N(\beta) = \int \prod_i dx_i e^{-\beta \mathcal{E}_k\{x_i\}}$ and henceforth we set the inverse temperature $\beta = 1$. We assume the Boltzmann constant $k_B = 1$ throughout this thesis. Without any loss of generality, we assume that the particles are ordered which implies

$x_1 \leq x_2 \leq x_3 \ldots \leq x_N$. As pointed out in the introduction, due to the competition between the confining potential and the repulsive power-law interactions, the particles are expected to settle over a finite distance at any finite temperature. The mean thermal density of particles is defined as $\rho_N^{(\mathrm{eq})}(x) = \frac{1}{N}\sum_{i=1}^{N}\langle\delta(x-x_i)\rangle$, where $\langle ...\rangle$ denotes a thermal average over the distribution $\mathcal{P}_G(\{x_i\})$. Using large-N field theory, the average thermal density is calculated recently $\forall\ k > -2$ [97], thereby obtaining a generalization of the Wigner semi-circle law for the log-gas [32]. The form of the average density profile and the scaling of its support with increasing N was found to be nontrivial. The average density, $\rho_N^{(\mathrm{eq})}(x)$, for large N is independent of the inverse temperature, β and is described by the following scaling form

$$\rho_N^{(\mathrm{eq})}(x) \equiv \frac{1}{N}\sum_{j=1}^{N}\langle\delta(x-x_j)\rangle = \frac{1}{l_k N^{\alpha_k}} F_k\big(\frac{x}{l_k N^{\alpha_k}}\big), \tag{2.2}$$

where α_k is given by

$$\alpha_k = \begin{cases} \frac{k}{k+2} \text{ for} & \mathrm{k} > 1 \\ \frac{1}{k+2} \text{ for} & -2 < \mathrm{k} < 1. \end{cases} \tag{2.3}$$

The scaling function $F_k(y)$, supported over $y \in [-1/2, 1/2]$, is given explicitly by

$$F_k(y) = \frac{1}{\mathbf{B}\big(\gamma_k+1, \gamma_k+1\big)}\big(\frac{1}{4}-y^2\big)^{\gamma_k}, \tag{2.4}$$

where the exponent γ_k is given by

$$\gamma_k = \begin{cases} \frac{1}{k} & \text{for} \quad \mathrm{k} > 1 \\ \frac{k+1}{2} & \text{for} \ -2 < \mathrm{k} < 1, \end{cases} \tag{2.5}$$

and the system size independent length scale is explicitly

$$l_k = \begin{cases} \Big(\frac{\left(2J\zeta(k)(k+1)\right)^{1/k}}{\mathbf{B}(1+1/k,1+1/k)}\Big)^{\frac{k}{k+2}} & \text{for} \quad \mathrm{k} > 1 \\ \Big(\frac{J|k|\pi(k+1)}{\sin\left[\frac{\pi}{2}(k+1)\right]\mathbf{B}(\frac{k+3}{2},\frac{k+3}{2})}\Big)^{\frac{1}{k+2}} & \text{for} \ -2 < \mathrm{k} < 1, \end{cases} \tag{2.6}$$

where $\mathbf{B}$ is the beta function. We use these densities to study the statistical properties of interparticle bulk gaps, $\Delta_i = x_{i+1} - x_i$ (for $1 \ll i \ll N$) in detail. Very recently, the average density profile, in the presence of a hard wall, has been computed exactly [115] which eventually leads to the computation of extreme value statistics for all $k > -2$ [116].

One of the interesting observations of Ref. [97] was on the system-size scaling of the mean separation $\langle \Delta_i \rangle$ between neighboring particles in the bulk. This has the form $\langle \Delta_i \rangle \sim N^{-a_k}$ where a_k has a non-monotonic dependence on k and can have both positive and negative signs. For a complete characterization, it is necessary to go beyond the mean and study the fluctuations of this quantity as well as its full distribution. As described in the introduction, we study the distribution of the normalized separation $s_i = \Delta_i / \langle \Delta_i \rangle$ defined as

$$P_N(s) = \frac{1}{N-1} \sum_{i=1}^{N-1} p_N^{(i)}(s), \tag{2.7}$$

where $p_N^{(i)}(s) = \langle \delta(s - s_i) \rangle$ is the distribution of the i-th normalized gap. We expect that for typical fluctuations, $P_N(s)$ will be dominated by the bulk gaps, but edge gap contributions could be important for atypical s. The interplay between the power-law interactions and the confining potential makes this a fascinating and difficult question and this is the main focus of this chapter.

Recall that the equilibrium distribution of particle positions in the log-gas ($k = 0^+$) at inverse temperature β, corresponds to the distribution of eigenvalues of random matrices for the Gaussian orthogonal, unitary and symplectic ensembles [5, 6]. From this correspondence, it is known that the distribution of particle spacing, normalized by the mean spacing, is given quite accurately by the Wigner surmise (WS) [5, 6, 32]. A variant of the WS has also been applied to the Calogero-Moser model ($k = 2$) [67] but to the best of our knowledge, there are no results for other values of k and this chapter provides a complete characterisation. Needless to mention, fluctuations at the microscopic level is an avenue that is essentially unexplored in systems with long-range interactions. Probing such fluctuations has now become experimentally accessible given the recent breakthroughs in the technology of quantum gas microscopy [118–122]. Gap fluctuations give us a novel way to probe aspects of the underlying interacting systems that are otherwise completely elusive

to diagnostics such as density profiles.

Before diving into a detailed discussion, we first provide a summary of our main findings.

1. We compute the system-size scaling of the variance of the bulk gap. For the exponent b_k which characterizes the system size scaling of variance of the bulk gap, we conjecture a non-trivial form in Eq.(2.9). Through direct Monte-Carlo (MC) simulations, we verify that b_k indeed exhibits the non-trivial k dependence as described in Eq.(2.9).

2. This proposed form is further validated by our results based on two (semi) analytical methods: microscopic Hessian calculation and quadratic field theory approach. In the first method, we start with the microscopic energy function $\mathcal{E}_k(x_i)$ given in Eq. (2.12) to find the Hessian matrix which describes the fluctuations of the nearest-neighbor gaps around their average values. By numerically inverting the Hessian matrix, we compute the variance of the bulk gaps (see Sec. 2.2). We find that except in the regime $-1 < k < 0$, this theory works well (see Fig. 2.3). In the second method, we use the quadratic field theory approach, starting with the free energy functional developed in Ref. [97]. We then connect the fluctuations in the macroscopic density profile to those of the nearest-neighbor gaps (see Eq.(2.22) and the discussion preceding Eq.(2.25)). This results in a matrix similar to the one obtained in the microscopic Hessian calculation (see Eq.(2.25)). We then compute the variance of the bulk gaps by inverting this matrix. Surprisingly, we find that this field theory method works exceptionally well for $\forall k > -2$ (see Fig. 2.3).

3. We study the scaling properties of the gap distributions for different k and observe that there exist four regimes, as shown in Fig. 2.1. As in the log-gas, we find that for the 1DOCP the distribution $P_N(s)$ converges very quickly with system size N (see Fig.2.6 (b), (d)); however, it fails to generalize the results of the Wigner surmise [57]. For other values of k, the distributions $P_N(s)$ are not system size-independent, leading to the analysis of $\tilde{P}_N(\tilde{s})$ (see Eq. (2.30)), which turns out to be independent of system size except in the range $-1 < k < 0$. Additionally, we find that the distributions $\tilde{P}_N(\tilde{s})$ can be well approximated by a normal distribution

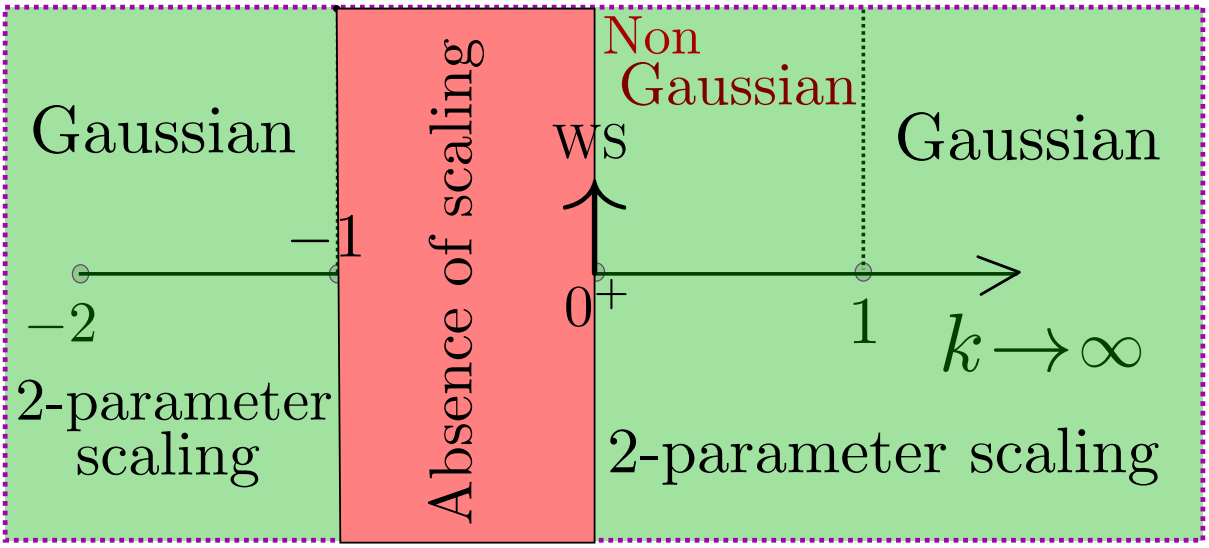

Figure 2.1: Schematic phase diagram of the behavior of the gap distribution. We find four regimes in $k \in (-2, \infty)$, where the gap distribution has different scaling properties. In the region $(-2,-1) \cup (0,\infty)$ the scaling limit is achieved by using mean and the variance of gap only. The scaling function for $k \in (-2,-1) \cup (1,\infty)$ is Gaussian whereas it is non-Gaussian in $k \in (0,1)$. In the regime $k \in (-1,0)$ we are unable to obtain a scaling limit.

(mean zero and variance unity) near the maxima for all $k > -2$ except in the range $[-1,1]$ (see Fig. 2.7).

2.1 Results for mean and variance of bulk gap

The average bulk gap, $\langle \Delta_i \rangle = \frac{1}{N \rho_N^{(\mathrm{eq})}(y_i)}$ which naturally scales with system size as

$$\langle \Delta_i \rangle \sim N^{-a_k}, \text{ with } a_k = 1 - \alpha_k = \begin{cases} \frac{2}{k+2} & \text{for} \quad k > 1 \\ \frac{k+1}{k+2} & \text{for} \quad -2 < k < 1. \end{cases} \tag{2.8}$$

We also find a power-law dependence on the system size of the gap fluctuations $\sigma^2_{\Delta_i} = \langle \Delta_i^2 \rangle - \langle \Delta_i \rangle^2$. In particular, for the mid-gap corresponding to $i = N/2$, we make the following conjecture based on theoretical arguments involving both microscopic Hessian

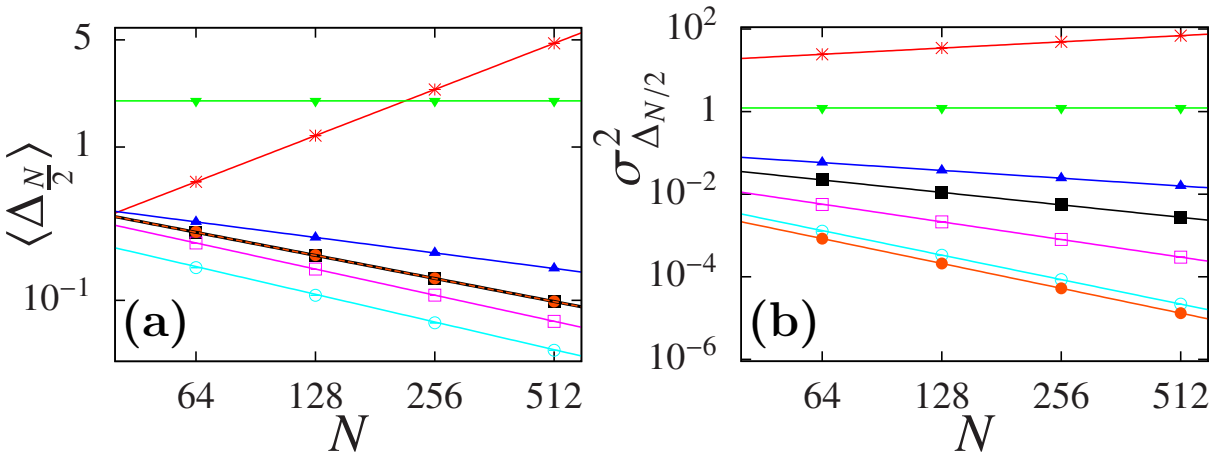

Figure 2.2: Mean (left) and variance (right) of mid gap as a function of system size for $k = 2(\bullet), 1.5(\circ), 0.5(\square), 0^+(\blacksquare), -0.5\ (\blacktriangle), -1(\blacktriangledown)$ and $-1.5(*)$. Solid lines correspond to their corresponding power-law fitting (Eq. 2.9). The slopes in (a) are $a_k = 0.5, 0.57, 0.6, 0.5, 0.33, 0, -1$ and in (b) are $b_k = 2, 1.97, 1.42, 1, 0.63, 0, -1$, for decreasing k. These are consistent with Eq. (2.8) and Eq. (2.9) as elucidated in Fig. 2.3. The error bars are negligible [98]. In (a) the data for $k = -1.5$ is scaled by a factor 500. A total number of $\sim 10^8$ MC samples are used for the computations.

and field theory at the microscopic scale (see below):

$$\sigma^2_{\Delta_{N/2}} \sim N^{-b_k}, \quad \text{where} \quad b_k = \begin{cases} 2 & \text{for} \quad k > 1 \\ 1+k & \text{for} \quad 0 < k < 1 \\ 2\frac{(k+1)}{(k+2)} & \text{for} \quad -1 < k < 0 \\ 1+k & \text{for} \quad -2 < k < -1. \end{cases} \tag{2.9}$$

We present numerical evidence for the above conjecture in Figs. 2.2 and 2.3 where we observe reasonable agreement between the numerically obtained exponent and the conjectured values. The details of numerical simulations are given in Appendix. A.1. We believe that the slight deviations from the predictions for a few values of k are due to finite-size effects [98]. We verify that the above scaling in Eq. (2.9) also holds for other gaps deep in the bulk. Interestingly we find that for $-1 \leq k \leq 0$, the ratio $\sigma_{\Delta_i}/\langle \Delta_i \rangle$ as well as $P_N^{(i)}(s)$ are weakly dependent on i (for large N and i in the bulk; see Sec. 2.5). Next, we first discuss our arguments based on the microscopic Hessian approach which is followed by the field theory-based arguments. Both the approximate calculations are valid as long as the typical variation of the distance between successive particles σ_{Δ_i} is

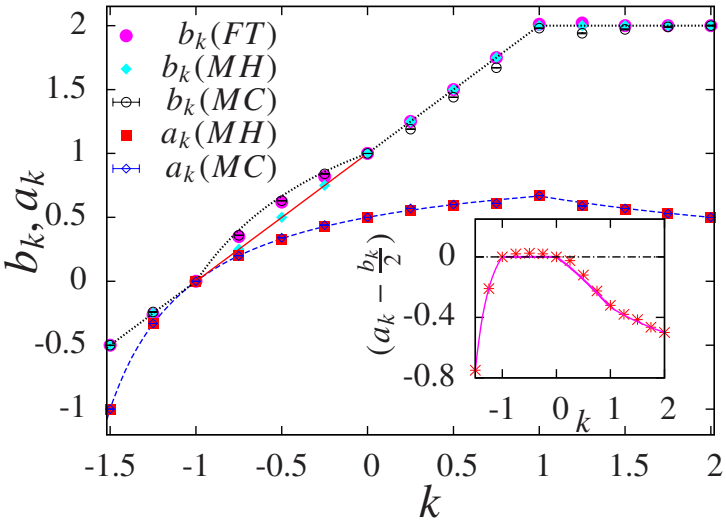

Figure 2.3: Comparison of the exponents a_k and b_k (symbols) obtained from simulations (MC), from MH and FT calculations, with Eqs. (2.8) (dashed line) and (2.9) (dotted line). In the inset we plot $\left(a_k - \frac{b_k}{2}\right)$ which quantifies the relative fluctuations $\sigma_\Delta/\langle\Delta\rangle$ in the MC data. To extract b_k the largest system sizes used were $N = 2048$ for MC, 4096 for MH and 16384 for FT. All the error bars are smaller than the point symbols [98].

much smaller than the average separation, $\langle\Delta_i\rangle$ [109]. In this regard, we have computed the ratio $\frac{\sigma_{\Delta_i}}{\langle\Delta_i\rangle}$ which has the following system size dependence in the large N limit,

$$\frac{\sigma_{\Delta_i}}{\langle\Delta_i\rangle} \sim \mathcal{O}(N^{(a_k - b_k/2)}) \text{ for } 1 \ll i \ll N. \tag{2.10}$$

The exponent $(a_k - b_k/2)$ is plotted as a function of k in the inset of Fig. 2.3 which clearly shows that this exponent is negative for all $k > -2$, except in the range $-1 < k < 0$. Therefore, one expects that in the large N limit, the approximate theories hold for all $k > -2$, except for the region $-1 < k < 0$.

2.2 Microscopic Hessian (MH)

Computing analytically the variance of the gap for generic values of k is hard (except for $k = -1$ and $k = 0^+$). Here, we use the microscopic Hessian method to estimate the variance for large N for all values of k. In the thermal equilibrium at inverse temperature β, the particles are sampled from the Gibbs Boltzmann distribution (see Eq. (2.1)). Then

the joint distribution of all gaps is given by

$$\mathcal{P}(\{\Delta_i\}) = \int dx_1 \int dx_2 \cdots \int dx_N \left(\prod_{i=1}^{N-1} \delta\left(\Delta_i - (x_{i+1} - x_i)\right) \right) e^{-\beta \mathcal{E}(\{x_i\})}. \tag{2.11}$$

Notice that for notational simplicity, we have used $\mathcal{E}$ instead of $\mathcal{E}_k$ for the energy function given in Eq. (1.3). From now on, we will continue using $\mathcal{E}$. Also note that the distribution $\mathcal{P}$ in Eq. (2.11) involves $(N-1)$ gap variables Δ_i for $i = 1, 2, \ldots, N-1$, rather than N. Using this distribution in Eq. (2.11), in principle one can calculate mean and the variance of i^{th} gap. However, the integrals over microscopic positions are difficult to compute, so we only solve them approximately. At zero temperature, the system will be in the ground state characterized by the configuration of positions y_i and corresponding gaps $\Delta_i^{\text{GS}} = y_{i+1} - y_i$. At low temperatures we expect that the Hessian of the microscopic energy $\mathcal{E}(\{x_i\})$ given in Eq. (1.3) about the ground state would approximately capture the behavior of the fluctuations of the gap. The positions y_i are obtained by minimizing the energy using the Broyden-Fletcher-Goldfarb-Shanno algorithm [123,124]. Under the Hessian approximation the joint distribution of fluctuation of gaps $\delta\Delta_i = \Delta_i - \Delta_i^{\text{GS}}$

$$\mathcal{P}_{MH}(\{\Delta_i\}) \sim e^{-\frac{\beta}{2} \sum_{i,j=1}^{N} H_{ij} \delta\Delta_i \delta\Delta_j}, \tag{2.12}$$

where the Hessian of the system about the equilibrium configuration is $H_{ij} = \left[\frac{\partial^2 \mathcal{E}(\{x_i\})}{\partial \Delta_i \partial \Delta_j} \right]_{\text{GS}}$. The matrix H_{ij} is obtained as follows. The Hessian $\tilde{H}_{ij}$ of the energy function $\mathcal{E}(\{x_i\})$ in terms of the fluctuation of positions around their equilibrium values are given by

$$\begin{aligned} \tilde{H}_{ij} &= \Big[\frac{\partial^2 \mathcal{E}(\{x_i\})}{\partial x_i \partial x_j} \Big]_{\text{GS}} \\ &= \delta_{ij} \Big[1 + \sum_{n \neq i}^{N} \frac{J \ \text{sgn}(k) k(k+1)}{\big(y_i - y_n\big)^{k+2}} \Big] \\ &\quad - (1 - \delta_{ij}) \frac{J \ \text{sgn}(k) k(k+1)}{\big(y_i - y_j\big)^{k+2}}. \end{aligned} \tag{2.13}$$

To get the Hessian H_{ij}, we change position to the gap variables, $\Delta_i = x_{i+1} - x_i$ for $i = 1, \ldots, N-1$ and the centre of mass coordinate which we denote by $\Delta_N \equiv \frac{1}{N} \sum_{i=1}^{N} x_i$

by the transformation

$$x_j = \Delta_N - \sum_{i=j}^{N-1} \Delta_i + \sum_{i=1}^{N-1} \frac{i}{N} \Delta_i \tag{2.14}$$

$$= \sum_{j=1}^{N} \mathcal{A}_{ij} \Delta_j, \tag{2.15}$$

where $\mathcal{A}$ is a matrix of dimension $N \times N$ with matrix elements

$$\mathcal{A}_{ij} = \begin{cases} \frac{j}{N} & \text{for } i > j \\ (\frac{j}{N} - 1) & \text{for } i \leq j (\neq N) \\ 1 & \text{for } j = N, i = 1, ..., N. \end{cases} \tag{2.16}$$

The quadratic Hamiltonian in terms of new variables becomes $\frac{1}{2} \sum_{i,j=1}^{N} H_{ij} \delta\Delta_i \delta\Delta_j$, where $H = \mathcal{A}^T \tilde{H} \mathcal{A}$. Using Eq. (2.12) we compute the variance of bulk gap from the relation $\sigma_i^2 = \langle \delta\Delta_i^2 \rangle = (\beta H)_{ii}^{-1}$, where H_{ii}^{-1} is found numerically. As seen in Fig. 2.3, the exponent b_k calculated using MH theory matches with the MC result (Eq. 2.9) except in the regime $-1 < k < 0$. This is perhaps not surprising since our conjecture suggests that in this regime, the relative fluctuation of the gap, $\sigma_{\Delta_i}/\langle \Delta_i \rangle \sim N^{(a_k - b_k/2)}$ does not decrease with system size — in fact over the range of N considered we see them increasing (see inset of Fig. 2.3). Next, we discuss the FT calculation.

2.3 Quadratic field theory (FT)

As discussed in Ref. [97] the Riesz gas for large-N can be described by a free energy functional $\Sigma[\rho_N] = \mathcal{E}[\rho_N] - \beta^{-1}\mathcal{S}[\rho_N]$ corresponding to a macroscopic density profile $\rho_N(x)$ where $\mathcal{E}[\rho_N]$ is the energy and

$$\mathcal{S}[\rho_N] = -N \int_{-\infty}^{\infty} dx \rho_N \log(\rho_N) \tag{2.17}$$

is the entropy functional [36]. The form of the energy functional depends on k, being local for $k \geq 1$ and non-local for $-2 < k < 1$ [97]. The energy functional, $\mathcal{E}[\rho_N(x)]$ is

given by

$$\mathcal{E}[\rho_N(x)] \approx \frac{N}{2}\int_{-\infty}^{\infty} x^2 \rho_N(x) dx + J\zeta(k) N^{k+1} \int_{-\infty}^{\infty} [\rho_N(x)]^{k+1} dx, \tag{2.18}$$

for $k > 1$ whereas for $-2 < k < 1$, it is given by

$$\mathcal{E}[\rho_N(x)] \approx \frac{N}{2}\int_{-\infty}^{\infty} x^2 \rho_N(x) dx + \frac{J\ \mathrm{sgn}(k) N^2}{2} PV \int_{-\infty}^{\infty} dx \int_{-\infty}^{\infty} dx' \frac{\rho_N(x)\rho_N(x')}{|x-x'|^k}. \tag{2.19}$$

where PV stands for principal value [97]. For a given macroscopic density profile $\rho_N(x)$, the gap between two consecutive particles at position x is $\bar{\Delta} = [N\rho_N(x)]^{-1}$. Note that this definition of the gap is different from the gap Δ_i defined earlier [below Eq. (2.6)] from the microscopic position configuration. The gap $\bar{\Delta}$ is a coarse-grained version of Δ averaged over many microscopic configurations consistent with the macroscopic density $\rho_N(x)$. As the density profile $\rho_N(x)$ fluctuates, the separation $\bar{\Delta}$ also fluctuates. We expect that for large N, the fluctuation of $\bar{\Delta}$ and Δ would have the same scaling with respect to N. We first find the distribution of the fluctuation $\delta\rho_N(x)$ around the equilibrium profile $\rho_N^{(\mathrm{eq})}(x)$ in the following way.

As our aim is to find the joint distribution of $(N-1)$ gaps, it will be useful to approximate the principal value integral in the Eq. (2.19). To do so we assume that there is a particle at x and break up the x' integrals in the three regions, $(-\infty, x-\bar{\Delta})$,$(x-\bar{\Delta}, x+\bar{\Delta})$ and $(x+\bar{\Delta}, \infty)$, where $\bar{\Delta}$ is the separation between two adjacent particles. Noting that the $\rho_N(x')$ vanishes in the window $(x-\bar{\Delta}, x+\bar{\Delta})$, we rewrite Eq. (2.19) as

$$\mathcal{E}[\rho_N(x)] \approx \frac{N}{2}\int_{-\infty}^{\infty} x^2 \rho_N(x) dx + \frac{J\ \mathrm{sgn}(k) N^2}{2} \int_{-\infty}^{\infty} dx \left[\int_{-\infty}^{x-\bar{\Delta}} + \int_{x+\bar{\Delta}}^{\infty}\right] dx' \frac{\rho_N(x)\rho_N(x')}{|x-x'|^k}. \tag{2.20}$$

The average value of the gap is given by the equilibrium density profile $\rho_N^{(\mathrm{eq})}(x)$ *i.e.* $\langle\bar{\Delta}\rangle = \frac{1}{N\rho_N^{(\mathrm{eq})}(x)}$. The probability of a given density profile $\rho_N(x)$ [99] is

$$\mathbb{P}[\rho_N] \sim e^{-\beta\delta\Sigma}, \text{ with, } \delta\Sigma = \Sigma[\rho_N] - \Sigma[\rho_N^{(\mathrm{eq})}] \tag{2.21}$$

where $\Sigma[\rho_N] = \mathcal{E}[\rho_N(x)] - \beta^{-1}\mathcal{S}[\rho_N(x)]$ is the free energy functional. Writing the fluctu-

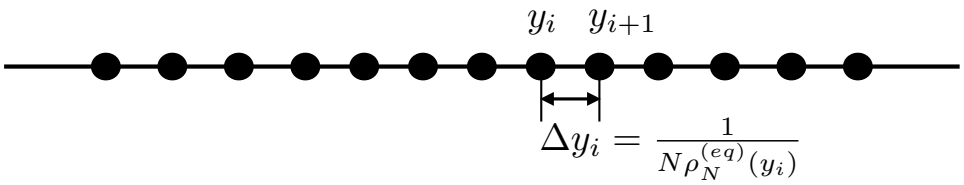

Figure 2.4: Schematic description of the discretization of the integral in the action $\delta\Sigma$.

ations of density profile about the equilibrium as $\rho_N(x) = \rho_N^{(\mathrm{eq})}(x) + \delta\rho(x)$ and using the relation $\bar{\Delta} = [N\rho_N(x)]^{-1}$ we obtain

$$\bar{\Delta}(x) = \langle\bar{\Delta}\rangle + \delta\bar{\Delta} = \frac{1}{N\rho_N^{(\mathrm{eq})}(x)} - \frac{\delta\rho(x)}{N\left(\rho_N^{(\mathrm{eq})}(x)\right)^2}. \tag{2.22}$$

Using this Eq. (2.22) we expand the exponent $\delta\Sigma = \Sigma[\rho_N] - \Sigma[\rho_N^{(\mathrm{eq})}]$ in Eq. (2.21) in powers of $\delta\rho(x)$ (up to second order in $\delta\rho$) to get

$$\begin{aligned}\delta\Sigma[\delta\rho, \rho_N^{(\mathrm{eq})}] \approx{}& \frac{J\zeta(k)k(k+1)N^{k+1}}{2} \\ &\times \int_{-l_k}^{l_k} dx\ [\rho_N^{(\mathrm{eq})}]^{k-1}\ \delta\rho(x)^2 \\ &+ \frac{N}{2\beta}\int_{-l_k}^{l_k} dx\ \frac{\delta\rho(x)^2}{\rho_N^{(\mathrm{eq})}(x)}, \quad \text{for } k > 1,\end{aligned} \tag{2.23}$$

and

$$\begin{aligned}&\delta\Sigma[\delta\rho, \rho_N^{(\mathrm{eq})}] \\ &\approx \frac{2J\ \mathrm{sgn}(k)N^{k+1}}{2}\int_{-l_k}^{l_k} dx\ [\rho_N^{(\mathrm{eq})}]^{k-1}\ \delta\rho(x)^2 \\ &+ \frac{J\mathrm{sgn}(k)N^2}{2}\int_{-l_k}^{l_k} dx\left[\int_{-l_k}^{x-\langle\bar{\Delta}\rangle} + \int_{x+\langle\bar{\Delta}\rangle}^{l_k}\right] dx' \\ &\qquad\times\ \frac{\delta\rho(x)\ \delta\rho(x')}{|x-x'|^k}, \\ &\quad + \frac{N}{2\beta}\int_{-l_k}^{l_k} dx\ \frac{\delta\rho(x)^2}{\rho_N^{(\mathrm{eq})}(x)}, \quad \text{for } -2 < k < 1.\end{aligned} \tag{2.24}$$

It is pertinent to note that, in the quadratic approximation of the field theory, the local term appears due to the fluctuations of the coarse-grained gap $\bar{\Delta}$ in the non-local

term of the energy $\mathcal{E}[\rho_N(x)]$ for $-2 < k < 1$. However, for $k > 1$ the field theory in Eq. (2.18) is local to the leading order in N. This leads to Eq. (2.23) which further implies $\sigma^2_{\Delta_{N/2}} \sim N^{-2}$. We have neglected the contribution from non-local terms in the field theory because they are expected to contribute to $\sigma^2_{\Delta_{N/2}}$ at most at the same order (N^{-2}) or less, thereby leaving the scaling exponent value b_k unchanged. For N (large but finite) particles there are $(N-1)$ number of gap variables. In order to find the joint distribution of these (discrete) gap variables from the field theory description, we need to discretize $\delta\Sigma$ given in Eqs. (2.23) and (2.24). To do so, we discretize the integral in the action $\delta\Sigma$ about the equilibrium positions $\{y_i\}$ (see Fig. 2.4). Recall that the microscopic Hessian was computed about this position configuration in Eq. (2.12). Note that the equilibrium (in this case the minimum energy) position configuration $\{y_i\}$ corresponds to equilibrium macroscopic density $\rho_N^{(\mathrm{eq})}(x)$ which implies that the mean gaps $\langle \bar{\Delta}_i \rangle = 1/N \rho_N^{(\mathrm{eq})}(y_i)$. Also note that for large-N, $\langle \bar{\Delta}_i \rangle \approx \Delta_i^{\mathrm{GS}}$. We emphasize that this discretization of the density profile is different from the original microscopic position description of the system. Hence replacing the integrals as $\int_{-l_k}^{l_k} dx \to \sum_i \frac{1}{N\rho_N^{(\mathrm{eq})}(y_i)}$ and performing some simplifications we get the following joint distribution of the gap variables $\{\delta\bar{\Delta}_i\}$:

$$\mathcal{P}_{\mathrm{FT}}\left(\{\delta\bar{\Delta}_i\}\right) \sim e^{-\frac{\beta}{2}\sum_{i,j=1}^{N} M_{ij}\delta\bar{\Delta}_i\delta\bar{\Delta}_j}, \text{where} \tag{2.25}$$

$$M_{ii} = \begin{cases} J\zeta(k)k(k+1)N^{k+2}[\rho_N^{(\mathrm{eq})}(y_i)]^{k+2} & \text{for} \quad k > 1 \\ 2JN^{k+2}[\rho_N^{(\mathrm{eq})}(y_i)]^{k+2} & \text{for} \quad 0 < k < 1 \\ N^2\beta^{-1}[\rho_N^{(\mathrm{eq})}(y_i)]^2 & \text{for} \quad -2 < k < 0, \end{cases}$$

$$M_{i\neq j} = \begin{cases} 0 & \text{for} \quad k > 1 \\ JN^2\ \mathrm{sgn}(k)\frac{\rho_N^{(\mathrm{eq})}(y_i)\rho_N^{(\mathrm{eq})}(y_j)}{|y_i - y_j|^k} & \text{for} \quad -2 < k < 1, \end{cases} \tag{2.26}$$

in the leading orders in N. Using the scaling form $\rho_N^{(\mathrm{eq})}(x) = \frac{1}{l_k N^{\alpha_k}} F_k\left(\frac{x}{l_k N^{\alpha_k}}\right)$ with $\alpha_k = \frac{k}{k+2}$ for $k > 1$ and $\frac{1}{k+2}$ for $-2 < k < 1$, we find the following system size dependence

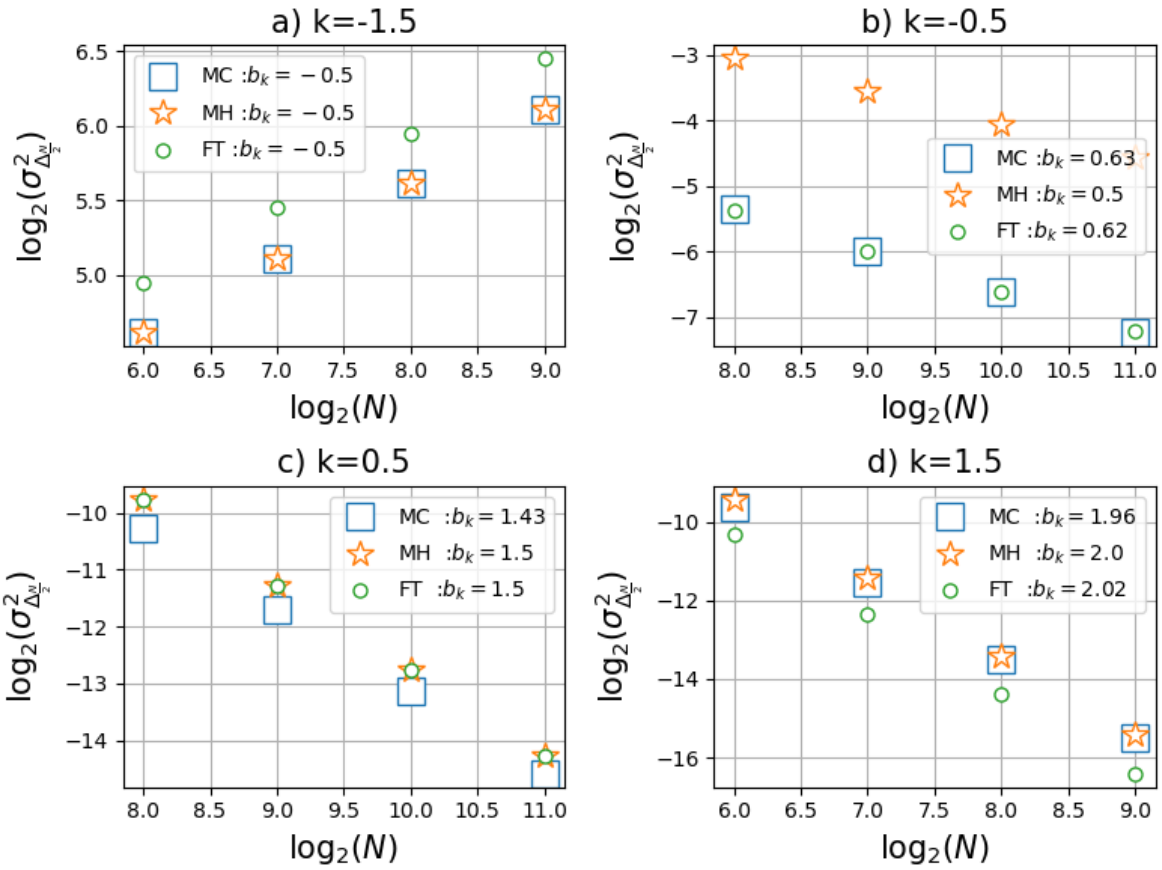

Figure 2.5: Comparison of actual values of the variance of mid-gap calculated using all three techniques, MC, MH and FT for $\beta = 1$.

of the matrix elements (see Appendix. A.2):

$$M_{ii} \sim \begin{cases} \mathcal{O}\left(N^2\right) & \text{for} \quad k > 1 \\ \mathcal{O}\left(N^{k+1}\right) & \text{for} \quad 0 < k < 1 \\ \mathcal{O}\left(N^{2(k+1)/(k+2)}\right) & \text{for} \quad -2 < k < 0, \end{cases} \tag{2.27}$$

$$M_{i\neq j} \sim \begin{cases} 0 & \text{for} \quad k > 1 \\ \mathcal{O}\left(N^{k+1}\right) & \text{for} \quad -2 < k < 1, \end{cases} \tag{2.28}$$

where we have ignored terms with $|i - j| \sim \mathcal{O}(N)$. Assuming that the inverse of the dominant term of the matrix M dictates the scaling of the variance we arrive at the conjecture on the form of b_k in Eq. (2.9). From Eq. (2.25), it is easy to compute the variance of middle gap $\Delta_{N/2}$ given by $\langle \delta\bar{\Delta}^2_{N/2} \rangle = [(\beta M)^{-1}]_{\frac{N}{2}\frac{N}{2}}$. This can be easily evaluated by

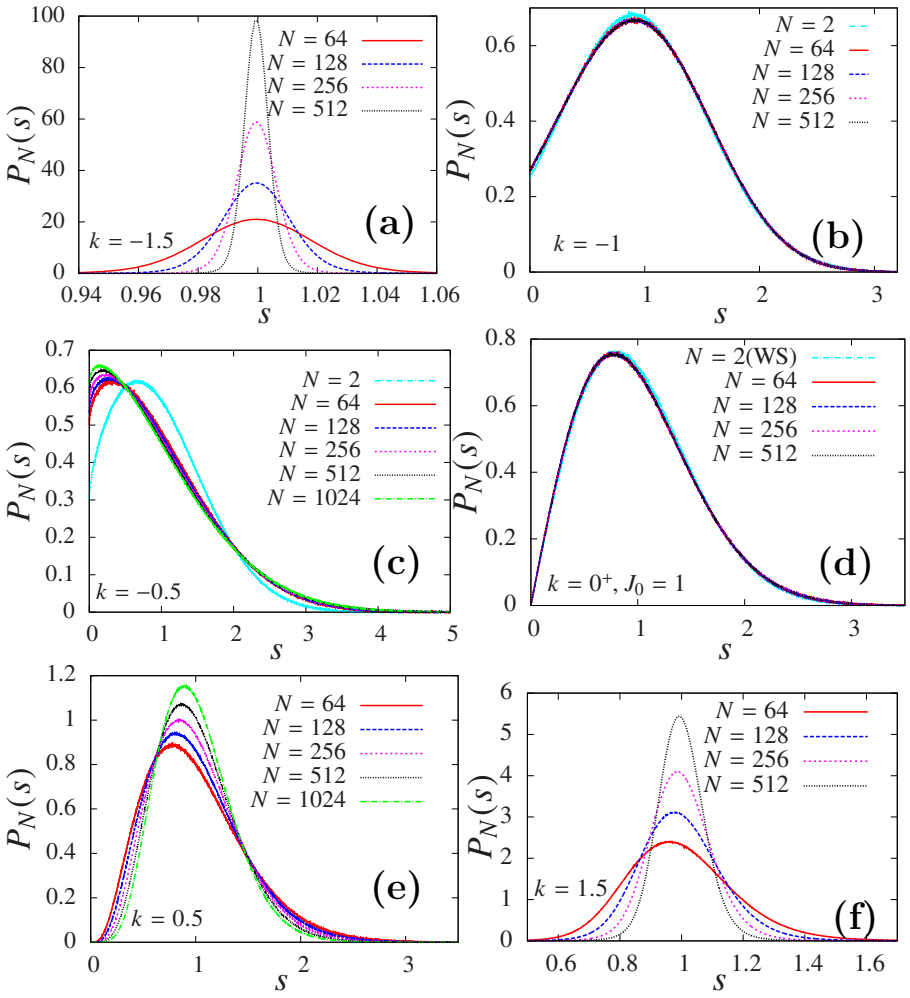

Figure 2.6: Plot of distributions $P_N(s)$ for different values of k and N. Except for the 1DOCP (b) and log-gas (d), for other values of k, we do not see convergence in N which naturally implies that it is different from $P_2(s)$ and hence there is no generalization of WS.

numerically inverting the matrix M and we find the following scaling of the variance of middle gap

$$\sigma^2_{\Delta_{N/2}} \sim \begin{cases} \mathcal{O}\left(N^{-2}\right) & \text{for } k > 1 \\ \mathcal{O}\left(N^{-(k+1)}\right) & \text{for } 0 < k < 1 \\ \mathcal{O}\left(N^{-2(k+1)/(k+2)}\right) & \text{for } -1 < k < 0 \\ \mathcal{O}\left(N^{-(k+1)}\right) & \text{for } -2 < k < -1, \end{cases} \tag{2.29}$$

which match remarkably well with the large-N scaling obtained from MC simulation.

The N dependence of the variance as given in Eq. (2.9) is verified numerically and

presented in Fig. 2.3. However, this does not contain information on the actual values obtained using different methods (MC MH and FT). This comparison is presented in Fig. 2.5. While the slopes are consistent with the conjecture, the actual values do not always match which is not surprising. We find that whenever microscopic Hessian and Monte-Carlo system size scaling agree [$k \notin (-1, 0)$], they even match quantitatively for large-N. Remarkably, in the region $-1 < k < 0$, the Monte-Carlo and field theory results match quantitatively as well.

2.4 Results for distribution of gap

Having examined the average and variance of bulk gaps, we now turn our focus to analyze the distribution of these gaps. For the distribution of eigenvalues of random matrices belonging to the three Gaussian ensembles, characterized by Dyson indices $1, 2, 4$ (which correspond to $\beta J_0 = 1, 2, 4$ for our log-gas), $P_{N\to\infty}(s)$ is accurately described by $P_2(s) = P_{N=2}(s)$ (which is basically the WS) and is given by $A_0 s^{\beta J_0} e^{-B_0 s^2}$where A_0 and B_0 are constants depending on βJ_0 [5]. From our simulations, we in fact find that the surmise for the log-gas is quite accurate for all $\beta J_0 > 1$. We now examine the distribution $P_N(s)$ for other values of k. Interestingly, we find that for $k = -1$ (and similarly for the log-gas), the distribution converges very quickly as the system size N increases, as shown in Figs. 2.6(b) and 2.6(d). On the other hand for other values of k there is no convergence. In particular, for the CM model ($k = 2$), our findings (see Sec. 2.6) are thus in disagreement with the generalized version of WS proposed in Ref. [67]. For generic values of k, as seen in Fig. 2.6, the distributions $P_N(s)$ do not show convergence with N. Hence, we look at the distribution of the following natural scaling variable

$$\tilde{s}_j = \frac{\Delta_j - \langle \Delta_j \rangle}{\sigma_{\Delta_j}}. \tag{2.30}$$

The distribution of this quantity defined as $\tilde{P}_N(\tilde{s}) = \frac{1}{N-1} \sum_{i=1}^{N-1} \langle \delta(\tilde{s} - \tilde{s}_i)$, is computed numerically for different values of k and N. In Fig. 2.7, we plot $\tilde{P}_N(\tilde{s})$ for $k = -1.5, -0.5, 0.5$ and $k = 1.5$. We find that $\tilde{P}_N(\tilde{s})$ tends to a Gaussian form with zero mean and unit variance in the limit $N \to \infty$, except in the range $-1 \leq k \leq 1$. Interestingly, in the range

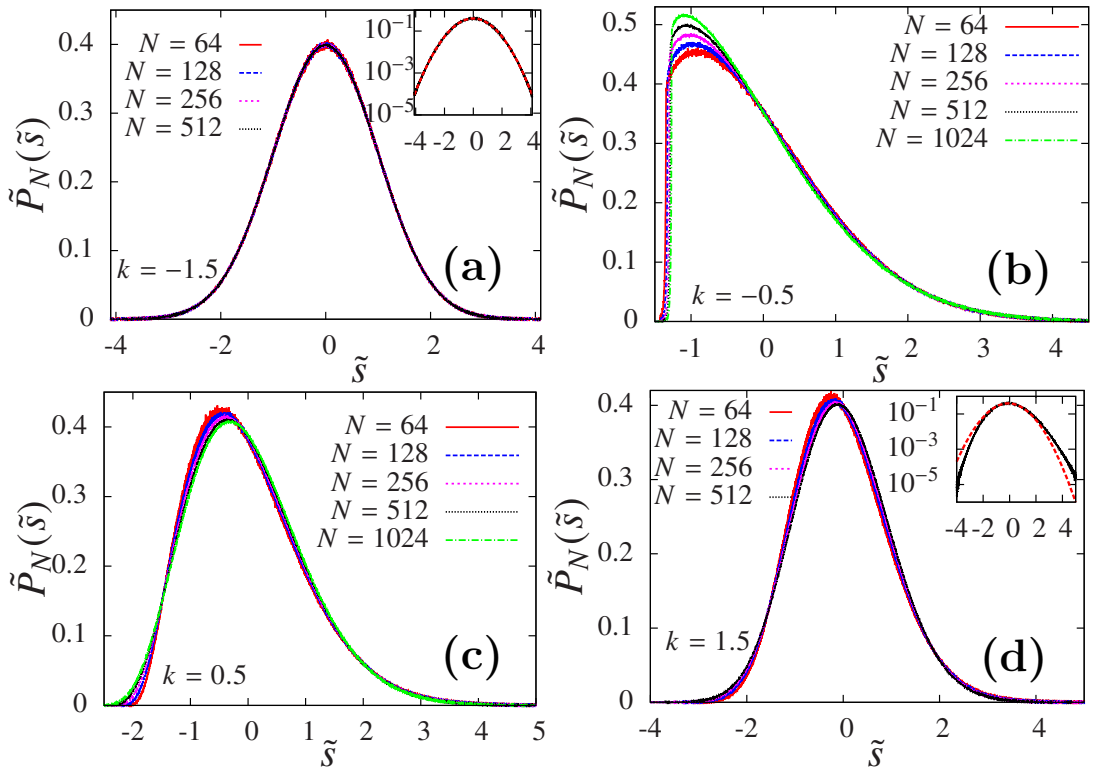

Figure 2.7: Plot of $\tilde{P}_N(\tilde{s})$ for different values of k and N. The distributions for $k = \pm 1.5$ are fitted with a Gaussian over two standard deviations (insets). This is generally observed for $k \notin [-1, 1]$. The distributions for $k = \pm 0.5$ are very different from Gaussian and this is generally the case for $k \in [-1, 1]$.

$-1 < k < 0$, we do not see convergence with N (Fig. 2.7b). In the range $0 < k < 1$ relative fluctuations die out with N in which case one might expect a Gaussian scaling form. Surprisingly, even though the MH nicely predicts the correct scaling exponent b_k the scaling form of the distribution is non-Gaussian (Fig. 2.7c).

Having discussed the main findings of our work, we now mention a few interesting features in the gap statistics in Riesz gas for $-1 \leq k \leq 0$ followed by a discussion on the spacing distribution $P_N(s)$ for the Calogero-Moser system.

2.5 Interesting aspects of the gap statistics for $-1 \leq k \leq 0$

The system size dependence of relative fluctuations $\frac{\sigma_{\Delta_i}}{\langle \Delta_i \rangle}$ in the bulk is characterized by the exponent $(a_k - b_k/2)$. From the conjecture as given in Eq. (2.9), the exponent $(a_k - b_k/2)$

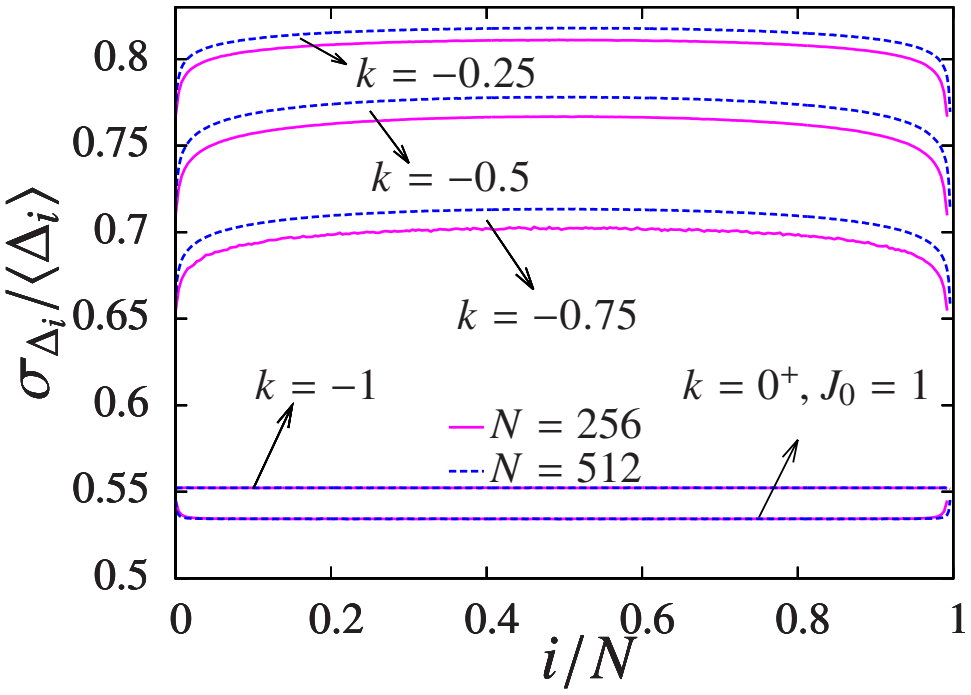

Figure 2.8: Relative fluctuations $\frac{\sigma_{\Delta_i}}{\langle\Delta_i\rangle}$ are shown as a function of i for different system sizes N as well as for different k in the regime $-1 \leq k \leq 0$ for two different system sizes ($N = 256$ in pink solid line and $N = 512$ in blue dashed line). For -1 $< k <$ 0, from our numerics we find that $a_k - b_k/2$ is slightly different from zero, possibly due to finite size effects, hence we get a system size dependence in the relative fluctuation as well. (Inverse temperature β is taken to be unity.)

is zero throughout the range $-1 \leq k \leq 0$. We believe that the slight deviations from the predictions for a few values of k are due to finite size effects. Interestingly, in the range $-1 \leq k \leq 0$, we find that the relative fluctuations have a weak dependence on i, in the bulk (with almost independent for $k = -1, 0^+$). This is shown in Fig: 2.8. We find that, not only do the relative fluctuations $\frac{\sigma_{\Delta_i}}{\langle\Delta_i\rangle}$ have small variations with i, but also the spacing distributions $p_N^{(i)}(s) = \langle\delta(s - s_i)\rangle$ for individual gaps are also almost the same (see Fig. 2.9). However, we expect the differences between $P_N(s)$ and $P_N^i(s)$, for i in bulk, to show up at very small and very large s where edge statistics (e.g $i = 1$) could start dominating over bulk behavior.

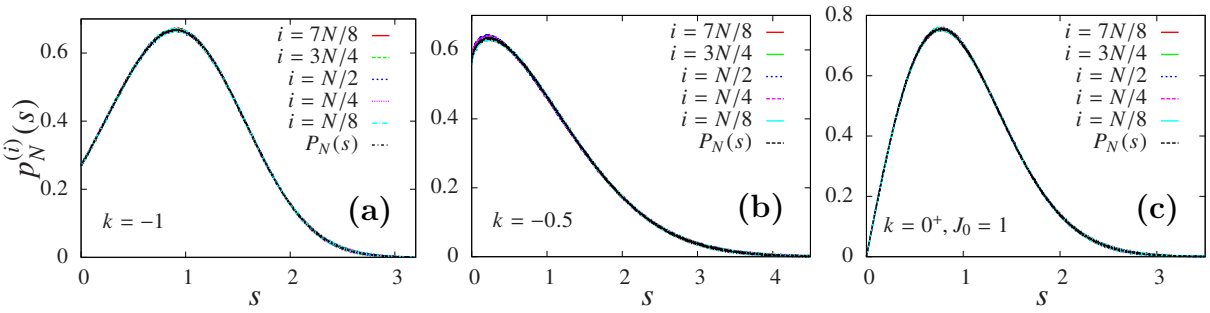

Figure 2.9: The distributions of the i-th normalized gap $p_N^{(i)}(s) = \langle \delta(s - s_i) \rangle$ are shown in the regime $-1 \leq k \leq 0$. It is clear that $p_N^{(i)}(s)$ is independent of i. In these figures we have taken $N = 256$ at inverse temperature $\beta = 1$.

2.6 Spacing distribution in the Calogero-Moser system

For the CM model ($k = 2$), it was claimed in Ref. [67] that the spacing distribution follows a form analogous to the WS, namely,

$$P_N(s) = A\, e^{-\frac{B^2}{s^2} - Cs}, \tag{2.31}$$

where $B = 1.46$ is a fitting parameter while A and C are fixed from the two equations:

$$\int_0^\infty P_N(s)ds = 1 \text{ and } \int_0^\infty sP_N(s)ds = 1. \tag{2.32}$$

However, our results for this system differ from this claim. For the CM model, we found that the distribution, $P_N(s)$, of s does not in fact converge with increasing N, which thus indicates that the generalization of the Wigner surmise does not work here. We believe that the disagreement can be attributed to the 'picket fence' (PF) approximation ($x_j \sim j$) used in the numerical computation of the level spacing distribution in Ref. [67]. Using this approximation, the Lax matrix $\tilde{L}$ takes the form

$$\tilde{L}_{nm} = p_n \delta_{nm} + \frac{i}{2} \frac{1 - \delta_{nm}}{(n - m)}, \tag{2.33}$$

where p_n is chosen from a uniform distribution between -1 and 1. From the eigenvalues of

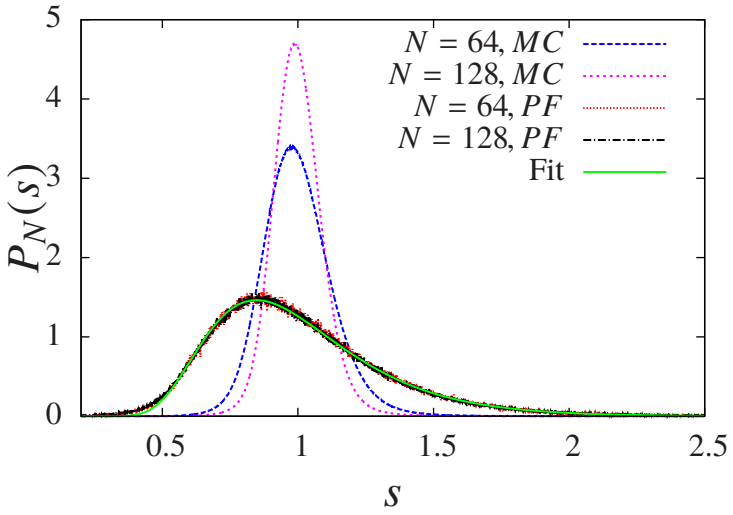

Figure 2.10: Comparison of the level spacing distribution using 'picket fence (PF)' approximation and the actual distribution using Monte-Carlo simulation (MC). The distribution using PF approximation is fitted with the Eq. (2.31) (Fit) with parameters $A = 410.354, B = 1.160, C = 4.441$. We observe that there is no convergence of the actual level spacing distribution (MC) with system size. (Inverse temperature β is taken to be unity.)

$\tilde{L}$, the level spacing distribution was obtained and shown to follow the expression Eq. 2.31. Using this method we can indeed verify (see Fig. 2.10) that the level spacing distribution converges to an N-indepependent form that is described by a WS-like distribution. On comparing the level spacing distribution obtained using the above approximation (denoted by PF in Fig. 2.10) with the actual level spacing distributions (denoted by MC), we observe that they are completely different. In particular, for the true distribution, we find that there is no convergence as the system size grows.

2.7 Summary and outlooks

In this work, we studied the nearest-neighbor gap statistics for a harmonically confined Riesz gas, particularly focusing on the variance and the distribution. The variance of the bulk gap is characterized by the exponent b_k, for which we conjectured a form, Eq. (2.9), for the k-dependence. We supported this conjecture through direct Monte-Carlo simulations and numerics based on small fluctuation theories such as microscopic Hessian and quadratic field theory. We analyzed the normalized gap distribution, $P_N(s)$, and found convergence with N for $k = 0^+$ and $k = -1$. For other values of k, $P_N(s)$ did

not converge with increasing N. This led us to study $\tilde{s}_i$ [gap normalized by fluctuations, see Eq. (2.30)]. As summarized in Fig. 2.1, for $-2 < k < -1$ and $k > 1$, we found that the scaling form of $\tilde{P}_N(\tilde{s})$ was Gaussian, while for all other k values, we observed strong non-Gaussian behavior. In fact, for $-1 < k < 0$, we found that there was no convergence with N. Moreover, in this regime, the fluctuations are of the same order as the mean, leading to the failure of the Hessian theory. Remarkably, the quadratic field theory approach was able to predict the expected scaling exponent even in this regime. We emphasize that the analytical microscopic treatment of fluctuations is extremely difficult. We proposed two different analytical approaches that successfully captured the main features observed in direct simulations: (i) mapping between the microscopic variables and the coarse-grained macroscopic density field, which provides enormous simplification for the otherwise intractable and highly non-local microscopic model, and (ii) the Hessian approximation, which results in an all-to-all connected harmonic network and provides a powerful tool for tackling long-ranged systems. We also discussed a few interesting features in the gap statistics that exist in the $-1 < k < 0$ regime. For the Calogero-Moser system, our findings suggested that there is no generalization of the Wigner surmise as claimed in Ref. [67].

Some interesting outstanding problems include understanding the non-Gaussian behavior, including large deviations, of the gap distribution and its analytical derivation for special cases such as the CM model ($k = 2$) and hard rods ($k \to \infty$). Future research directions include studying the statistics of gaps between any two particles (not just nearest neighbors), which corresponds to the classical analog of the spectral form factor. Investigating how different systems (distinguished by the exponent k) thermalize would also be an interesting and challenging question. Additionally, examining the effects of variations in temperature and the confining potential on the results are promising directions to pursue.

In the next chapter, we discuss the effect of tuning the range of interaction on the equilibrium density profiles specifically in two models: 1DOCP and log-gas.

Chapter 3

Crossover in densities of confined particles with finite range of interaction

In a pure Coulomb interaction, the potential energy between two charges present in three dimensions decreases inversely with the separation between them. Since the power-law exponent (= 1) is less than the dimensionality of the system (= 3), this is a long-range interaction [16, 17]. However, in physical systems, the presence of other charges causes the interaction potential between two particles to be screened, resulting in a finite-ranged interaction. Understanding the finite-ranged interactions is essential for accurately modeling and predicting the behavior of many-body systems in condensed matter and soft matter physics [125–129]. In this chapter, to account for the finite range of interactions, we consider a generalized version of the one dimensional Riesz gas as described in Eq. (1.7). For the convenience, we rewrite the energy function [99]

$$\mathscr{E}(\{x_j\}) = \frac{1}{2}\sum_{i=1}^{N} x_i^2 + \frac{J\ \mathrm{sgn(k)}}{2} \sum_{\substack{i\neq j=1 \\ |i-j|\leq d}}^{N} \frac{1}{\mid x_i - x_j \mid^k},\ \forall\ k > -2. \tag{3.1}$$

As in the previous chapter, we have omitted the subscript k in the energy function to simplify the notation. The parameter d in Eq. (3.1) determines the number of particles each particle is allowed to interact with on either side (left or right) of it, if available.

When $d = N - 1$, the energy function in Eq. (3.1) reduces to the all-to-all coupled (ATAC) model as given in Eq. (1.3) in which each particle interacts with every other particle present in the system. For $d \sim \mathcal{O}(1)$, each particle can interact only with a few other particles. Such a system is called short-ranged (SR). By tuning the fraction $f = \frac{d}{N}$ from 1 to 0 in the large N limit, one can go from the ATAC regime ($f = 1$) to the SR regime ($f = 0$). We call systems with intermediate values of f *i.e.,* $0 < f < 1$ to be finite ranged (FR).

In thermal equilibrium at temperature $T = \beta^{-1}$, the generalized version of Riesz gas system in Eq. (3.1) can be described by the Boltzmann distribution

$$\mathscr{P}_G(\{x_j\}) = e^{-\beta \mathscr{E}(\{x_j\})}/\mathscr{Z}_N(\beta), \tag{3.2}$$

where $\mathscr{Z}_N(\beta)$ is the partition function of the system at inverse temperature β. The first natural question: what is the equilibrium density profile of the particles? Recall that for the ATAC case ($f = 1$), by developing a large-N field theory, the average thermal density has been calculated for any $k > -2$ in Ref. [97] at small temperature [$\beta^{-1} \sim \mathcal{O}(1)$]. It was observed that the average thermal density for large N is independent of the temperature of the system and has a finite support for all $k > -2$, although the support explicitly depends on the power-law exponent k (see Eqs. (2.2)-(2.6)) [97].

While these results are valid for the ATAC case of Riesz gas *i.e.,* for $f = 1$, they are expected to get modified for other values of $f < 1$. Moreover, in most of the physical systems, the particles do not interact with all other particles and hence the interactions are not all-to-all coupled. It is important to study the effect of the parameter f on different physical quantities of the system. The basic physical quantity that one would naturally consider is the average equilibrium density profile and study how the density profile changes with f in the large N limit. Recently, the equilibrium density profile for the SR case ($f = 0$) has been computed in Ref. [99]. In this paper, after developing a large-N field theory similar to the all-to-all coupling case, the density profile was obtained analytically for $\beta \sim \mathcal{O}(1)$. It was found that in the SR case, the density profile is drastically different compared to the ATAC scenario for Riesz gas with $k \leq 0$. However, interestingly, for $k > 0$ the shape of the density profile in the SR case remains same as in

the ATAC case [99]. Natural questions arise: what is the density profile for intermediate f *i.e.,* for $0 < f < 1$? How does the shape of the density profile change as f is tuned from 1 to 0 while keeping the temperature fixed at $\mathcal{O}(1)$ value? In this chapter, we address this question for two specific systems: 1DOCP and log-gas which correspond to $k = -1$ and $k = 0^+$ cases of the energy function in Eq. (3.1), respectively. A similar question was studied in the context of random matrix theory in Ref. [101], where a change in the spectral density profile from the Wigner semi-circle to a Gaussian form was observed as the strength of the interaction was varied smoothly from a very high value to a low value. With decreasing interaction strength, the entropy starts taking part in balancing the confining effect of the harmonic trap. At a very small value of the interaction strength, only entropic contribution is dominant and one observes a Gaussian distribution as one would see for non-interacting particles inside a harmonic trap. Same interaction strength (or equivalently temperature) tuned crossover of spectral density was observed in the context of invariant β-Wishart ensembles as well [102].

For the 1DOCP and log-gas models, we demonstrate a crossover in the density from a finitely supported profile to a Gaussian form as the parameter f is tuned from 1 to 0 [103]. For the 1DOCP model, we obtain an analytical expression for the density profile for any $f \in (0, 1]$ in the large N limit, while for the log-gas model, we provide approximate analytical calculations to understand the density profiles for f close to 1 and 0, separately. For other values of $k > -2$, we numerically demonstrate a similar crossover in the density profile.

The rest of the chapter is organized as follows. In Sec. 3.1, we define the main physical quantity of interest and give a quick summary of important previous results. We provide the summary of our findings in Sec. 3.2 along with numerical demonstrations of the density crossover in both systems. In Sec. 3.3, we study the density crossover in 1DOCP ($k = -1$) by solving saddle point equations for $f \in (0, 1]$. We present this solution in two parts, for $1/2 \leq f \leq 1$ in Sec. 3.3.1 and for $0 < f < 1/2$ in Sec. 3.3.2, respectively. Then in Sec. 3.4, we study the density crossover in the log-gas ($k \to 0$) model. Along with the numerical results, we provide approximate analytical calculations to understand the density profiles both in the $f \to 1$ and $f \to 0$ limits. Finally, in Sec. 3.5, we summarize our study along with some interesting future directions. Some details of the

calculations and numerical simulations are relegated to the Appendices. The details of numerical methods used in this paper are given in Appendix. A.1. The derivation of the saddle point equations are presented in Appendix. A.3. Some details pertaining to the solution of the saddle point equations in the 1DOCP case are provided in Appendix. A.4. In Appendix. A.5, we numerically demonstrate similar density crossover in the general Riesz gas model defined in Eq. (3.1) for other values of k.

3.1 Definitions and relevant previous results

We consider FR Riesz gas consisting of N particles in thermal equilibrium at temperature $\beta^{-1} \sim \mathcal{O}(1)$. We focus on the two choices of the interaction potentials, 1DOCP and log-gas for which the microscopic energy functions are given explicitly as

$$\begin{aligned} \mathscr{E}(\{x_j\}) &= \frac{1}{2}\sum_{i=1}^{N} x_i^2 + \frac{1}{2}\sum_{i=1}^{N}\sum_{\substack{j=\max(i-d,1)\\ j\neq i}}^{j=\min(i+d,N)} V(x_i - x_j), \\ \text{with } \; V(x) &= \begin{cases} -|x|, & \text{for 1DOCP,} \\ -\log(|x|) & \text{for log-gas.} \end{cases} \end{aligned} \tag{3.3}$$

In Eq. (3.3), we have set the strengths J and J_0 of the interaction potentials, respectively, for 1DOCP and log-gas to 1 in this chapter.

In these systems, we are interested in computing the average equilibrium density profile $\varrho_N(x) = \langle \rho_N(x) \rangle_T$, where the empirical density $\rho_N(x)$ is defined as $\rho_N(x) \equiv \frac{1}{N}\sum_{i=1}^{N} \delta(x - x_i)$, and the average $\langle ... \rangle_T$ is performed over the Boltzmann distribution in Eq. (3.2). In the large N limit, the multiple integrals required in order to compute the average $\langle ... \rangle_T$, can be converted to a functional integral over fluctuating density profiles weighted appropriately by a free energy functional $\Psi[\rho_N(x)]$ written in terms of the empirical density, $\rho_N(x)$ [36, 97, 99]. The free energy functional $\Psi[\rho_N(x)]$ for a given density profile $\rho_N(x)$ has two parts

$$\Psi[\rho_N(x)] = \mathscr{E}[\rho_N(x)] - \beta^{-1}\mathcal{S}[\rho_N(x)], \tag{3.4}$$

where $\mathscr{E}[\rho_N(x)]$ is the energy functional and $\mathcal{S}[\rho_N(x)] = -N\int_{-\infty}^{\infty} dx\rho_N(x)\log[\rho_N(x)]$ is the entropy functional [36]. The energy functional needs to be determined from the microscopic energy function in Eq. (3.3) and in general should contain a self energy term and the bulk energy term [36, 130].

In terms of the free energy functional $\Psi[\rho_N(x)]$, the partition function of the system can be written (up to an overall multiplicative factor) as [36, 97, 99]

$$\mathscr{Z}_N(\beta) \sim \int d\mu \int \mathcal{D}[\rho_N(x)] \exp\Big[-\beta\bar{\Psi}[\rho_N(x)]\Big], \tag{3.5}$$

where $\int \mathcal{D}[\rho_N(x)]$ denotes functional integration over density function $\rho_N(x)$ and

$$\bar{\Psi}[\rho_N(x)] = \Psi[\rho_N(x)] - \mu\left(\int dx\rho_N(x) - 1\right). \tag{3.6}$$

Note μ is a Lagrange multiplier that ensures the normalization of the density profile to unity. In the large N limit, the equilibrium density profile $\varrho_N(x)$ can be obtained by solving the saddle point equations (SPEs) [97, 99]

$$\frac{\delta\bar{\Psi}[\rho_N(x)]}{\delta\rho_N(x)}\Big|_{\rho_N(x)=\varrho_N(x)} = 0, \quad \text{and} \quad \frac{\partial\bar{\Psi}}{\partial\mu} = 0. \tag{3.7}$$

For fixed f it is possible to show that in the large N limit, the energy functional scales as $\sim N^{\Lambda}$ with $\Lambda \geq 1$. This fact has been proved for Riesz gas with general k (> -2) for $f = 1$ and $f = 0$ in Refs. [97] and [99] respectively. Additionally, in the large N limit one can show (see Appendix. A.3) that for fixed $f \in (0, 1]$ the contributions from the entropy and the self energy are much smaller compared to the bulk energy term and consequently, they can be neglected while solving the SPEs.

Before going into the details of the derivation and presentation of the results for the FR case ($0 < f < 1$), we discuss some of the relevant results obtained previously for ATAC ($f = 1$) and SR ($f = 0$) cases.

3.1.1 Equilibrium density profile in the ATAC case ($d = N - 1$ *i.e.,* $f = 1$)

In this case, the entropy as well as the self energy terms are subdominant compared to the bulk energy part in the free energy [36,97]. Neglecting these contributions, minimizing the free energy functional essentially becomes minimizing the (bulk) energy functional. One finds that the average density $\varrho_N(x)$ is described, for both 1DOCP and log-gas systems, by the following scaling form [97]

$$\varrho_N(x) = \frac{1}{N^\alpha}\tilde{\varrho}_1\left(\frac{x}{N^\alpha}\right), \quad \text{with} \quad \alpha = \begin{cases} 1 & \text{for} \quad \text{1DOCP} \\ \frac{1}{2} & \text{for} \quad \text{log-gas,} \end{cases} \tag{3.8}$$

with scaling functions given explicitly by

$$\tilde{\varrho}_1(y) = \begin{cases} \frac{1}{2} & \text{for} \quad -1 \le y \le 1 \quad \text{in 1DOCP} \\ \frac{1}{\pi}\sqrt{2-y^2} & \text{for} \quad -\sqrt{2} \le y \le \sqrt{2} \quad \text{in log-gas.} \end{cases} \tag{3.9}$$

We would like to emphasize that these scaling functions correspond to the equilibrium densities of particles under conditions of $\mathcal{O}(1)$ temperature and large N. In such scenarios, the contribution from entropy can be disregarded when solving the SPEs. However, as the temperature increases, the entropy's influence becomes increasingly significant. Consequently, the solution of the SPE deviates from those presented in Eqs. 3.8 and 3.9. This phenomenon has been rigorously examined within the framework of random matrix theory [101, 102], wherein instead of raising the temperature, the interaction strength is diminished. This adjustment leads to a cooperative interplay between energy and entropy, working together to counterbalance the confinement imposed by harmonic trapping.

3.1.2 Equilibrium density profile in SR case ($d \sim \mathcal{O}(1)$ *i.e.,* $f = 0$)

Contrary to the previous case, the entropy term in this case dominates over the interaction energy term in the 1DOCP system. However, for the log-gas the entropy, the self energy and the bulk interaction energy all contribute at the same order [99]. The density profiles

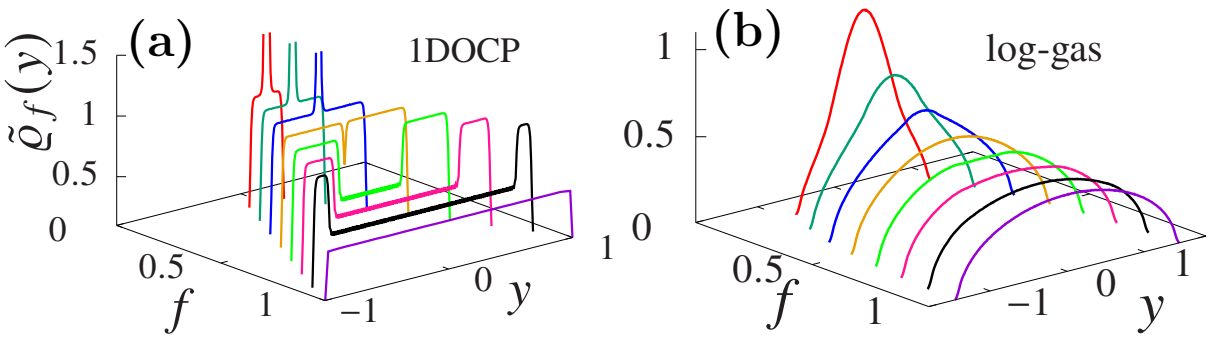

Figure 3.1: Demonstration of the crossover in the density profiles in (a) 1DOCP and (b) log-gas systems. For both the systems we plot the scaled density profile $\tilde{\varrho}_f(y) = N^\alpha \varrho_N(yN^\alpha)$ as functions of y [see Eq. (3.11)] for eight values of $f = n/8$ with $n = 1$ (red), 2 (dark-green), 3 (blue), 4 (brown), 5 (green), 6 (dark-pink), 7 (black), and 8 (violet). For 1DOCP model, the profile transitions from a flat profile at $f = 1$ to a delta function profile in the $f \to 0$ limit. The peaks of the delta functions on the z-axis are cut in order to display the features of the density profiles for f close to 1. For the log-gas, the density profile changes its shape [shown in figure (b)] from Wigner semi-circle at $f = 1$ to bell-shaped at small f. For both cases we observe that the total support of the density profile decreases as f is reduced. The plots of density profiles are obtained numerically for $N = 128$ for both systems. Details of the numerical simulation are provided in A.1.

in this case for large-N are given by [99]

$$\varrho_N(x) = \varrho_0(x), \quad \text{where,} \quad \varrho_0(x) = \begin{cases} \sqrt{\frac{\beta}{2\pi}} \exp(-\beta x^2/2) & \text{for 1DOCP} \\ \sqrt{\frac{\beta}{2(\beta d+1)\pi}} \exp(-\frac{\beta x^2}{2(\beta d+1)}) & \text{for log-gas.} \end{cases} \tag{3.10}$$

In contrast to the ATAC scenario ($f = 1$), the equilibrium density profiles in the SR case remain independent of the system size N and are of Gaussian form.

3.2 Summary of the results

As mentioned in the previous section, the equilibrium density profiles are dramatically different for the ATAC ($f = 1$) and the SR ($f = 0$) case. In this chapter, we investigate how the density profiles cross over from finitely supported profiles to infinitely extended Gaussian profiles as f is decreased from 1 to 0. We find that in both models, the density profiles for large N and fixed f consist of three parts: one central part extending over region $x \in [-\ell_N, \ell_N]$ and two symmetric edge parts supported over regions $[-b_N, -\ell_N)$

and $(\ell_N, b_N]$, respectively, where $0 < \ell_N < b_N$. At low temperature ($T \sim \mathcal{O}(1)$), these three regimes naturally appear because the interactions felt by a particle in these regimes are different. For $f < 1$, the central part contains $|1-2f|$ fractions of particles where each particle can interact either with $2d$ other particles or the remaining $(N-1)$ particles depending on whether $2d < (N-1)$ or not. On the other hand, the remaining fraction of particles residing on the edges always find less than d particles on at least one side, either left or right. The lengths of these supports depend on f. As f is changed, the ranges as well as the shape of the profiles in these regimes get modified and one observes the above-mentioned crossover in the density profile as numerically demonstrated in Fig. 3.1 for both 1DOCP and log-gas models. Below, we briefly summarise our main findings [103].

1. We find that for both 1DOCP and log-gas, the equilibrium density profile for fixed f in the large N limit, possesses the following scaling form,

$$\varrho_N(x) = \frac{1}{N^\alpha}\, \tilde{\varrho}_f\left(\frac{x}{N^\alpha}\right), \quad \text{with} \begin{cases} \alpha = 1, & \text{for 1DOCP,} \\ \alpha = \frac{1}{2}, & \text{for log-gas.} \end{cases} \tag{3.11}$$

   Note even for $f < 1$, the density profile satisfies the same scaling form as in the ATAC case given in Eq. (3.8). The length of the total support of the scaling function $\tilde{\varrho}_f(y)$ remains finite for all $f > 0$ and it decreases as f is reduced from 1 (see Fig. 3.1).

2. We have derived the saddle point equations satisfied by the equilibrium density profiles for both cases (see Appendix. A.3).

3. For the 1DOCP case, one can solve the SPEs for arbitrary values of $f \in (0, 1]$. We find that the scaling function $\tilde{\varrho}_f(y)$, in this case, is given by

$$\tilde{\varrho}_f(y) \;\; = \begin{cases} 1 & \text{for } -f \le y < -(2f-1), \\ \frac{1}{2} & \text{for } -(2f-1) \le y \le (2f-1), \\ 1 & \text{for } \;\; (2f-1) < y \le f, \end{cases} \qquad \text{for } \; \frac{1}{2} \le f \le 1, \tag{3.12}$$

$$\tilde{\varrho}_f(y) \;\; = (1-2f)\delta(y) + \Theta(y+f)\Theta(f-y), \qquad \text{for } \; 0 < f < \frac{1}{2}, \tag{3.13}$$

which describes the crossover in the scaled density profile as f is reduced from 1 to 0. This crossover phenomena is demonstrated in Fig. 3.1(a). In the $f \to 0$ limit, the strength of the delta function part grows and approaches unity which (as shown in Sec. 3.3.2), when zoomed in, essentially corresponds to the Gaussian profile given in Eq. (3.10) in terms of the unscaled variable x as obtained previously in Ref. [99].

4. For the log-gas case, we numerically demonstrate the crossover of density profile from Wigner semi-circle to Gaussian form as f is decreased from 1 to 0 (see Fig. 3.1(b)). Solving the SPEs for arbitrary values of f seems difficult in this case. We find approximate solutions for the density profiles for f close to 1 and 0. In the former case, we find that the scaling function for the density can approximately be described by [39]

$$\tilde{\varrho}_f(y) \approx \frac{1}{\pi}\sqrt{\frac{(y^2-\tilde{a}^2)(\tilde{b}^2-y^2)}{(y^2-\tilde{\ell}^2)}}, \tag{3.14}$$

which exists on a three-cut support $[-\tilde{b},-\tilde{a}]$, $[-\tilde{\ell},\tilde{\ell}]$, and $[\tilde{a},\tilde{b}]$ with $0<\tilde{\ell}<\tilde{a}<\tilde{b}$ and y belongs to any of the intervals in the support. For given $\tilde{\ell}$, the parameters $\tilde{a},\tilde{b}$ can be determined from the relation $\tilde{a}^2+\tilde{b}^2=2+\tilde{\ell}^2$ and the normalisation condition $\int_{\tilde{a}}^{\tilde{b}} \tilde{\varrho}_f(y)dy=(1-f)$ [39]. In our case we determine $\tilde{\ell}$ from the numerically obtained density, $\tilde{\varrho}_{\rm nu}(y)$ using the relation $\int_{-\tilde{\ell}_{\rm nu}}^{\tilde{\ell}_{\rm nu}} \tilde{\varrho}_{\rm nu}(y)dy=(2f-1)$, where the subscript 'nu' stands for numerical value. With increasing f towards unity, the parameters $\tilde{\ell}$ and $\tilde{a}$ in Eq. (3.14) approach to $\tilde{b}$. Exactly at $f=1$, they all become equal to $\sqrt{2}$ and one recovers the density profile in the ATAC case (given in Eq. (3.9)). A comparison of our theoretical result with numerically obtained density is provided in Fig. 3.4 where we observe decent agreement.

For small f, we find that the density profile in the central part can be well described by the following approximate scaling function

$$\tilde{\varrho}_f(y) \approx \frac{1}{\sqrt{2\pi f}}\exp\left(-\frac{y^2}{2f}\right), \quad -\tilde{\ell}\le y\le\tilde{\ell}, \tag{3.15}$$

where $\tilde{\ell}$ is determined from $\int_{-\tilde{\ell}}^{\tilde{\ell}} \tilde{\varrho}_f(y)dy = 1-2f$. This result is consistent with the result in Eq. (3.10) obtained previously in Ref. [99]. To see this one needs

to consider both d and N large in Eq. (3.10), so that the fraction $f = d/N$ is fixed. This essentially means $\tilde{\ell} \to \infty$ as $f \to 0$ in Eq. (3.15). To determine $\tilde{\varrho}_f(y)$ outside the central part, we notice that for small f the solution of the SPE can be approximated by a problem in ATAC log-gas system with a region $[-\tilde{\ell}, \tilde{\ell}]$ deprived of particles. The saddle point solution for this problem is given by [39]

$$\tilde{\varrho}_f(y) \approx \frac{1}{\pi}\sqrt{\frac{y^2\ (\tilde{b}^2 - y^2)}{(y^2 - \tilde{\ell}^2)}} \quad \text{for} \quad \tilde{\ell} < |y| \leq \tilde{b}, \tag{3.16}$$

where $\tilde{b} = \sqrt{\tilde{\ell}^2 + 4f}$ can be obtained from the constraint $\int_{\tilde{\ell}}^{\tilde{b}} \tilde{\varrho}_f(y)dy = f$. We find that this form describes the behavior of the density profile near the edges well (see Fig. 3.5).

3.3 Density crossover in 1DOCP ($V(x) = -|x|$)

In this section, we solve the SPE in Eq. (3.7) for given f to study crossover in the density profile for the 1DOCP model described by the energy function given in Eq. (3.3). For $0 < f < 1$ one gets separate SPEs in the three parts: the central part $[-\ell_N, \ell_N]$, the left edge part $[-b_N, -\ell_N)$ and the right edge part $(\ell_N, b_N]$. These equations, derived in Appendix. A.3, can be solved exactly as shown below. We first present the solution for $1/2 \leq f \leq 1$. For $0 < f < 1/2$, as we will see, one requires to solve the SPEs separately for $1/3 \leq f < 1/2$ and $0 < f < 1/3$.

3.3.1 Solution for $1/2 \leq f \leq 1$:

For fixed f and large N, in order to minimize energy (see Eq. (3.3)), particles settle over a region which scales as $\mathcal{O}(N)$. In this configuration, the contributions from the confining harmonic term and the repulsive interaction term both become order N^3 such that they can compete with each other. Note, on the other hand, entropy is always of order N for $\beta^{-1} \sim \mathcal{O}(1)$. Hence it is expected that the equilibrium density profile possesses the scaling $\varrho_N(x) = \frac{1}{N}\tilde{\varrho}_f(x/N)$ which is also verified numerically in Fig. 3.2 for two representative values of $f > 1/2$. To find the scaling function $\tilde{\varrho}_f(y)$, it seems convenient to rewrite the

SPEs in terms of the scaling variable $y = x/N$ and the scaling functions $\tilde{\varrho}_f(y)$ as given in Eqs. A.21 and A.22. Furthermore, numerical observations from Fig. 3.2 suggest that the equilibrium density profile is piece-wise uniform. This leads us to make the following ansatz for the saddle point density profile

$$\tilde{\varrho}_f(y) = \begin{cases} \tilde{\varrho}_{\rm edge} \text{ for } -\tilde{b} \le y < -\tilde{\ell} \\ \tilde{\varrho}_{\rm mid} \text{ for } -\tilde{\ell} \le y \le \tilde{\ell} \\ \tilde{\varrho}_{\rm edge} \text{ for } \tilde{\ell} < y \le \tilde{b}, \end{cases} \tag{3.17}$$

where $\tilde{\ell} = \ell_N/N$ and $\tilde{b} = b_N/N$. Note there are six unknown constants, namely, $\tilde{\varrho}_{\rm edge}$, $\tilde{\varrho}_{\rm mid}$, $\tilde{b}$, $\tilde{\ell}$ and the chemical potentials $\tilde{\mu}_1$ and $\tilde{\mu}_2$, which are required to ensure appropriate normalizations of the density profiles in respective parts [see Eq. (A.2)]. Inserting the above form of the scaled density profile in SPEs, one finds six equations which determine the values of these constants. Since the calculations to find these six constants are involved and lengthy, we present the details of this calculation in Appendix. A.4.1. Here, we only present the final result:

$$\begin{aligned} &\tilde{\varrho}_{\rm edge} = 1, \qquad \tilde{\varrho}_{\rm mid} = \frac{1}{2}, \\ &\tilde{\ell} = (2f-1), \quad \tilde{b} = f, \\ &\tilde{\mu}_1 = \tilde{\mu}_2 = -2\left(f - \frac{1}{2}\right)^2, \end{aligned} \tag{3.18}$$

inserting which in Eq. (3.17) completely determines $\tilde{\varrho}_f(y)$ for $1/2 \le f \le 1$. The theoretical density profile is numerically verified in Fig. 3.2. In Appendix. A.1, we provide all the details of our numerical simulations.

3.3.2 Solution for $0 < f < 1/2$:

In this case also we find that the equilibrium density profile has scaling form $\varrho_N(x) = \frac{1}{N}\tilde{\varrho}_f(x/N)$ which is demonstrated numerically in Fig. 3.3(a). Note that with increasing N, the central part (in terms of the scaling variable $y = x/N$) shrinks to a delta function (see inset of Fig. 3.3(a)) while the profiles in the edge parts are uniform. When this delta

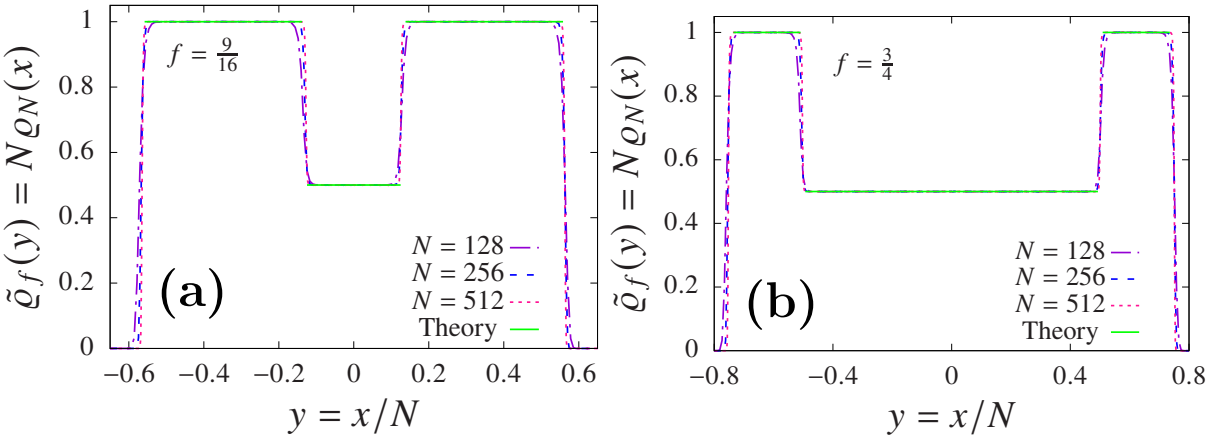

Figure 3.2: Plots of numerically obtained density profiles (dashed lines) for (a) $f = \frac{9}{16}$ and (b) $f = \frac{3}{4}$ in 1DOCP. Collapse of data for different N verifies the scaling relation in Eq. (3.11) with $\alpha = 1$. The solid green lines represent the analytical prediction in Eq. (3.12). We observe good agreement between simulation and theory. With decreasing f, the size of the central region reduces and the edge regions grow.

function is zoomed to the original scale, we observe from Fig. 3.3(b) that, the density profile there can very nicely be described by a Gaussian form in terms of the unscaled variable x. This suggests us to expect the following form for the equilibrium density profile (in terms of the unscaled variable x)

$$\varrho_N(x) = \begin{cases} \rho_{\text{central}}(x) & \text{for } -\ell_N \le x \le \ell_N \\ \rho_{\text{edge}} & \text{for } \ell_N < |x| \le b_N, \end{cases} \tag{3.19}$$

such that $\int_{-\ell_N}^{\ell_N} dx \rho_{\text{central}}(x) = 1 - 2f$, $\rho_{\text{edge}} = f/(b_N - \ell_N)$. This, in turn, suggests us the following form for the scaled density profile:

$$\tilde{\varrho}_f(y) = (1 - 2f)\delta(y) + \tilde{\varrho}_{\text{edge}} \mathbb{1}_{[-\tilde{b},\tilde{b}]}(y), \tag{3.20}$$

where $\tilde{\ell} = \ell_N/N \to 0$ and, $\tilde{\varrho}_{\text{edge}} = N\rho_{\text{edge}}$ and $\tilde{b} = b_N/N$. Note, $\tilde{\varrho}_{\text{edge}}$ and $\tilde{b}$ are $\mathcal{O}(1)$ constants which we need to find. We also show below that $\rho_{\text{central}}(x)$ indeed has a Gaussian form. We first write the SPEs from Eqs. (A.18)-(A.20) (with $V(x) = -|x|$) in terms of the scaling variable $y = x/N$ and the scaled density profile $\tilde{\varrho}_f(y)$. The explicit expression of the SPE on the left edge part $[-\tilde{b}, -\tilde{\ell})$ is given in Eq. (A.32). Here, we rewrite it for

convenience:

$$\frac{y^2}{2} - \int_{-\tilde{b}}^{0_-} |y-y'|\tilde{\varrho}_f(y')dy' \\ - \Big[\int_{0_-}^{y+\bar{\delta}_y}(y'-y)\tilde{\varrho}_f(y')dy' - \frac{1}{2}\Big(\int_{-\tilde{b}}^{y}\bar{\delta}_{y'}\tilde{\varrho}_f(y')dy' + \int_{0_-}^{y+\bar{\delta}_y}\delta_{y'}\tilde{\varrho}_f(y')dy'\Big)\Big] - \tilde{\mu}_2 = 0, \tag{3.21}$$

where we have used the fact $\tilde{\ell} \to 0$ in the large N limit. In fact, we will later show that $\ell_N \sim \mathcal{O}(\sqrt{\log N})$. In the above equation, $\bar{\delta}_y = \bar{\mathcal{D}}_{x=Ny}/N$ and $\delta_y = \mathcal{D}_{x=Ny}/N$ with $\mathcal{D}_x$ and $\bar{\mathcal{D}}_x$, representing the distances from point x, respectively, on the left and right side over which one would find f fraction of particles (see their definitions in Eq. (A.8)). The chemical potential $\tilde{\mu}_2 = \mu_2/N^3$ ensures that the density profile $\tilde{\varrho}_f(y)$ on the left edge is normalized to f. One can write an equation similar to Eq. (3.21) for the right part as well. Owing to the symmetry between the two parts, the calculation on the right part would be exactly the same as in the left part. Therefore, here we only discuss the computations for the left part. Our next task is to insert the ansatz from Eq. (3.20) for the scaled density profile in Eq. (3.21) and evaluate different integrals in this equation. For that, we first need to find the y dependence of $\bar{\delta}_y$ and δ_y explicitly. It turns out that the dependence of these functions on y changes as f decreases below $1/3$. This happens because the number of particles $(1-2f)N$ in the central region changes from being smaller to being larger than the number of particles fN at the edges as f is decreased below $1/3$. Hence, one is required to consider the two cases $1/3 \le f < 1/2$ and $0 < f < 1/3$ separately.

We first discuss the $1/3 \le f < 1/2$ case. The functions $\bar{\delta}_y$ and δ_y are determined in Eq. (A.37) and Eq. (A.39) respectively and they are given by

$$\bar{\delta}_y = \begin{cases} -y & \text{for} \quad -\tilde{b} \le y \le -\tilde{x}_f \\ \tilde{x}_f & \text{for} \quad -\tilde{x}_f \le y < 0_- \\ \tilde{b} & \text{for} \quad y = 0_+, \end{cases} \quad , \quad \delta_y = \begin{cases} y & \text{for} \quad \tilde{x}_f \le y \le \tilde{b} \\ \tilde{x}_f & \text{for} \quad 0_+ < y \le \tilde{x}_f \\ \tilde{b} & \text{for} \quad y = 0_-, \end{cases} \tag{3.22}$$

with

$$\tilde{x}_f = \frac{(3f-1)}{\tilde{\varrho}_{\text{edge}}} \quad \text{for } \frac{1}{3} \le f < \frac{1}{2}. \tag{3.23}$$

We use the above explicit expressions of the functions $\bar{\delta}_y$ and δ_y and the ansatz for $\tilde{\varrho}_f(y)$ from Eq. (3.20) in the SPE (3.21). After performing the integrals in Eq. (3.21) we find the following equations [details are provided in Appendix. A.4.2]

$$\begin{aligned} \Big(1-\tilde{\varrho}_{\text{edge}}\Big)\tfrac{y^2}{2} &\approx \tilde{\mu}_2, && \text{for } -\tilde{b} \le y \le -\tilde{x}_f, \\ (\ \ 1-\tilde{\varrho}_{\text{edge}})\tfrac{y^2}{2} + \tilde{\varrho}_{\text{edge}}\Big(\tfrac{f}{\tilde{\varrho}_{\text{edge}}} - \tilde{b}\Big)y - \tfrac{\tilde{\varrho}_{\text{edge}}}{4} &\quad \Big[\tilde{b}^2 - \Big(\frac{3f-1}{\tilde{\varrho}_{\text{edge}}}\Big)^2\Big] \\ + \tfrac{1}{2}(1-2f)\Big[\tilde{b} - \tfrac{(1-2f)}{2\tilde{\varrho}_{\text{edge}}}\Big] &\approx \tilde{\mu}_2, && \text{for } -\tilde{x}_f \le y < 0_-. \end{aligned} \tag{3.24}$$

Since the above equations are valid for arbitrary y in the respective regions, the coefficients of different powers of y should vanish individually in both the regions of y. Solving the resulting equations, we get

$$\tilde{\varrho}_{\text{edge}} = 1, \quad \tilde{b} = f, \quad \text{and } \tilde{\mu}_2 = 0. \tag{3.25}$$

A similar calculation is performed for the $0 < f < 1/3$ case in Appendix. A.4.2 and once again one finds the same solutions for the constants as in Eq. (3.25). We would like to mention again that a similar calculation can be performed for the SPE on the right edge part and arrive at the same solutions as in Eq. (3.25). Note that the solutions in this equation completely specify the expression of the scaled density profile in Eq. (3.20) which is given explicitly in Eq. (3.13) and verified numerically in Fig. 3.3(a).

We now focus on the central regime which is described by the delta function part of the scaling distribution in Eq. (3.20). However, if one zooms over this region, then one does not find that $(1-2f)$ fraction of particles at the central region are just piled up at the origin. They of course, get spread over a region $[-\ell_N, \ell_N]$ due to the presence of finite temperature, however as we will show below $\ell_N/N \to 0$ as $N \to \infty$. This spreading happens because of the entropy of these particles. As it turns out the net interaction energy of the particles in this region is sub-dominant compared to the entropy. Hence, neglecting the interaction part of the free energy, the SPE in the central region can be written in terms of the un-scaled density profile $\varrho_N(x)$ as

$$N\frac{x^2}{2} + N\beta^{-1}\log[\varrho_N(x)] = \mu_1, \tag{3.26}$$

which has the following solution

$$\varrho_N(x) = \exp\left(\frac{\mu_1}{N} - \beta\frac{x^2}{2}\right). \tag{3.27}$$

Note that the above Gaussian form of the density profile remains valid over the central region $[-\ell_N, \ell_N]$ and it should smoothly connect to the density profile outside the central region on both sides. Furthermore, μ_1 should be such that the fraction of the number of particles inside the central region is $(1-2f)$. These conditions provide the following two equations

$$\exp\left(\frac{\mu_1}{N} - \beta\frac{\ell_N^2}{2}\right) = \frac{1}{N}, \tag{3.28}$$

$$\text{with} \quad \int_{-\ell_N}^{\ell_N} \varrho_N(x)dx = (1-2f). \tag{3.29}$$

Solving these two equations one finds that

$$\ell_N \approx \sqrt{\frac{2}{\beta}\log N}, \quad \text{and} \;\; \exp(\mu_1/N) \approx (1-2f)\sqrt{\frac{\beta}{2\pi}}, \tag{3.30}$$

which completely specify the density profile in Eq. (3.27) in the central region $[-\ell_N, \ell_N]$. This Gaussian form for the density profile is verified in Fig. 3.3(b).

In summary, for fixed $f \in [\frac{1}{2}, 1]$ and large N, the equilibrium density profile is piecewise uniform

$$\varrho_N(x) \approx \begin{cases} \frac{1}{N} & \text{for} \;\; x \in \big[-fN, -(2f-1)N\big), \\ \frac{1}{2N} & \text{for} \;\; x \in \big[-(2f-1)N, (2f-1)N\big] \\ \frac{1}{N} & \text{for} \;\; x \in \big((2f-1)N, fN\big], \end{cases} \tag{3.31}$$

On the other hand for $0 < f < 1/2$, the equilibrium density profile has the following form

$$\varrho_N(x) \approx \begin{cases} \frac{1}{N} & \text{for} \;\; x \in \big[-fN, -\ell_N\big). \\ (1-2f)\sqrt{\frac{\beta}{2\pi}}e^{-\beta x^2/2} & \text{for} \;\; x \in [-\ell_N, \ell_N], \;\text{with}\; \ell_N \sim \mathcal{O}(\sqrt{\log N}) \\ \frac{1}{N} & \text{for} \;\; x \in \big(\ell_N, fN\big], \end{cases} \tag{3.32}$$

for large N. In terms of the scaled variable y, the density profiles in the above equations

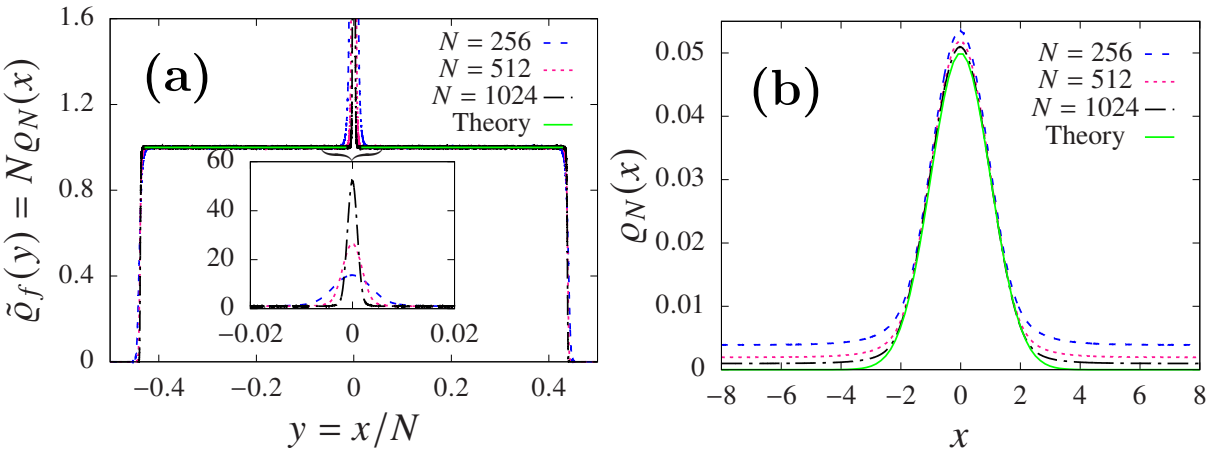

Figure 3.3: (a) System size collapse of scaled density $\tilde{\varrho}_f(y) = N\varrho_N(x)$ for 1DOCP at $f = 7/16$. Data collapse for different N verifies the scaling relation in Eq. (3.11) with $\alpha = 1$ over almost the full range except for a small region around the origin. The green solid line represents a uniform profile on both the left and right edge parts, as described by Eq. (3.13). The inset displays a zoomed version of the central part, where we observe that under scaling $y = x/N$ the density profile for larger N becomes sharper and narrower which is consistent with the delta function in Eq. (3.13). (b) This figure plots the density profile in the central part [zoomed version of delta part in (a)] as functions of unscaled variable x for different N. We observe that the density profile in the central part approaches, with increasing N, to a Gaussian form as given in Eq. (3.32). Simulation data are obtained using $\beta = 1$.

possess the scaling form in Eq. (3.11) with $\alpha = 1$ and the scaling functions are given in Eq. (3.12) and Eq. (3.13). These scaling functions can indeed describe the crossover demonstrated in Fig. 3.1(a). Note, for $f = 1$ these results reproduce the density profile of the ATAC case given in Eq. (3.9) which represents a flat profile existing over a single support $[-N, N]$. As f is reduced from 1, the particles at the edges do not feel the repulsion from all the particles, however, the particles at the central part feel the interaction from all other particles. Consequently, the total support of the profile shrinks to $[-fN, fN]$ and the density profile becomes piecewise uniform over three parts. Since the particles in the central part feel more repulsion than the edge parts, more particles get pushed away from the centre of the trap giving rise to a higher density value in the edge parts than the central part. As f is further reduced, the two edge parts approach each other, causing the central part to shrink and cease to exist at $f = 1/2$. When f is reduced below $1/2$, one does not find a single particle in the system that interacts with all other particles. On the other hand, because of the reduced f, the amount of overall repulsion that the edge

particles can manage to climb against the harmonic potential also got reduced. Hence they get more squeezed leading to an even smaller spread ($2fN$) for the full profile. In this situation to minimize energy, the particles at the central part find themselves easier to sit on top of each other at the minimum of the harmonic trap leading to piling up at the center. At this point, the entropy starts dominating because the contribution from the interaction part of the energy to the free energy becomes negligible. As a result, the particles behave like a non-interacting fluid and get distributed according to the Boltzmann distribution which is a Gaussian in harmonic trap. With decreasing f, more and more particles join the fluid in the central part. In the $f \to 0$ limit the edge parts get completely melted into the fluid part and one finds the density profile to be Gaussian as was obtained in Ref: [99].

3.4 Density crossover in log-gas ($V(x) = -\log|x|$).

The energy function of log-gas is given in Eq. (3.3). In the ATAC ($f = 1$) case, as mentioned earlier, the equilibrium density profile has the Wigner semi-circular scaling form given in Eq. (3.9) [97]. On the other hand, in the SR case ($f = 0$), the equilibrium density profile is Gaussian and the width of the profile depends on the parameter d (see Eq. (3.10)) [99]. As demonstrated in Fig. 3.1(b), the density profile changes from Wigner semi-circle to Gaussian as f is decreased. To understand this crossover in the equilibrium density profile one requires to solve the relevant SPEs for arbitrary $f \in [0, 1]$. While exact solutions for the scaling density function $\tilde{\varrho}_f(y)$ have been obtained for $f = 1$ and $f = 0$, finding the solution for general f seems difficult. However, it turns out that for f close to 1 and 0, one can find approximate solutions to the SPEs, which we discuss below.

3.4.1 Solution for f close to 1:

For $1/2 \leq f \leq 1$ the SPEs in the central, left and right edge parts are derived in Eqs. (A.13 - A.15). Here, we write them explicitly with log-gas interaction $V(x) = -\log(|x|)$. In

the central part $-\ell_N \le x \le \ell_N$ one has

$$N\frac{x^2}{2} - N^2 \int_{-b_N}^{b_N} \log(|x'-x|)\ \varrho_N(x')\ dx' + \frac{N^2}{2}\Big[\int_{-b_N}^{-\ell_N} \log\big(\bar{\mathcal{D}}_{x'}\big)\ \varrho_N(x')\ dx' + \int_{\ell_N}^{b_N} \log(\mathcal{D}_{x'})\ \varrho_N(x')\ dx'\Big] = \mu_1, \qquad (3.33)$$

and in the left part ($-b_N \le x < -\ell_N$) one has

$$N\frac{x^2}{2} - N^2 \int_{-b_N}^{b_N} \log(|x'-x|)\ \varrho_N(x')\ dx' + \frac{N^2}{2}\Big[2\int_{x+\bar{\mathcal{D}}_x}^{b_N} \log(|x'-x|)\varrho_N(x')dx' + \int_{-b_N}^{x} \log\big(\bar{\mathcal{D}}_{x'}\big)\varrho_N(x')dx' + \int_{\ell_N}^{x+\bar{\mathcal{D}}_x} \log(\mathcal{D}_{x'})\varrho_N(x')dx'\Big] = \mu_2. \qquad (3.34)$$

One can write a similar equation on the right part, which has the same structure due to the inversion symmetry (about the origin) of the problem. The chemical potentials μ_1 and μ_2 ensure the two normalization constraints given in Eq. (A.2). Recall that D_x ($\bar{D}_x$), defined in Eq. (A.8), represents the distance from x over which one would find f fraction of particles on the left (right) side.

For f close to 1, most of the particles stay in the central region and consequently, the edge regions being lightly populated become much narrower than the central region. Hence, in this limit, the contribution from the third terms (inside the square brackets) on the L.H.S. of Eq. (3.33) and Eq. (3.34) are much smaller than the first and second terms. We neglect these terms and solve the resulting approximate SPEs which look like

$$\begin{aligned} N\frac{x^2}{2} - N^2 \int_{-b_N}^{b_N} \log(|x'-x|)\ \varrho_N(x')\ dx' &\approx \mu_1, \quad \text{for} \ \ |x| \le \ell_N \\ N\frac{x^2}{2} - N^2 \int_{-b_N}^{b_N} \log(|x'-x|)\ \varrho_N(x')\ dx' &\approx \mu_2, \quad \text{for}\ \ell_N < |x| \le b_N, \end{aligned} \qquad (3.35)$$

with the constraints $\int_{-\ell_N}^{\ell_N} \varrho_N(x)\ dx = 2f-1$ and $\int_{\ell_N<|x|\le b_N} \varrho_N(x)\ dx = 1-f$. Note that the saddle point problem in Eq. (3.35) is equivalent to the problem of computing the equilibrium density profile in an ATAC log-gas system, where $(2f-1)N$ number of particles are restricted to be inside $[-\ell_N, \ell_N]$ and the rest of the particles stay outside. For log-gas, this problem was solved in Ref. [39] subject to the constraint of having a fixed number of particles inside $[-\ell_N, \ell_N]$. The density profile is given by $\varrho_N(x) =$

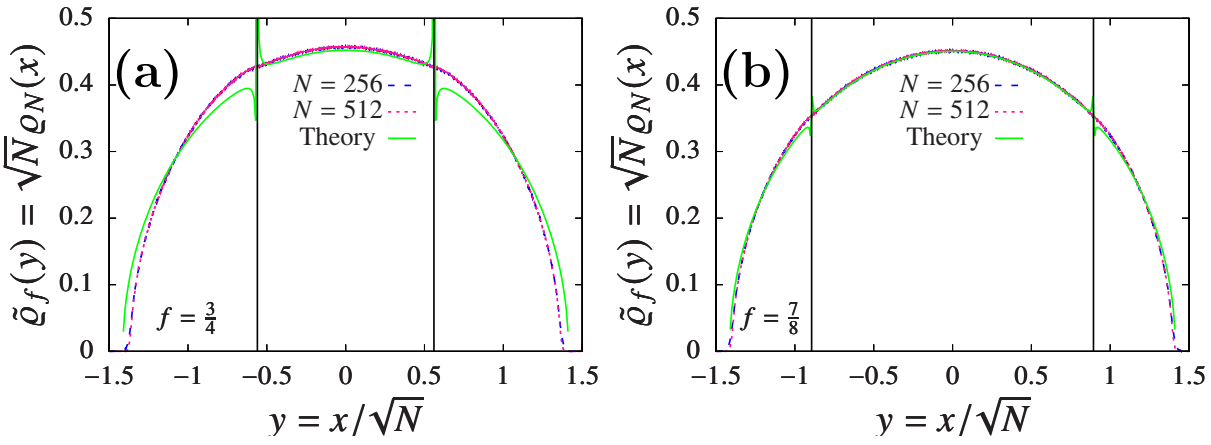

Figure 3.4: These plots show system size collapse of the numerical density profiles (dashed lines) for different N in the log-gas model for (a) $f = \frac{3}{4}$ and (b) $f = \frac{7}{8}$. The good collapse verifies the scaling $\varrho_N(x) = \frac{1}{\sqrt{N}}\tilde{\varrho}_f(x/\sqrt{N})$ in Eq. (3.11). The solid green line plots the scaling function $\tilde{\varrho}_f(y)$ as given in Eq. (3.14). We observe good agreement between simulation and theory in the central regime (represented by solid black vertical lines at $y = \pm\tilde{\ell}$). Outside this regime, the agreement between theory and simulation is better for f close to one and declines as f is reduced from one.

$(1/\sqrt{N})\tilde{\varrho}_f(x/\sqrt{N})$ with $\tilde{\varrho}_f(y)$ given explicitly in Eq. (3.14) with $\tilde{\ell} = \ell_N/\sqrt{N}$ and $\tilde{b} = b_N/\sqrt{N}$. We adopt this solution in our case however, ℓ_N is not known beforehand. We calculate its numerical value, $\ell_{\rm nu}$ using $\int_{-\ell_{\rm nu}}^{\ell_{\rm nu}} \varrho_{\rm nu}(x)dx = (2f-1)$, where $\varrho_{\rm nu}(x)$ being the numerically obtained density profile. The analytical form in Eq. (3.14) is compared with the numerically obtained densities in Fig. 3.4, where we notice good agreement between them. Closer the f is to one, better the agreement is.

3.4.2 Solution for f close to 0:

The SPEs for $0 < f < 1/2$ are different from the previous case and are derived in Eqs. (A.18 - A.20) for the three regimes, where one needs to insert $V(x) = -\log(|x|)$.

The SPE in the central part $-\ell_N \le x \le \ell_N$ is written explicitly as

$$\begin{aligned}\frac{Nx^2}{2} - \frac{N^2}{2}\Big[2\int_{x-\mathcal{D}_x}^{x+\bar{\mathcal{D}}_x} \log(|x'-x|) - \int_{x-\mathcal{D}_x}^{x} \log\big(\bar{\mathcal{D}}_{x'}\big) - \int_{x}^{x+\bar{\mathcal{D}}_x} \log(\mathcal{D}_{x'})\Big]\ \varrho_N(x')dx' \\ - \frac{N^2}{2}\int_{-b_N}^{-\ell_N} \Big[\log(|x'-x|) - \log\big(\bar{\mathcal{D}}_{x'}\big)\Big]\Theta(x'+\bar{\mathcal{D}}_{x'}-x)\ \varrho_N(x')\ dx' \qquad (3.36) \\ - \frac{N^2}{2}\int_{\ell_N}^{b_N} \Big[\log(|x'-x|) - \log(\mathcal{D}_{x'})\Big]\Theta(x-x'+\mathcal{D}_{x'})\ \varrho_N(x')\ dx' = \mu_1,\end{aligned}$$

where $\Theta(x)$ is the Heaviside step function.

We, here, solve this equation approximately for small f. Similar to the previous case (f close to 1), in this case also the central region $[-\ell_N, \ell_N]$ is much wider than the two edge regimes $[-b_N, -\ell_N)$ and $(\ell_N, b_N]$. Recall the central region contains $(1-2f)$ fraction of particles and the two edge regions contain f fractions of particles each. As f approaches to zero, the central region widens and the edge regions shrink. Starting from any point $x' \in [-b_N, -\ell_N)$ one must traverse to the image point $\bar{X}(x') = x' + \bar{\mathcal{D}}_{x'}$ on the right of x', to find f fraction of particles. For f close to 0, one does not require to move far inside the bulk. More precisely, the distance $\bar{\mathcal{D}}_{-\ell_N} = \big(\bar{X}(-\ell_N) + \ell_N\big)$ is very small for small f and $\bar{X}(x') < \bar{X}(-\ell_N)$ for any $x' \in [-b_N, -\ell_N)$. Additionally, the presence of $\Theta(x'+\bar{\mathcal{D}}_{x'}-x)$ on the second line of Eq. (3.36) makes the contribution from this integral non-zero only over a tiny region $-\ell_N \le x \le \bar{X}(-\ell_N)$. For x in this small region, we neglect the contribution from the integral on the second line of Eq. (3.36). Following similar arguments, the contribution from the integral on the third line of Eq. (3.36) is also ignored in the $f \to 0$ limit. As a justification, we later show that the resulting approximate solution for the density profile in the central part indeed matches quite well with the numerical results.

Neglecting the contributions from these integrals on the second and third lines of Eq. (3.36), the SPE in now approximately reads

$$\begin{aligned}\frac{Nx^2}{2} - N^2\int_{x-\mathcal{D}_x}^{x+\bar{\mathcal{D}}_x} \log(|x'-x|)\varrho_N(x')\ dx' \\ + \frac{N^2}{2}\int_{x-\mathcal{D}_x}^{x} \log\big(\bar{\mathcal{D}}_{x'}\big)\varrho_N(x')\ dx' + \frac{N^2}{2}\int_{x}^{x+\bar{\mathcal{D}}_x} \log(\mathcal{D}_{x'})\varrho_N(x')\ dx' \approx \mu_1. \qquad (3.37)\end{aligned}$$

For small f, $\mathcal{D}_x$ and $\bar{\mathcal{D}}_x$ can be approximated by $\frac{f}{\varrho_N(x)}$ which can be obtained from Eq. (A.8). After a few simple algebraic steps, one can calculate the contribution from the interaction part of the energy in the SPE. Apart from some numerical additive constants, which are independent of x, the contribution of the interaction term comes out to be of order $fN^2 \log[\varrho_N(x)]$. The SPE then becomes

$$\frac{Nx^2}{2} + fN^2 \log(\varrho_N(x)) \approx \mu_1. \tag{3.38}$$

Solving this equation one finds

$$\begin{aligned} &\varrho_N(x) \approx A_N \exp\left(-\frac{x^2}{2Nf}\right) \quad \text{for} \quad -\ell_N \leq x \leq \ell_N, \\ &\text{where} \quad A_N = \exp\left(\frac{\mu_1}{N^2 f}\right). \end{aligned} \tag{3.39}$$

This density profile should satisfy the normalisation $\int_{-\ell_N}^{\ell_N} \varrho_N(x)dx = 1-2f$ which provides a relation between μ_1 and ℓ_N for given f. It is easy to realize that in the $f \to 0$ limit, the support length $\ell_N \to \infty$. Using this fact, we find that $A_N \approx 1/\sqrt{2\pi Nf}$ *i.e.,* $\mu_1 \approx -(N^2 f/2)\log(2\pi Nf)$ in the leading order in f. Making use of this approximate expression of A_N back in the normalisation condition yields $\text{erf}(\ell_N/\sqrt{2Nf}) \approx 1 - 2f$, solving which one can find $\tilde{\ell} = \ell_N/\sqrt{N}$ in the leading order in f. Note that the density profile in the central regime $-\ell_N \leq x \leq \ell_N$ given in Eq. (3.39) has the scaling form $\varrho_N(x) = (1/\sqrt{N})\tilde{\varrho}_f(x/\sqrt{N})$ with $\tilde{\varrho}_f(y)$ given explicitly in Eq. (3.15). A comparison of this result with numerical simulation is provided in Fig. 3.5 for $f = 1/8$ and $f = 1/16$. The excellent agreement of theory with the numerical profiles in the central part provides justification of the approximations made to go from Eq. (3.36) to Eq. (3.37).

The density profile in Eq. (3.39) does not explain the behavior of the density of the remaining $2fN$ particles in the left and right edge parts. These regimes therefore need to be considered separately. We first focus on the left edge part. The SPE in the left edge

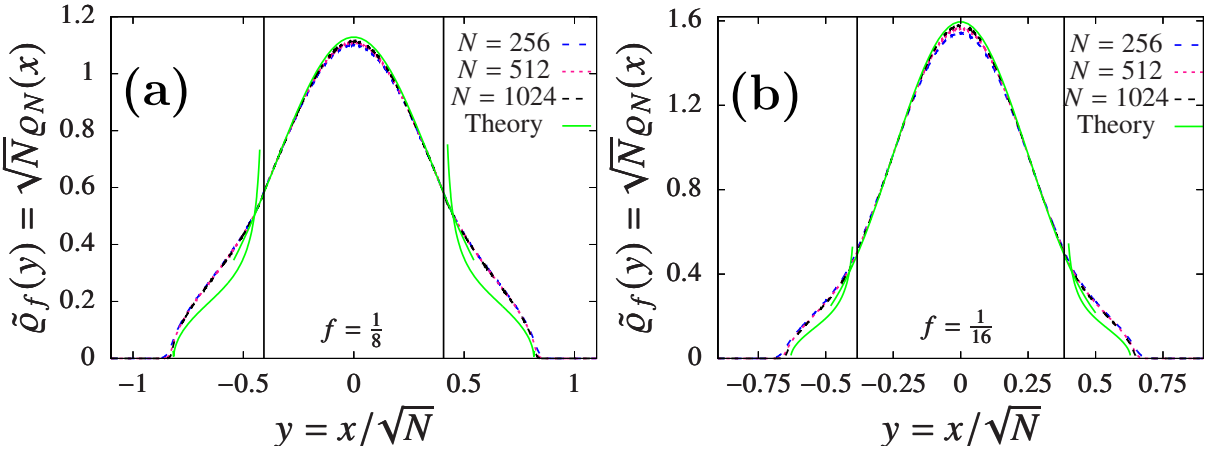

Figure 3.5: Comparison of numerically obtained (scaled) density profiles for different system sizes (dashed lines) with the analytical predictions (green solid lines) for log-gas (a) with $f = 1/8$ and (b) with $f = 1/16$. Once again collapse of numerical data for different N verifies the scaling in Eq. (3.11) with $\alpha = 1/2$. The theoretical prediction for the form of the scaled density profile $\tilde{\varrho}_f(y)$ inside the central part $(-\tilde{\ell}, \tilde{\ell})$ is Gaussian as in Eq. (3.15) [for log-gas]. The central region $(-\tilde{\ell}, \tilde{\ell})$ (represented by two vertical solid black lines) can be found from the relation $\int_{-\tilde{\ell}}^{\tilde{\ell}} \tilde{\varrho}_f(y)dy = 1 - 2f$. Outside the central region, the equilibrium density profile $\tilde{\varrho}_f(y)$ is different from the central part and its approximate analytical formula is provided in Eq. (3.16). Although agreement between the analytical formula [Eq. (3.16)] for the density and the numerical density profile reduces as f is increased from zero, however, it captures the total support of the density profile quite accurately.

part $(-b_N \leq x < -\ell_N)$ can be written from Eq. (A.18) with $V(x) = -\log(|x|)$ as

$$\frac{Nx^2}{2} - N^2 \int_{-b_N}^{-\ell_N} \log(|x' - x|)\ \varrho_N(x')\ dx' \ - \frac{N^2}{2}\left[2\int_{-\ell_N}^{x+\bar{\mathcal{D}}_x} \log(|x' - x|)\varrho_N(x')dx' \right. \quad (3.40)$$
$$\left. - \int_{-b_N}^{x} \log\left(\bar{\mathcal{D}}_{x'}\right)\varrho_N(x')dx' - \int_{-\ell_N}^{x+\bar{\mathcal{D}}_x} \log(\mathcal{D}_{x'})\varrho_N(x')dx'\right] = \mu_2.$$

It turns out that this SPE is in general difficult to solve for arbitrary $f \in (0, 1/2)$. We however notice that for small f, the contribution from the last three terms on the L.H.S. of Eq. (3.40) (*i.e.* the terms inside the square bracket) should be much smaller than the second term (in the first line).

As mentioned previously, the size $(b_N - \ell_N)$ of an edge part is very small for small f and consequently, for any $x \in [-b_N, -\ell_N)$ the image point $(x + \bar{\mathcal{D}}_x) \approx -\ell_N$. Hence, the integration ranges of the three terms inside the square bracket on the L.H.S. of

Eq. (3.40) are very small and one can neglect them compared to the first two terms. This approximation is exact for $x = -b_N$ and it becomes less valid as x is taken away from $-b_N$. Owing to the symmetry of the problem, one can make the same set of approximations for the SPE on the right edge part $\ell_N < x \leq b_N$. After making the above mentioned approximations, the SPEs on both edge parts now read

$$\begin{aligned} \frac{Nx^2}{2} - N^2 \int_{-b_N}^{-\ell_N} \log(|x'-x|)\ \varrho_N(x')\ dx' &\approx \mu_2, \quad \text{for} \quad -b_N \leq x < -\ell_N \\ \frac{Nx^2}{2} - N^2 \int_{\ell_N}^{b_N} \log(|x'-x|)\ \varrho_N(x')\ dx' &\approx \mu_2, \quad \text{for} \quad \ell_N < x \leq b_N. \end{aligned} \tag{3.41}$$

The problem in Eq. 3.41 can be interpreted as the problem of finding the density profile of the $2fN$ particles interacting all-to-all and conditioned to be outside the central range $[-\ell_N, \ell_N]$. This problem was studied in Ref. [39]. For this case, the scaled density profile $\tilde{\varrho}_f(y)$ takes the same form as in Eq.(3.14) with $\tilde{a} = 0$, since the central region $[-\ell_N, \ell_N]$ is empty, and thus is given by Eq.(3.16). The analytical form in Eq. (3.16) for the equilibrium density at the edges is compared with the density obtained numerically in Fig. 3.5. The support of the density $\tilde{b}$ can be computed from normalization and one finds $\tilde{b} = \sqrt{\tilde{\ell}^2 + 4f}$ which quite accurately describes the support of the simulation density profile in Fig. 3.5 even though the analytical form in Eq. (3.16) is only approximate. This happens because Eq. (3.41) is exact only when $|x| = b_N$ and the approximations for getting Eq. (3.41) starting from Eq. (3.40) does not hold for x away from the edges.

In summary, we found approximate forms of the equilibrium density profiles of the FR log-gas model for f close to 1 given by Eq. (3.14) and for small f given by Eqs. (3.15) and (3.16). These theoretical results are compared with simulation data in Fig. 3.4 and Fig. 3.5 respectively. We observe that the density profiles for large and small f are quite different. From Fig. 3.4, with f decreasing from one, the edge parts grow inside the central part as in the 1DOCP case discussed in the previous section. At $f = 1/2$ the central part vanishes. On the other hand, for small f, we observe from Fig.3.5(a) (for $f = 1/8$) and Fig.3.5(b) (for $f = 1/16$) that with decreasing f, the density profile in the central part grows, causing the edge parts to vanish at $f = 0$. At this value of f, the scaled density profile $\tilde{\varrho}_f(y)$ is described by Eq. (3.15) and reproduces the result obtained previously in Ref: [99].

<table>
<tr><th>Model / Features</th><th colspan="2">1DOCP ($k=-1$)</th><th colspan="2">log-gas ($k\to 0$)</th><th>other $k>-2$</th></tr>
<tr><td>Crossover</td><td colspan="2">Numerically demonstrated in Fig. 3.1(a)</td><td colspan="2">Numerically demonstrated in Fig. 3.1(b)</td><td>Numerically demonstrated in Fig. A.1</td></tr>
<tr><td rowspan="3">Free energy functional</td><td>Entropy</td><td>Subdominant*</td><td colspan="2">Subdominant</td><td rowspan="7">Only Numerical observation</td></tr>
<tr><td>Bulk energy</td><td>Dominant contribution</td><td colspan="2">Dominant contribution</td></tr>
<tr><td>Self energy</td><td>No contribution</td><td colspan="2">Neglected for fixed $f>0$</td></tr>
<tr><td>Saddle point equation</td><td colspan="2">Derived in Appendix. A.3</td><td colspan="2">Derived in Appendix. A.3</td></tr>
<tr><td rowspan="5">Scaling function $\tilde{\varrho}_f(y)$</td><td colspan="2">Exact analytical expression for $\tilde{\varrho}_f(y)$</td><td colspan="2">Approximate expression for $\tilde{\varrho}_f(y)$</td></tr>
<tr><td rowspan="2">$f\in\left[\frac{1}{2},1\right]$</td><td>Given in Eq. 3.12</td><td rowspan="2">f close to 1</td><td>Given in Eq. 3.14</td></tr>
<tr><td>Verified numerically in Fig. 3.2</td><td>Compared with numerics in Fig. 3.4</td></tr>
<tr><td rowspan="2">$f\in\left(0,\frac{1}{2}\right)$</td><td>Given in Eq. 3.13</td><td rowspan="2">f close to 0</td><td>Given in Eq. 3.15 & 3.16</td></tr>
<tr><td>Verified numerically in Fig. 3.3</td><td>Compared with numerics in Fig. 3.5</td></tr>
</table>

Table 3.1: A table summarising the status of our results. The * in the second row indicates the fact that for $0<f<1/2$ the entropy can contribute in the central part of the density profile in the 1DOCP model. However the central region $[-\ell_N,\ell_N]$ shrinks to a point in terms of scaled variable $y=x/N$ in the $N\to\infty$ limit since $\ell_N\sim\sqrt{\log N}$ [see Eq. (3.30)].

3.5 Summary and outlook

We studied equilibrium density profiles of two harmonically confined classical many-particle model systems – 1DOCP and log-gas, in which the particles are interacting via potentials $V(x)=-|x|$ and $V(x)=-\log(|x|)$, respectively. Additionally, the interaction is such that each particle, in both systems, can interact only up to d particles to its left and right if available. We numerically demonstrated that as the parameter $f=d/N$ is reduced from 1 to 0, the density profile in both models undergoes crossover from a finitely supported density profile to an infinitely extended Gaussian density profile. Furthermore, for both the models, we found that for all $f\in(0,1]$ the density profile possesses the same scaling with respect to the system's size N as in their respective

all-to-all coupling cases. To understand the above-mentioned crossover of the density profile, we derived the corresponding saddle point equations for both models. We found that the SPEs are different for $1/2 \leq f \leq 1$ and $0 < f < 1/2$. For the 1DOCP model, we solved the SPEs in all regimes of f and found exact analytical expressions for the density scaling functions which are verified with numerical computations. For the log-gas, we provided approximate solutions of the SPEs for large (close to 1) and small (close to 0) f. We have numerically found similar crossover in the density profiles to exist for other Riesz gas models corresponding to other values of k in Eq. (3.1). A brief discussion along with a numerical demonstration of such crossover for other values of k is provided in Appendix. A.5. We provided a table of summary in Tab. 3.1 which contains essential features of our results along with the equation numbers and the section numbers where they appear or they are derived.

Our work can be extended in several directions in the future. One immediate direction would be to find a complete solution of the SPEs for arbitrary f in the log-gas model as well as for other values of k in Eq. (3.1). It would be interesting to look at how the distribution of position of the particle at the edge gets affected as f is reduced from one. In the all-to-all coupled case it was found that the spacing distribution exhibits interesting statistical fluctuations for different k [98]. It would also be interesting to investigate how the spacing statistics get affected as f is reduced. Another interesting outlook would be to look at the crossover in densities due to temperature variation. Particularly for the all-to-all coupled log-gas ($f = 1$), Gauss-Wigner crossover is observed in Ref. [101] but how would such temperature-tuned crossover happen for $f < 1$? This is an interesting question to study. Extensions of our study to higher dimensional Riesz gas is another interesting and challenging problem [13, 131–133]. Exploring crossover in densities within quantum systems exhibiting power-law interactions could also be an intriguing avenue to investigate [134, 135]. It is important to emphasize that the parameter d in Eq. (3.1) does not really quantify the "range" of interaction. A more realistic model would be the Yukawa gas where the interaction gets screened on a finite length scale [125–129]. Extending our studies on density crossover and gap statistics, Riesz gas with Yukawa-type interaction would indeed be an interesting problem to explore in future.

After analyzing gap statistics in the all-to-all coupling Riesz gas and density crossovers

in the finite-ranged 1DOCP and log-gas systems under thermal equilibrium, we next investigate the Calogero-Moser model under non-equilibrium conditions by introducing activity into the system.

Chapter 4

Crystal to liquid cross-over in the active Calogero-Moser model

Active particles refer to a class of non-equilibrium systems where every individual unit breaks the detailed balance condition [136]. Powered by some mechanism, active particles exhibit stochastic but directed motion. A notable example is the run-and-tumble particle (RTP) which is used to describe the motion of certain species of bacteria like E. Coli [137]. Such a particle is often driven by an athermal noise with non-trivial correlations. As a result, analytical computation of their statistical properties is generally challenging. However, in the past few years, several striking properties have been uncovered for a single RTP in the form of position distributions in the free as well as confined space [138–140], first-passage properties [138,141], extreme value statistics [142], convex hull problem [143, 144] and so on. These studies have quantitatively established notable distinctions between the active motion and the passive Brownian motion [145, 146].

Going beyond single particle, studies on interacting active particles have also revealed fascinating behaviors like formation of fish schools [147, 148], flocking [149], jamming [150], absence of the equation of state for pressure [151] and motility-induced phase separation [152, 153], which are not seen for the thermal particles. Unlike, in the equilibrium case, where the stationary measure has Boltzmann form, there exists no universal principle to write the steady state for active particles. Recently, there is a growing interest in constructing microscopic lattice models and continuous space models that are amenable to analytical treatment, and which provide insights into the above mentioned

features. [109, 154–164]. Some recent works, for instance, looked at the active version of the Dyson's Brownian motion (DBM) [108, 109]. DBM is one of the well-studied models in statistical physics, which shares a direct connection with the random matrix theory [5, 6]. It has also found applications in other areas such as quantum chaos [5] and growth model [165]. In DBM, the underlying particles interact via pairwise repulsive logarithmic potential and are additionally subjected to a global harmonic trap. Due to the confining trap, the system attains equilibrium at late times, and in the large N limit (with N being the particle number), the average density profile takes the famous Wigner semi-circle (WSc) form [32]. The active version of this model was studied in Refs. [108, 109]. Surprisingly, across a broad range of the activity parameter, it was numerically found that the density profile in the steady state still maintains the shape of the WSc [108]. In support of this, some analytical arguments were given based on the computations of the covariance of the particle positions [109].

The Calogero-Moser (CM) model is another classic example of a solvable many-particle system where particles interact via repulsive inverse-square law potential as opposed to the logarithmic interaction in the DBM [60, 61, 65, 66]. It has also found connections with the random matrix theory and soliton physics [67, 68, 72]. As mentioned earlier, although the interaction potentials of the CM model and DBM model are very different, it turns out that they share an identical minimum energy configuration. The equilibrium positions of particles for both models coincide with the zeros of the Hermite polynomials in the zero noise limit [31]. Consequently, the average equilibrium density profiles for the two cases are exactly the same, and they converge to the WSc form in the large N limit. However, the fate of this connection in the presence of activity is not known. In the present work, we systematically explore the connections between the two models when the particles are driven by the active noise instead of the thermal noise.

In particular, we investigate the following steady-state properties of the active Calogero-Moser model: (i) the mean density profile and, (ii) fluctuations and correlations of particle positions. For part (i), we numerically demonstrate that as the system's activity increases, the density profile undergoes a crossover from a multi-peaked crystalline structure at low activity, to a liquid-like state exhibiting a smooth Wigner semi-circular density profile at

the intermediate activity. As the activity increases further, the profile changes from the Wigner semi-circle to a bell-shaped form. For part (ii), we follow the approach developed in Ref. [109] and compute the covariance of particle positions and of the gaps in the limit of small activity and large persistence time, providing support for the observed transition in the density profile. Additionally, we point out notable differences between the active CM and active DBM models in both the steady-state density profile and the variance of particle positions.

The remainder of the chapter is structured as follows: Sec. 4.1 is devoted to the description of the model and summarising the main results. We present numerical results on the steady-state density profile including its crossover and system size scaling in Sec. 4.2. Sec. 4.3 looks at the fluctuation and covariance of particle positions, which is followed by the conclusion and future directions in Sec. 4.4.

4.1 Model, observables and the summary of our findings

We consider the motion of N run-and-tumble particles in one dimension, interacting with each other via repulsive inverse-square power-law interaction with strength g (> 0). In addition, the particles are subjected to a global confining harmonic potential with stiffness parameter ω (> 0). Denoting the position of the i-th particle at time τ by $X_i(\tau)$, the time evolution equation is given by

$$\frac{dX_i}{d\tau} = -\omega X_i + \sum_{\substack{j=1 \\ j\neq i}}^{N} \frac{2g}{(X_i - X_j)^3} + V_0\sigma_i(\tau), \quad \text{for } i = 1, 2, ..N, \tag{4.1}$$

where V_0 is the speed of the particle and $\sigma_i(\tau)$ is the dichotomous noise that switches between ± 1 at a constant rate Γ. Because of the infinite repulsion on contact, the particles remain ordered, $X_1 < X_2 < ... < X_N$. For any pair of particles, the noises $\sigma_i(\tau)$ on different particles are statistically independent and their temporal correlation takes the form $\langle \sigma_i(\tau)\sigma_j(\tau')\rangle = \delta_{ij} \exp\left(-2\Gamma|\tau - \tau'|\right)$ with δ_{ij} being the Kronecker delta. Note that for $\Gamma \to \infty$, $V_0 \to \infty$ with the ratio V_0^2/Γ fixed, the model reduces to the passive

limit of Brownian particles with diffusion coefficient equal to $V_0^2/2\Gamma$. However, for any other values of these parameters, we anticipate to see departures from the thermal case. It is instructive to write the equations in dimensionless form. Defining the dimensionless time and position variables $t = \omega\tau$ and $x_i = X_i/(g/\omega)^{1/4}$, the above equations take the form:

$$\frac{dx_i}{dt} = -x_i + \sum_{\substack{j=1 \\ j\neq i}}^{N} \frac{2}{(x_i - x_j)^3} + v_0\sigma_i(t), \quad \text{for } i = 1, 2, ..N, \tag{4.2}$$

where now the only remaining dimensionless parameters are $v_0 = \frac{V_0}{\omega^{3/4}g^{1/4}}$ and the tumbling rate $\gamma = \Gamma/\omega$. Note that, the activity in the system can be increased either by enhancing the speed v_0 or reducing the tumbling rate γ, although the two parameters have quantitatively different effects.

In this work, we will be interested in steady-state properties. In particular, we consider the density of particles defined as follows:

$$\rho_{\rm st}(x) = \frac{1}{N}\sum_{i=1}^{N}\langle\delta(x_i - x)\rangle_{\rm st}, \tag{4.3}$$

where $\langle ...\rangle_{\rm st}$ denotes an average over the steady-state distribution.

In our simulations, we observe that increasing the activity in the system causes the density profile to cross over from a multi-peaked crystalline structure to a smooth Wigner semicircle, and eventually to a bell-shaped profile. To characterize the first crossover from a crystal-like structure to a liquid-like structure, we examine the fluctuations of particle positions in the steady state. Therefore, we measure the mean positions, the variances, and the mean interparticle separations as follows:

$$\bar{x}_i = \langle x_i\rangle_{\rm st}, \tag{4.4}$$

$$s_i^2 = \langle(x_i - \bar{x}_i)^2\rangle_{\rm st} \tag{4.5}$$

$$\Delta_{i,n} = \bar{x}_{i+n} - \bar{x}_i. \tag{4.6}$$

Additionally, we compute the covariance of the particle positions which finally leads to

the computation of the variance of inter-particle gaps

$$g_{i,n}^2 = \langle (x_{i+n} - x_i)^2 \rangle_{\rm st} - \Delta_{i,n}^2. \tag{4.7}$$

Specifically, to study the crossover more quantitatively, we compare the standard deviation of particle positions to the average interparticle separation, known as the Lindemann's ratio [166],

$$\eta_i = \frac{s_i}{\Delta_{i,1}}. \tag{4.8}$$

To address the second transition, from a smooth Wigner semi-circle to a bell-shaped profile, we quantify the difference between the steady-state density profile and the Wigner semi-circle $\rho_{\rm sc}(x)$ by computing the following quantity:

$$\chi = \int_{-\infty}^{\infty} |\rho_{\rm st}(x) - \rho_{\rm sc}(x)| dx, \tag{4.9}$$

where

$$\rho_{\rm sc}(x) = \begin{cases} \frac{1}{\pi N}\sqrt{2N - x^2} \text{ for } |x| \leq \sqrt{2N} \\ 0 \qquad\qquad \text{otherwise.} \end{cases} \tag{4.10}$$

In the following sections, we will numerically study the form of $\rho_{\rm st}(x)$, the position fluctuations $\{s_i\}$, Lindemann's ratio $\{\eta_i\}$, the quantity χ and the variance of inter-particle gap $g_{i,n}^2$ upon varying (i) the activity parameters v_0 and γ and (ii) the number of particles N.

Before going into the detailed discussion, it is useful to summarize our main results:

1. As observed in the active Dyson's Brownian motion, the steady-state density profile in the active Calogero-Moser model also exhibits three distinct structures depending on the strength of the activity. At very small activity, the system resembles a 'crystal' having a multi-peaked density profile. The Wigner semi-circle gives the envelope of the density profile (see Fig. 4.2(a)). As activity increases, the crystalline structure in the density profile vanishes, resulting in a smoother profile resembling a 'liquid'. This profile matches well with the Wigner semi-circle across nearly the entire support region, except at the edges (see Fig. 4.2(b)). The support of the

density profile can be approximated as $[-\sqrt{2N}, \sqrt{2N}]$. By increasing the activity further, the steady-state density profile deviates significantly from the Wigner semi-circle, transforming into a bell-shaped profile with support approximately on $[-v_0, v_0]$ where $v_0 \sim \mathcal{O}(N)$ (see Figs. 4.2(c) and 4.3). Interestingly, we observe that near the edges, the density profile decays following a power-law of the form $\sim 1/x^3$ (see Fig. 4.3). This power-law decay seems to be universal as long as the particles confined in a harmonic trap experience infinite repulsion upon contact.

2. These three distinct structures in the density profile correspond to three different activity regimes, referred to as the weakly active, intermediate, and strongly active regimes. A density profile with noticeable peaks defines the weakly active regime. The intermediate active regime corresponds to a smooth Wigner semi-circle density profile, while the bell-shaped density profile is indicative of the strongly active regime. These regimes are further quantified by the computation of the Lindemann's ratio η_i (defined in Eq. (4.8)) and the quantity χ (defined in Eq. (4.9)). Based on the numerical values of these two quantities $\eta_{N/2}$ and χ, we draw a 'phase' diagram in Fig. 4.8 showing three activity regimes for two different system sizes.

3. We use an analytic approach developed in Ref. [109] based on small oscillations about the ground state (i.e., in the limit $v_0 \to 0$) to describe the transition from the weakly active to the intermediate active region. Surprisingly, this small oscillation theory accurately predicts the variance of particle positions and gaps in both the weakly active and intermediate active regions. For large N, we derive a closed expression for the variance of particle positions in the small tumbling rate limit, as presented in Eq. (4.33). By comparing the typical fluctuations in particle positions with the existing length scales in the system, we identify the criteria for the transitions. The first transition from the weakly active to the intermediate active region occurs when $v_0 \sim \mathcal{O}(1)$, independent of system size. On the other hand, the second transition, from the intermediate active to the strongly active region, is expected to occur at $v_0 \sim \mathcal{O}(N)$. Additionally, from the covariance of particle positions, we have computed the variance of the gap between any two particles. In the large N limit, we derive an analytical formula for the variance of the interparticle gap $g_{i,n}^2$

in Eq. (4.45) near the center of the trap ($i = N/2$). An extension to finite γ, based on a future work [167], is also presented.

4.2 Density profile

In this section, we discuss the effect of activity on the average density profile in the steady state. To get the density profile, we first evolve the system for a very long time following Eq. (4.2). After that, the density profile is obtained simply as the histogram of the positions and then averaged over many similar realizations. For $v_0 = 0$, the density takes the Wigner semi-circular form for large N [75]. As mentioned in the previous section, the system's activity can be tuned by varying both the speed v_0 and the tumbling rate γ. Initially, we adjust the system's activity by varying the parameter $a \in (0, 1]$ where, a is defined as $v_0 = aN$, while keeping γ fixed at unity. Later, we will also present results due to the variation of the tumbling rate γ. Here, we will demonstrate that even for the active CM model, the density converges to the Wigner semi-circle in a significant parameter regime. To present density profiles across various system sizes effectively, we find it useful to show the scaled density profile $\tilde{\rho}(z)$, defined by

$$\tilde{\rho}(z) = \sqrt{N}\rho_{\rm st}(\sqrt{N}z), \tag{4.11}$$

where both $\tilde{\rho}$ and z are of order $\mathcal{O}(1)$. For further discussion, it is useful to identify three parameter regimes depending on the value of v_0.

4.2.1 Weakly active

At zero activity ($v_0 = 0$), the equilibrium configuration $\{x_i^{(\rm eq)}\}$ is obtained by equating $dx_i/dt = 0$ in Eq. (4.2) and solving the resulting equations. This implies that the equilibrium configuration $\{x_i^{(\rm eq)}\}$ corresponds to the zeros of Hermite polynomials [75]. For small v_0, particles fluctuate little about their equilibrium positions. This is also illustrated in Figure 4.1(a) where we observe sharp peaks in the density about the equilibrium positions. For instance, with just two particles ($N = 2$), the peaks are located (in the unscaled variable) around $x = \pm 0.71$ which are the zeros of the Hermite polynomials of

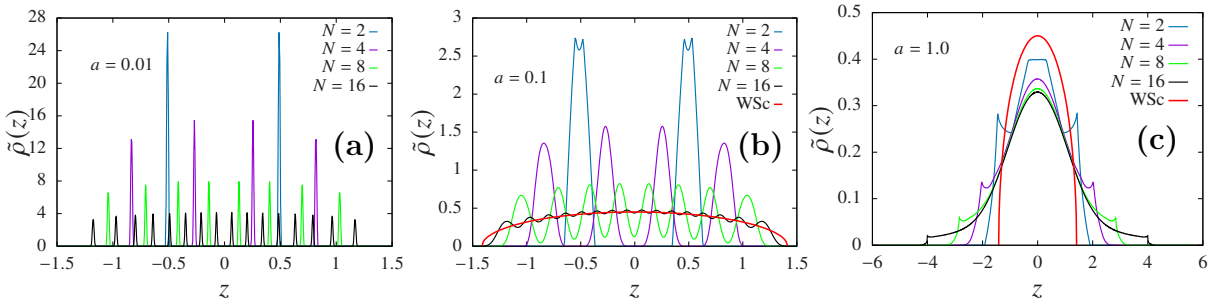

Figure 4.1: The total (scaled) density profiles $\tilde{\rho}(z)$ for different (small) system sizes with several values of the activity, $a = 0.01$ in (a), 0.1 in (b) and 1.0 in (c) show the crossover: from sharply peaked density profile in (a) at very small activity to bell-shaped density profile in (c) at very large activity via an intermediary WSc profile in (b). For all the panels, the flipping rate γ is kept fixed at 1.

degree 2. Similarly, for $N = 4$ the locations of the peaks are at $x = \pm 1.65$ and $x = \pm 0.52$ which again are zeros of the Hermite polynomial of degree 4. As long as the width of these peaks remains much smaller than the inter-particle separation, we refer to the system as being in the weakly active regime. In this regime, the entire system resembles a crystal where particles are ordered around their equilibrium positions, as illustrated in Fig. 4.1(a). Therefore, the coarse-grained density, in this regime is governed by the Wigner semi-circle in the large-N limit, supported over $[-\sqrt{2N}, \sqrt{2N}]$ (see Fig. 4.2(a)). Detailed information about the numerical simulations can be found in Appendix A.1.

4.2.2 Intermediate activity:

As the activity increases, particle fluctuations around their equilibrium positions grow, becoming comparable to the distance to their nearest neighbors. Consequently, the density profile becomes smoother. For example, see Fig. 4.1(b), where in a system with $N = 16$ particles, the peaks in the steady-state density profile almost vanish, creating a density profile that aligns well with the Wigner semi-circle form. In Fig. 4.2(b), for the activity parameter $a = 0.1$, the steady-state density profiles for two different (large but finite) system sizes match extremely well with the Wigner semi-circular form, apart from the edges. We refer to this as the intermediate active region, where the steady-state density profile loses the peaks, at least in the bulk, and conforms well to the Wigner semi-circular form. Thus, as observed in the case of active DBM [108], the density profiles

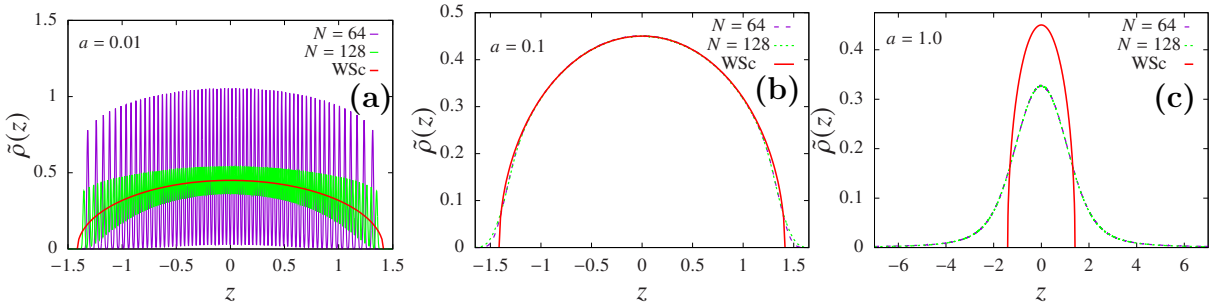

Figure 4.2: The transition in the (scaled) density profile $\tilde{\rho}(z)$ is shown once again with the same set of parameters as in Fig. 4.1, but now for large system sizes. In (a), where the activity parameter $a = 0.01$, the peaks in the density profile smooth out with increasing system sizes, and the numerically obtained density profile approaches the WSc density profile. In the middle panel (b) with an activity parameter of $a = 0.1$, the density profile in the bulk approximately matches the WSc form but deviates at the edges. The deviation from the WSc profile increases with system size. The form as well as the support of the density profile has changed significantly in (c) with $a = 1.0$. The density forms a bell-shaped profile extending approximately to $[-aN, aN]$ (depicted separately in Fig. 4.3). However, it is important to note that the $\sqrt{N}$ scaling in the density profile remains consistent throughout the bulk.

in the active CM model also maintain their Wigner semi-circular form in the bulk even at significantly high levels of activity. Notice that near the edges, the density profiles exhibit slight deviations from the Wigner semi-circular form. However, it is important to observe that there are no 'wings', a clear distinction from the active DBM as discussed in Refs. [108, 109]. This is probably related to the distinctive behaviors of the edge particles compared to those in the bulk of the active DBM [109] (see Sec.4.3.2 near Eq. (4.35)). It is due to the fact that the (active) CM model is much more rigid than the (active) log gas [75].

4.2.3 Strongly active

When v_0 becomes substantially large, particles in the edge can move significantly more in the harmonic trap compared to the passive case. Under this circumstance, the density deviates notably from the semi-circular form, they now have a bell-shaped appearance (see Fig. 4.1(c) and 4.2(c)). Remarkably, as the density profile transitions from the Wigner semi-circle to a bell-shaped distribution, the scaling behavior with system size as in Eq. (4.11) persists. The bulk of the density is thus still contained over an interval of

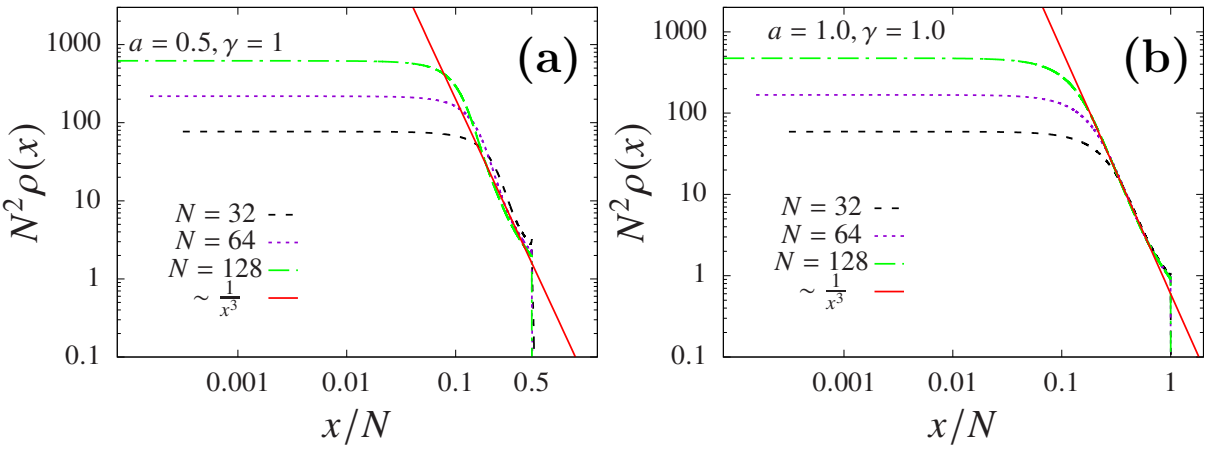

Figure 4.3: Showing the total support of the density profile $\rho(x)$ approximates to $[-aN, aN]$ in the large activity limit. The steady-state density profiles are drawn as a function of x/N for three different system sizes which seem to converge and show a sharp drop at $x = aN$. Near the edges, the density profiles (dashed lines) decay as $\sim 1/x^3$ (red solid line).

size $\sim \sqrt{N}$. However, the total support of the density profile undergoes an approximate shift to $[-aN, aN]$, contrasting with the previous support of $[-\sqrt{2N}, \sqrt{2N}]$ (see Fig.4.3). Additionally, near the edges, the density profile exhibits a power-law decay characterized by $\sim 1/x^3$ (see Fig.4.3). The $1/x^3$ power-law decay is not limited to the active CM model; it has been observed in various other systems. For instance, it manifests in active DBM under extreme activity conditions ($v_0 \sim \mathcal{O}(N)$), as documented in Ref. [108]. Moreover, it emerges in models featuring contact interaction i.e., where the interaction strength tends towards zero ($g \to 0^+$), even at modest activity levels ($v_0 \sim \mathcal{O}(1)$) [108]. This decay seems to be universal, independent of the specific interaction potential, provided it involves infinite repulsion upon contact. Nevertheless, our current understanding of this decay lacks theoretical insights.

Recall that the system's activity can also be enhanced by reducing the flip rate γ. In Fig. 4.4, we demonstrate a crossover in a system of 64 particles, this time with changing the γ keeping the speed v_0 fixed at 1.6 ($a = 0.025$). As γ is reduced, the density profile transitions from having noticeable peaks to a smooth Wigner semi-circle density profile, at least near the center of the trap. With such a small v_0, the strongly active regime cannot be achieved solely by reducing γ as demonstrated in the phase diagram (Fig.4.8). Thus, the system's activity is mainly controlled by v_0 rather than γ.

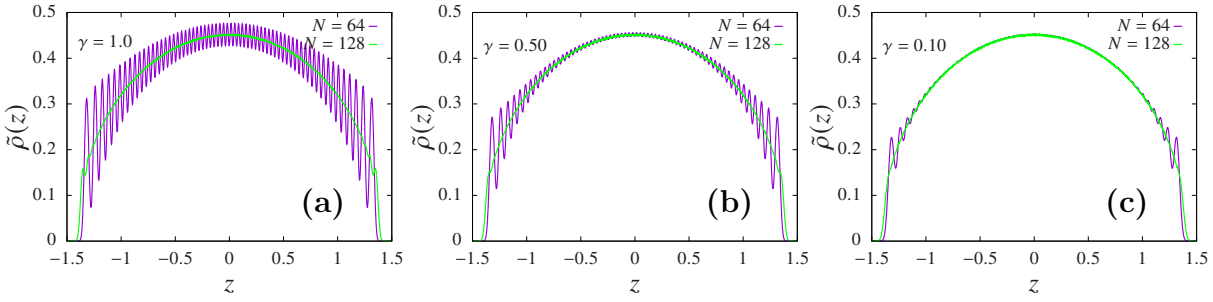

Figure 4.4: Showing the crossover from a 'crystal' to 'liquid' in a system of 64 particles because of reducing the flip rate γ keeping the activity parameter a fixed at 0.025. For the system size $N = 128$ with $a = 0.025$, the system has already crossed over to the liquid state characterized by a smooth density profile.

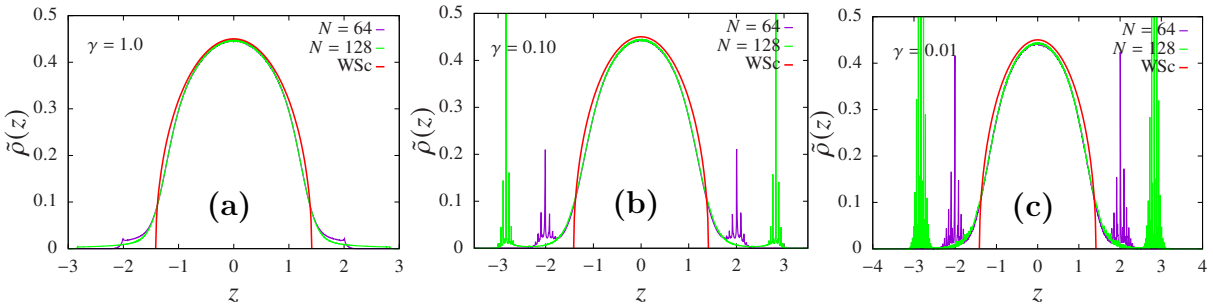

Figure 4.5: Demonstration of the emergence of wing-like structures in the density profile within the strongly active region ($a = 0.25$) as a result of the reduced flipping rate, γ.

In the strongly active region, where the density profile deviates significantly from the Wigner semi-circle and attains a bell-shaped profile, it has a sharp cut-off at $\pm v_0$ when γ remains sufficiently large (see Fig. 4.3). For smaller γ, two slightly broadened peaks appear near the edges ($\pm v_0$), creating a wing-like structure as shown in Fig. 4.5. The position of the 'wings' can be roughly obtained by balancing, for the edge particles, the driving velocity term with $\sigma_i = +1$ and the harmonic term, leading to $x_i \sim v_0 \sim N$ (while in the intermediate regime of the active DBM, the position of the 'wings' is $\sim \sqrt{N}$). Note that these 'wings' are only observed when γ is small enough ($\gamma \lesssim 0.1$), since it requires that the particles spend a lot of time near the fixed points for which $\sigma_i = +1$ for the edge particles.

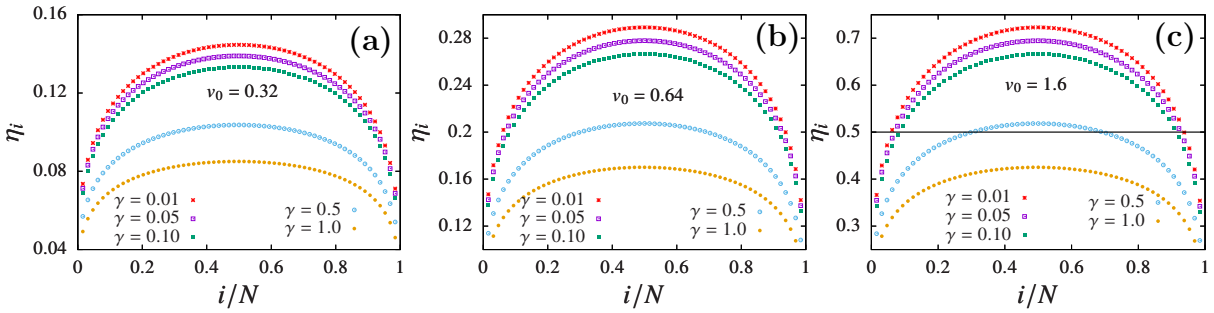

Figure 4.6: Numerically computed Lindemann's ratio η_i (points) as a function of i/N for different values of the flipping rate γ within a system comprising $N = 64$ particles. Three panels correspond to three different values of the speed v_0, $0.32, 0.64$ and 1.6 in (a),(b) and (c) respectively. Additionally, we have drawn a solid black (horizontal) line at 0.5 indicating the cases where the standard deviation of particle positions becomes exactly equal to 50% of the average distance to the nearest neighbor. For a quantitative distinction between the 'crystal' and 'liquid' phases, we use this as a reference line above which we consider the system to be in the 'liquid' phase and below which is in the 'crystal' phase. In the first two panels, the system remains in the 'crystal' phase regardless of the γ values analyzed. However, in the third panel with speed $v_0 = 1.6$, the system stays in the 'crystal' phase for higher values of γ ($\gamma \gtrsim 1$). Conversely, for smaller γ values ($\lesssim 0.5$), the Lindemann's ratio exceeds 0.5 at the center, indicating a 'liquid' phase.

4.2.4 Discussion of crossovers

Thus, based on values of the parameters v_0 and γ, the steady-state density profile has three different forms. When the activity is extremely low, the particles stay close to their equilibrium positions and fluctuate within a small region. This leads to a density profile with sharp peaks, resembling a crystal phase. As the activity increases, particle fluctuations around their equilibrium positions grow, becoming comparable to the distance to their nearest neighbors. The density profile then becomes smoother, resembling a liquid phase. To quantify this transition further, we numerically compute the Lindemann's ratio defined in Eq. (4.8). This ratio compares the standard deviation of a particle's position to the average gap between the particle and its nearest neighbor. The numerical values of this ratio are shown in Fig. 4.6 for different values of the activity parameter v_0 and the flipping rate γ in a system with a total 64 particles. Notably, we introduce a reference line at 0.50, representing scenarios where particle fluctuations are exactly 50% of the average gap. When Lindemann's ratio at the center exceeds this reference value, we consider the system to be in a 'liquid' phase; when it is below, it is in a 'crystal' phase. It's evident

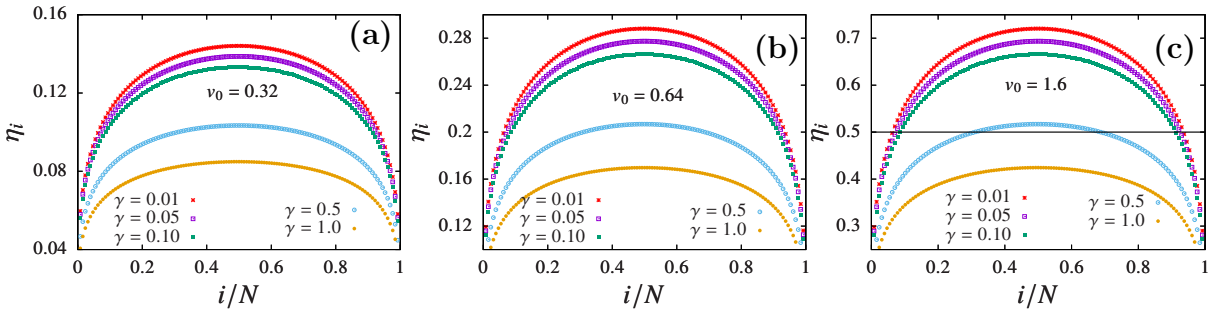

Figure 4.7: Lindemann's ratio η_i as a function of i/N for different values of the flipping rate γ is shown in Fig. 4.6, now within a system comprising $N = 128$ particles. Similar to the scenario of $N = 64$ in this case, the system remains in the 'crystal' phase for $v_0 = 0.32$ and 0.64 across all values of γ and shifts to the 'liquid' phase for $v_0 = 1.6$ when $\gamma \lesssim 0.5$.

that a system comprising 64 particles with speed $v_0 = 0.32$ and 0.64 consistently remains within the 'crystal' phase, as illustrated in Fig. 4.6(a) and (b). Conversely, for $v_0 = 1.6$, the system resides in the 'crystal' phase only when the flip rate $\gamma \gtrsim 0.5$; below this value, it is in the 'liquid' phase. The corresponding scenarios are illustrated in Fig. 4.7 for a system comprising of 128 particles. From Figs. 4.6 and 4.7, it is now clear that the 'crystal' to 'liquid' transition occurs at $v_0 \sim \mathcal{O}(1)$, independent of system size.

For the second crossover, from a smooth Wigner semi-circular density profile to a bell-shaped density profile, we numerically compute the values of the quantity χ as defined in Eq. (4.9) across various combinations of parameters a and γ. Table 4.1 presents the χ values for two distinct system sizes, $N = 64$ and 128. Whenever the value of χ exceeds 0.1, we call the system to be in the strongly active regime. Based on the values of Lindemann's ratio and the quantity χ we draw a 'phase' diagram in the a, $1/\gamma$ plane in Fig. 4.8 separating three distinct 'phases' which correspond to weakly active, intermediate and strongly active regions.

In summary, we numerically compute the steady-state density profile in three activity regimes: weakly active, intermediate active and strongly active regime. In these regimes, the density profile exhibits distinct characteristics: in the weakly active regime, it features sharp peaks akin to a 'crystal' phase, which vanish (at least in the bulk) in the intermediate active region, resembling a transition to a 'liquid' phase. In the strongly active region, the density profile takes on a bell-shaped form. To distinguish these three regions more quantitatively, we look at the Lindemann's ratio η_i (defined in Eq. (4.8))

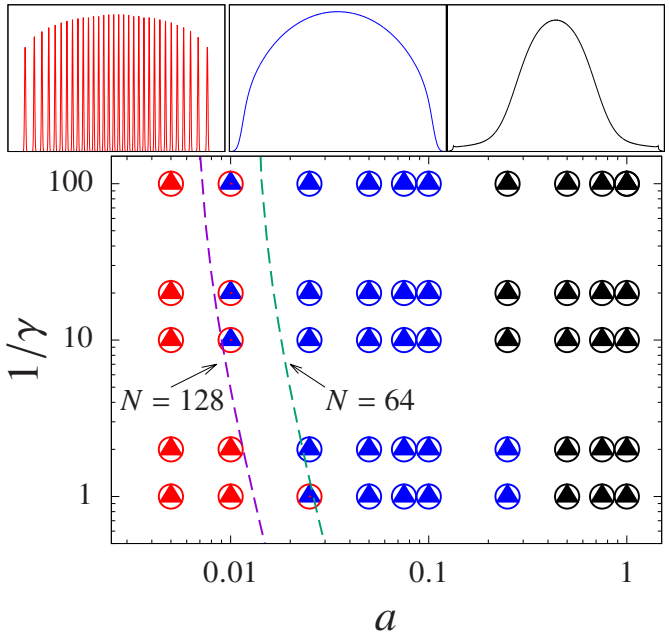

Figure 4.8: Lower diagram depicts three distinct 'phases' in the active CM model within the parameter space represented by a and $1/\gamma$, with red, blue, and black points representing weakly active, intermediate and strongly active regimes respectively. Red points signify scenarios where Lindemann's ratio η_i at the center of the trap ($i = N/2$) is less than 0.5 (see Fig. 4.7). Blue points represent intermediate active regions where the Lindemann's ratio at the trap center exceeds 0.5, but the values of χ defined in Eq. (4.9) remain below 0.1 (see Table. 4.1). The strongly active regime (indicated by black points) corresponds to cases where the value of χ exceeds 0.1. Density profiles in the corresponding regimes are shown schematically in the top panels. Two different system sizes are represented: circles (○) correspond to $N = 64$, while triangles (▲) represent $N = 128$. Notice that the second transition (from blue to black) occurs at $a \sim \mathcal{O}(1)$, which is independent of N. In contrast, the first transition (from red to blue) occurs at a values that depend on N, as depicted by two schematic (dashed) lines for the different system sizes.

and the quantity χ (defined in Eq. (4.9)). Based on their numerical values, we made a 'phase' diagram in the a, $1/\gamma$ plane. Next, we discuss our theoretical understanding of the fluctuations in particle positions using Hessian calculations. By examining the Hessian matrix of the CM system [75, 168], analytical results have been obtained by our collaborators L. Touzo, P. L. Doussal, and G. Schehr from the University of Paris City and the Sorbonne University, respectively.

Flip rate, γ	Activity parameter a	χ for $N = 64$	χ for $N = 128$
1.000	0.100	0.014	0.018
1.000	0.250	0.084	0.084
1.000	0.500	0.230	0.229
0.500	0.100	0.017	0.021
0.500	0.250	0.099	0.096
0.500	0.500	0.266	0.264
0.100	0.100	0.022	0.027
0.100	0.250	0.122	0.117
0.100	0.500	0.325	0.322
0.050	0.100	0.023	0.028
0.050	0.250	0.126	0.120
0.050	0.500	0.337	0.332
0.010	0.100	0.024	0.029
0.010	0.250	0.130	0.125
0.010	0.500	0.351	0.344

Table 4.1: Table showing the values of χ (defined in Eq. (4.9), which measures the deviation of the steady-state density profile from the Wigner semi-circle profile, for system sizes $N = 64$ and 128. The table includes results for various combinations of the tumbling rate γ and the activity parameter a $(= v_0/N)$. By applying a cutoff of $\chi = 0.1$ to distinguish the transition from the intermediate activity region to the strongly active region, we observe that this transition is independent of system size.

4.3 Variance and covariance of the particle displacements

In this section, we compute the correlation between the displacements of different particles in the small noise limit ($v_0 \to 0$). To this end, we will utilize the Hessian-based technique developed in Ref. [109]. A striking feature about the model in Eq. (4.2) is that for $v_0 = 0$, the positions of the particles $\mathbf{x}^{(\mathrm{eq})} = (x_1^{(\mathrm{eq})}, x_2^{(\mathrm{eq})}, ..., x_N^{(\mathrm{eq})})$ are given by the zeroes of the Hermite polynomial of degree N, *i.e.,* $H_N\left(x_i^{(\mathrm{eq})}\right) = 0$. Moreover, for $N \to \infty$, the equilibrium particle density converges to the Wigner semi-circle which has a finite support on $[-x_e, x_e]$ where $x_e = \sqrt{2N}$. For small v_0, we anticipate the position x_i of the i-th particle to deviate very little from its equilibrium value $x_i^{(\mathrm{eq})}$. Let us denote this displacement by δx_i and write

$$x_i = x_i^{(\mathrm{eq})} + \delta x_i. \tag{4.12}$$

Assuming that the typical fluctuations of the particle positions δx_i are small compared to the typical size of the gaps $x_{i+1}^{(\mathrm{eq})} - x_i^{(\mathrm{eq})} \sim 1/\sqrt{N}$, one can linearise the equation of motion in (4.2) in δx_i to obtain

$$\frac{d\left(\delta \mathbf{x}\right)}{dt} \simeq -\mathbf{H}_{\mathrm{CM}} \delta \mathbf{x} + v_0 \boldsymbol{\sigma}, \tag{4.13}$$

with $\delta \mathbf{x} = (\delta x_1, \delta x_2, ..., \delta x_N)^T$ and $\boldsymbol{\sigma} = (\sigma_1(t), \sigma_2(t), .., \sigma_N(t))^T$. Moreover, $\mathbf{H}_{\mathrm{CM}}$ denotes the Hessian matrix for the Calogero-Moser model and is given completely in terms of the zeroes of the Hermite polynomial as [75]:

$$\left(\mathbf{H}_{\mathrm{CM}}\right)_{ij} = \delta_{i,j} \left[1 + \sum_{\substack{n=1 \\ n \neq i}}^{N} \frac{6}{\left(x_i^{(\mathrm{eq})} - x_n^{(\mathrm{eq})} \right)^4} \right] - \frac{6\left(1 - \delta_{i,j}\right)}{\left(x_i^{(\mathrm{eq})} - x_j^{(\mathrm{eq})} \right)^4}. \tag{4.14}$$

$$\tag{4.15}$$

Although we have linearized the equation of motion, solving Eq. (4.13) analytically still turns out to be difficult due to the dynamics of the σ variables. Therefore, in order to simplify the dynamics further, we will focus on the $\gamma \to 0^+$ limit, which implies that the σ variables remain fixed to their initial values throughout the time evolution. However, these initial values still fluctuate for different realizations. Now, for a given realization of $\boldsymbol{\sigma}$, we anticipate our system to go to a unique fixed point at large times. For the case of the active Dyson's Brownian motion, this was seen in Ref. [109] using extensive numerical simulations. Anticipating this to be true for the active Calogero-Moser model also, we can then write the steady-state displacements from Eq. (4.13) as

$$\delta \mathbf{x} \simeq v_0 \ \mathbf{H}_{\mathrm{CM}}^{-1} \ \boldsymbol{\sigma}. \tag{4.16}$$

We now use this solution to calculate the variance and covariance of the displacement variables. To do this, we first recall that σ_i is chosen from ± 1 with equal probability independent of the index i. Hence, we obtain $\langle \sigma_i \rangle = 0$ and $\langle \sigma_i \sigma_j \rangle = \delta_{i,j}$. This allows us

to write the expressions of the mean and the covariance as

$$\langle \delta x_i \rangle_{\rm st} \simeq 0 \tag{4.17}$$

$$\langle \delta x_i \delta x_j \rangle_{\rm st} \simeq v_0^2 \left(\mathbf{H}_{\rm CM}^{-2} \right)_{ij} . \tag{4.18}$$

Note that at leading order in v_0, the average of δx_i vanishes, which means that the average position $\bar{x}_i$ of the i^{th} particle coincides with its equilibrium position $x_i^{(\rm eq)}$. This implies in particular that $s_i^2 = \langle \delta x_i^2 \rangle_{\rm st}$ and $g_{i,n}^2 = \langle (\delta x_{i+n} - \delta x_i)^2 \rangle_{\rm st}$.

4.3.1 Inverting the Hessian matrix $\mathbf{H}_{\rm CM}$

Given the complicated form of the matrix $\mathbf{H}_{\rm CM}$ in Eq. (4.14), it might seem difficult to invert it analytically. However, we use the fact that the Hessian matrix of the Calogero-Moser model can be expressed in terms of the Hessian matrix $\mathbf{H}_{\rm L}$ of Dyson's Brownian motion as $\mathbf{H}_{\rm CM} = \mathbf{H}_{\rm L}^2$ where $\mathbf{H}_{\rm L}$ is given by [75]

$$(\mathbf{H}_{\rm L})_{ij} = \delta_{ij} \Big[1 + \sum_{\substack{n=1 \\ n \neq i}}^{N} \frac{1}{(x_i^{(\rm eq)} - x_n^{(\rm eq)})^2} \Big] - \frac{(1-\delta_{ij})}{(x_i^{(\rm eq)} - x_j^{(\rm eq)})^2}. \tag{4.19}$$

The covariance in Eq. (4.18) then becomes

$$\langle \delta x_i \delta x_j \rangle_{\rm st} \simeq v_0^2 \left(\mathbf{H}_{\rm L}^{-4} \right)_{ij} . \tag{4.20}$$

It turns out that the matrix $\mathbf{H}_{\rm L}$ can be diagonalized exactly using the Hermite polynomials [168]. Its eigenvalues are simply the integers from 1 to N, and the normalized eigenvector ψ_λ associated to the eigenvalue λ has components given by

$$(\psi_\lambda)_i = \frac{u_\lambda \left(x_i^{(\rm eq)} \right)}{\sqrt{\sum_{n=1}^{N} u_\lambda \left(x_n^{(\rm eq)} \right)^2}}, \quad \text{with } u_\lambda(x) = 2^{\lambda-1} \frac{(N-1)! H_{N-\lambda}(x)}{(N-\lambda)! H_{N-1}(x)}. \tag{4.21}$$

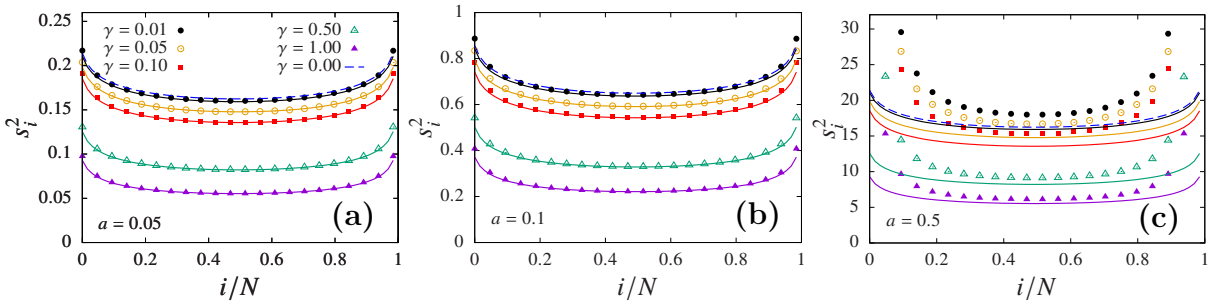

Figure 4.9: Numerically computed variance of particle positions $s_i^2 \equiv \langle x_i^2 \rangle - \langle x_i \rangle^2$ (points) in the steady-state of active CM model for different values of the flipping rate γ keeping the activity parameter a fixed at 0.05 in (a), 0.1 in (b) and 0.5 in (c) for the system size $N = 64$. The dashed blue line represents our theoretical expectation given in Eq. (4.33). In the first two panels, the matching between numerical and analytical results becomes more and more promising as the flipping rate γ is reduced from 1. However, in the last panel where the activity is very high, the approximation used in the theoretical calculation is not valid. Therefore, the theoretical formula is no longer correct.

Using the eigenvalue decomposition

$$\left(\mathbf{H}_{\mathrm{L}}^{-4}\right)_{ij} = \sum_{\lambda=1}^{N} \frac{(\psi_\lambda)_i (\psi_\lambda)_j}{\lambda^4}, \tag{4.22}$$

the covariance in Eq. (4.20) then simplifies to

$$\langle \delta x_i \delta x_j \rangle_{\mathrm{st}} \simeq v_0^2 \sum_{\lambda=1}^{N} \frac{1}{\lambda^4} \frac{u_\lambda\left(x_i^{(\mathrm{eq})}\right) u_\lambda\left(x_j^{(\mathrm{eq})}\right)}{\sum_{n=1}^{N} u_\lambda\left(x_n^{(\mathrm{eq})}\right)^2}. \tag{4.23}$$

From this expression, the variance $\langle \delta x_i^2 \rangle$ turns out to be

$$\langle \delta x_i^2 \rangle_{\mathrm{st}} \simeq v_0^2 \sum_{\lambda=1}^{N} \frac{1}{\lambda^4} \frac{u_\lambda\left(x_i^{(\mathrm{eq})}\right)^2}{\sum_{n=1}^{N} u_\lambda\left(x_n^{(\mathrm{eq})}\right)^2}. \tag{4.24}$$

These results are similar to the active DBM but with a $1/\lambda^4$ factor instead of $1/\lambda^2$ [109]. This leads to a faster convergence of the sum. Later, we will discuss that this results in some interesting differences between the two models. In what follows, we will analyze the results derived in Eqs. (4.23) and (4.24) in the large N limit to obtain some nice scaling relations for the variance and the covariance.

4.3.2 Variance and covariance of particle positions in the large N limit

We now make the same approximations as done in Ref. [109] in the limit $N \to \infty$. We first note that even though the summation in Eq. (4.23) runs from 1 to N, the sum gets dominant contribution from the smaller values of λ. In particular, for $\lambda \ll N$, the function $u_\lambda\left(x_i^{(\mathrm{eq})}\right)$ has a simplified expression [109]

$$u_\lambda\left(x_i^{(\mathrm{eq})}\right) \simeq (2N)^{\frac{\lambda-1}{2}} U_{\lambda-1}\left(\frac{x_i^{(\mathrm{eq})}}{\sqrt{2N}}\right), \tag{4.25}$$

in terms of the Chebyshev polynomial of the second kind $U_\lambda(w)$ of order λ. Moreover for $|w| < 1$, $U_\lambda(w)$ can be written as

$$U_\lambda(w) = \frac{\sin\big((\lambda+1)\arccos(w)\big)}{\sqrt{1-w^2}}. \tag{4.26}$$

To fully simplify the correlation in Eq. (4.23), we still need to simplify the denominator $\sum_{n=1}^{N} U_{\lambda-1}\left(\frac{x_n^{(\mathrm{eq})}}{\sqrt{2N}}\right)^2$ in this expression. Remember that as N becomes large, the density of the Hermite zeroes approaches the Wigner semi-circle. Moreover, the difference between successive roots $\left[\frac{x_n^{(\mathrm{eq})}}{\sqrt{2N}} - \frac{x_{n-1}^{(\mathrm{eq})}}{\sqrt{2N}}\right] \sim \frac{1}{N}$. Therefore, we can change the aforementioned summation to an integration with an appropriate measure as follows:

$$\sum_{n=1}^{N} U_{\lambda-1}\left(\frac{x_n^{(\mathrm{eq})}}{\sqrt{2N}}\right)^2 \simeq N \int_{-1}^{1} dw \frac{2\sqrt{1-w^2}}{\pi} U_{\lambda-1}(w)^2 = N. \tag{4.27}$$

Finally plugging the approximations from Eqs. (4.25)-(4.27) in Eq. (4.23) and taking the $N \to \infty$ limit, we find that the covariance $\langle \delta x_i \delta x_j \rangle_{\mathrm{st}}$ satisfies the scaling relation

$$\langle \delta x_i \delta x_j \rangle_{\mathrm{st}} \simeq \frac{v_0^2}{N}\, \mathcal{C}\left(\frac{x_i^{(\mathrm{eq})}}{\sqrt{2N}}, \frac{x_j^{(\mathrm{eq})}}{\sqrt{2N}}\right), \tag{4.28}$$

with the scaling function $\mathcal{C}(w,z)$ defined as

$$\mathcal{C}(w,z) = \sum_{\lambda=1}^{N} \frac{1}{\lambda^4} U_{\lambda-1}(w) U_{\lambda-1}(z), \tag{4.29}$$

and both the scaled variables w and z lie between $[-1, 1]$. In fact, the sum can actually be computed explicitly, leading to

$$\mathcal{C}(w,z) = \frac{c(\arccos(w), \arccos z)}{\sqrt{1-w^2}\sqrt{1-z^2}}, \quad \text{with} \tag{4.30}$$

$$c(u,v) = \frac{1}{6}\Big[\frac{uv}{2}(u^2+v^2) + \frac{\pi}{4}(|u-v|^3 - (u+v)^3 + \pi^2 uv\Big], \tag{4.31}$$

$$= \frac{v}{12}(\pi - u)(2\pi u - u^2 - v^2) \text{ for } u > v. \tag{4.32}$$

From the expression of the covariance, one can easily get the variance of the position for a single particle as

$$\langle \delta x_i^2 \rangle_{\rm st} \simeq \frac{v_0^2}{N}\, \mathcal{V}\left(\frac{x_i^{(\rm eq)}}{\sqrt{2N}}\right), \text{ with } \mathcal{V}(w) = \frac{\arccos^2(w)(\pi - \arccos(w))^2}{6(1-w^2)}. \tag{4.33}$$

In Fig. 4.9, we compare this analytical formula (Eq. (4.33)) with the numerically computed variance of particle positions in the steady state. The comparison is done across various values of the activity parameters v_0 and γ in a system with $N = 64$. The formula provided in Eq. (4.33) (labeled by the dashed line in Fig. 4.9) appears to be valid for sufficiently large values of v_0. However, it is evident that the flip rate γ needs to be very low.

Since for a general particle $x_i^{(\rm eq)} \sim \sqrt{N}$, the only real N dependence in (4.28) and (4.33) is in the prefactor and we find that the variance and covariance of the particle positions decay as $\langle \delta x_i^2 \rangle_{\rm st} \sim 1/N$ for large N. For particles that are far away in the bulk, i.e. when $x_i^{(\rm eq)} \ll \sqrt{N}$, the first few orders of the expansion of $\mathcal{V}(w)$ near $w = 0$ are given by,

$$\mathcal{V}(w) = \frac{\pi^4}{96} + \frac{\pi^4}{96}\Big(1 - \frac{8}{\pi^2}\Big)w^2 + \frac{\pi^4}{96}\Big(1 - \frac{32}{\pi^2} + \frac{16}{\pi^4}\Big)w^4 + \mathcal{O}(w^6), \tag{4.34}$$

and we see that the $1/N$ decay also holds at the leading order. This is similar to the behavior obtained in Ref. [109] for the active Dyson's Brownian motion. However, the main difference is that, due to the faster convergence of the series in Eq. (4.29), these results are also valid for the edge particles. Indeed, expanding $\mathcal{V}(w)$ near the edge (since $x_i^{(\rm eq)} \sim \sqrt{2N}$ for the edge particles, we replace $w = (1 - \epsilon)$ in Eq. (4.33) and take the

$\epsilon \to 0^+$ limit) we find

$$\mathcal{V}(1-\epsilon) = \frac{\pi^2}{6} - \frac{\pi}{3}\sqrt{2\epsilon} + \mathcal{O}(\epsilon). \tag{4.35}$$

We see that there is a finite limit, which indicates that for large N the variance decays as $\langle \delta x_i^2 \rangle_{\rm st} \sim 1/N$ even for the edge particles. This is very different from the active DBM which exhibits different scaling behaviors for the bulk and the edge particles [109]. For the active DBM, the equivalent of the function $\mathcal{V}(w)$ diverges near the edges, which shows that the $1/N$ scaling breaks down, and an alternative analysis is required to obtain the variance of the position of the edge particles. Nothing of the sort seems to occur for the active CM: the leading order decay of the variance is the same regardless of whether the particle is in the bulk or at the edge. All of this is also true for the covariance (4.28).

As a remark, one can use (4.35) along with the asymptotics of the Hermite zeros at the edge to obtain the behavior of the edge particles, for which $m = N - i = \mathcal{O}(1)$,

$$\langle \delta x_{N-m}^2 \rangle_{\rm st} \simeq \frac{v_0^2}{N}\left(\frac{\pi^2}{6} - \frac{\pi}{3}\sqrt{-a_m}\, N^{-1/3} + \mathcal{O}(N^{-2/3})\right), \quad \text{(for edge particles)}. \tag{4.36}$$

Comparing the values of position fluctuations to other existing length scales in the system, one can derive the criterion of the crossovers observed in the steady-state density profile. We first compare the typical displacements ($\sim v_0/\sqrt{N}$) of the particle with the typical inter-particle separation ($\sim 1/\sqrt{N}$), we get Lindemann's ratio

$$\eta_i = \frac{\sqrt{\langle \delta x_i^2 \rangle_{\rm st}}}{\left(x_{i+1}^{(\rm eq)} - x_i^{(\rm eq)}\right)} \sim \frac{v_0\,\sqrt{N}}{\sqrt{N}} \sim v_0. \tag{4.37}$$

Thus, if v_0 is very small ($\ll 1$), the particle fluctuations are much less compared to the mean spacing between successive particles. This situation corresponds to the density profiles with sharp peaks and refers to the weakly active regime. On the other hand, when the particle fluctuations become comparable to the total support of the density profile in the passive limit $x_e = \sqrt{2N}$, then the ratio

$$\frac{\sqrt{\langle \delta x_i^2 \rangle_{\rm st}}}{x_e} \sim \frac{v_0}{N} \tag{4.38}$$

suggests that when $v_0 \sim \mathcal{O}(N)$, the particle fluctuations are of the order of total support

of the density profile in the passive case which in turn implies very strong activity and corresponds to the bell-shaped density profile. Thus the transition from weakly active to intermediate active region occurs when $v_0 \sim \mathcal{O}(1)$ and the second transition, from intermediate to strongly active region happens at $v_0 \sim \mathcal{O}(N)$. Notice that the transition regions are consistent with the phase diagram shown in Fig. 4.8 as well. This argument also explains why in the strongly active regime, while the total support of the density is $[-aN, aN]$, the bulk of the density is still contained in an interval of size $\sim \sqrt{N}$. Indeed in this regime, the density is dominated by the fluctuations of the particles, which are typically of order $\sqrt{\langle \delta x_i^2 \rangle_{\rm st}} \sim v_0/\sqrt{N} = a\sqrt{N}$ (assuming that the (4.33) still gives the correct order of magnitude for the typical fluctuations in this regime).

Extension to finite γ. It is actually possible to extend the present results to finite values of γ. The derivation will be presented in a future paper [167]. The idea is to start again from the linearized equation of motion (4.13), and to solve it in Fourier space to obtain an expression of the covariance $\langle \delta x_i \delta x_j \rangle_{\rm st}$ for any value of γ. Going back to real space and taking the large N limit, we arrive at

$$\langle \delta x_i \delta x_j \rangle_{\rm st} \simeq \frac{v_0^2}{N} \mathcal{C}^\gamma \left(\frac{x_i^{(\rm eq)}}{\sqrt{2N}}, \frac{x_j^{(\rm eq)}}{\sqrt{2N}} \right) \quad , \tag{4.39}$$

$$\mathcal{C}^\gamma(w,z) = \sum_{\lambda=1}^{\infty} \frac{1}{\lambda^2(\lambda^2+2\gamma)} \frac{\sin(\lambda \arccos w)}{\sqrt{1-w^2}} \frac{\sin(\lambda \arccos z)}{\sqrt{1-z^2}} \, . \tag{4.40}$$

For the variance, this reads

$$\langle \delta x_i^2 \rangle_{\rm st} \simeq \frac{v_0^2}{N} \mathcal{V}^\gamma \left(\frac{x_i^{(\rm eq)}}{\sqrt{2N}} \right) \quad , \quad \mathcal{V}^\gamma(u) = \sum_{\lambda=1}^{\infty} \frac{1}{\lambda^2(\lambda^2+2\gamma)} \frac{\sin^2(\lambda \arccos u)}{1-u^2} \, . \tag{4.41}$$

In the limit $\gamma \to 0$ we recover the previous results (4.28) and (4.33), while for $\gamma \gg 1$ we recover the results for the passive Calogero-Moser model derived in Ref. [109], with an effective temperature $v_0^2/(2\gamma)$. Here, however, the sums cannot be computed explicitly. In Fig. 4.9, we see that the agreement with numerical simulations is very good for small values of a (up to $a \sim 0.1$), for all values of γ.

4.3.3 Variance of interparticle distance

The expression of the covariance can also be used to obtain the variance of the distance between two particles. Indeed

$$\langle(\delta x_i - \delta x_{i+n})^2\rangle_{\rm st} = \langle \delta x_i^2\rangle_{\rm st} + \langle \delta x_{i+n}^2\rangle_{\rm st} - 2\langle \delta x_i \delta x_{i+n}\rangle_{\rm st}. \tag{4.42}$$

One can use the results from the previous section to estimate each term in Eq. (4.42). This leads to

$$\langle(\delta x_i - \delta x_{i+n})^2\rangle_{\rm st} = \frac{v_0^2}{N}\mathcal{D}\Big(\frac{x_i^{(\rm eq)}}{\sqrt{2N}}, \frac{x_{i+n}^{(\rm eq)}}{\sqrt{2N}}\Big), \tag{4.43}$$

where $\mathcal{D}(w,z) = \mathcal{V}(w) + \mathcal{V}(z) - 2\mathcal{C}(w,z)$ with $\mathcal{C}$ and $\mathcal{V}$ are given in Eq. (4.30) and Eq. (4.33) respectively. Let us examine the behavior of this observable near the center of the quadratic well. In the limit where both w and z are close to zero, $\mathcal{D}(w,z)$ admits a simple expression. Indeed in this limit,

$$\mathcal{D}(w,z) = \frac{\pi^2}{24}(w-z)^2 + \mathcal{O}(w^3, z^3) \tag{4.44}$$

Using the fact that near $w = 0$, $x_i^{(\rm eq)} - x_{i+n}^{(\rm eq)} \simeq \frac{\pi n}{\sqrt{2N}}$. Eqs. (4.43) and (4.44) lead to the variance of mid-particle gap ($i = N/2$)

$$g_n^2 \equiv \langle\Big(\delta x_i - \delta x_{i+n}\Big)^2\rangle_{\rm st} \simeq \frac{\pi^4}{96}\frac{v_0^2}{N^3}n^2, \quad i = N/2. \tag{4.45}$$

Upon comparing this theoretical model with numerical findings in Fig.4.10, we observe a notable agreement between theoretical predictions and numerical data, particularly evident for lower values of n. Notice that the agreement gets better and better with decreasing γ which is not surprising since the formula is valid only in the $\gamma \to 0$ limit. Contrary to what we observed in Ref. [109] for the active DBM, the results (4.43) and (4.45) seem to be compatible with numerical simulations even for $n = \mathcal{O}(1)$ (see Fig. 4.10). In particular, the variance of mid-gap near $x = 0$ is correctly given to leading order by Eq. (4.45) with $n = 1$. This is again due to the faster convergence of the series defining $\mathcal{C}(x,y)$ and $\mathcal{V}(x)$.

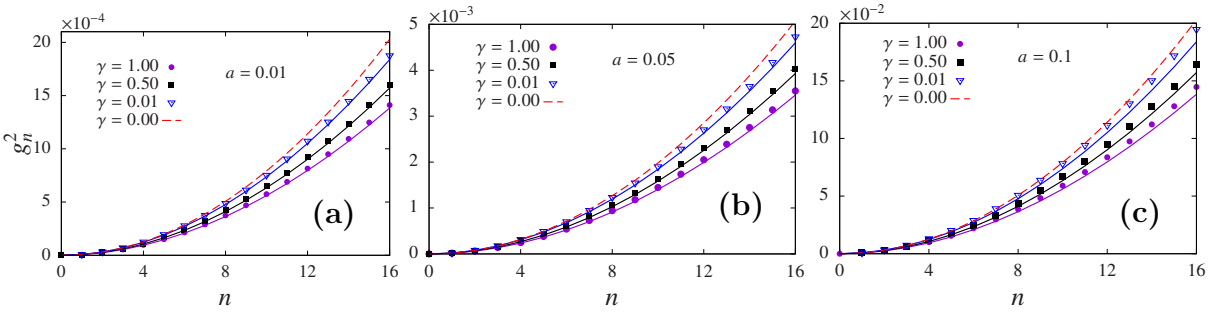

Figure 4.10: Variance of the gap g_n^2 as defined in Eq. (4.45), is plotted as a function of n for two different values of the activity parameters, $a = 0.01$, 0.05, and 0.1, in panels (a), (b) and (c) respectively, within a system of 128 particles for three different choices of the flipping rate γ. The points represent the numerically computed variance of the gap, while the solid lines indicate the corresponding theoretical expectations given by Eq. (4.46) with $i = N/2$. The red dashed line represents the approximated theoretical form of g_n^2 given in Eq. (4.45) obtained in the $\gamma \to 0$ limit. For small values of n, the numerical results show good agreement with the theoretical predictions.

Extension to finite γ. The results (4.39) and (4.41) enable us to generalize to finite γ the expressions (4.43) and (4.45). Indeed,

$$\langle (\delta x_i - \delta x_{i+n})^2 \rangle_{\rm st} = \frac{v_0^2}{N} \mathcal{D}^\gamma \left(\frac{x_i^{(\rm eq)}}{\sqrt{2N}}, \frac{x_{i+n}^{(\rm eq)}}{\sqrt{2N}} \right) \quad , \text{ with} \tag{4.46}$$

$$\begin{aligned} \mathcal{D}^\gamma(w,z) &= \mathcal{V}^\gamma(w) + \mathcal{V}^\gamma(z) - 2\mathcal{C}^\gamma(w,z) \\ &= \sum_{\lambda=1}^{N} \frac{1}{\lambda^2(\lambda^2+2\gamma)} \left(\frac{\sin(\lambda \arccos w)}{\sqrt{1-w^2}} - \frac{\sin(\lambda \arccos z)}{\sqrt{1-z^2}} \right)^2 . \end{aligned} \tag{4.47}$$

As in the $\gamma \to 0$ case, we could not derive a simple formula for the variance of the gap $g_{i,n}^2$ at any finite γ, even for $i = N/2$. The formula for the variance of the gap, given in Eq.(4.46), has been compared with numerical results in Fig.4.10 for $i = N/2$. We find a good agreement between the theoretical predictions and the numerical results for all γ at small v_0.

4.3.4 Validity of the approximation

The result (4.45) allows us to test *a* posteriori the validity of the small v_0 approximation made at the beginning of this section. This requires that the typical variations of the distance between successive particles $g_{i,1}$ is much smaller than the average distance $\Delta_{i,1}$.

Thus we get that our results should be valid when the following ratio is small (assuming that γ is small and that i is close to $N/2$ to simplify the evaluation),

$$\frac{g_{i,1}}{\Delta_{i,1}} \sim \frac{v_0/N^{3/2}}{1/\sqrt{N}} = \frac{v_0}{N} \, . \tag{4.48}$$

Thus we find that the weak noise approximation should always hold as long as $v_0 \ll N$, i.e. in the entire 'solid' and 'liquid' regimes.

4.4 Summary and outlook

We extended the analysis of active Dyson's Brownian motion presented in Refs. [108, 109] to the active Calogero-Moser system described by Eq. (4.2). In the steady state, we focused on computing the density profile of the particles. As the activity in the system increases, the density profiles exhibit interesting crossovers from a sharply peaked profile to a smooth bell-shaped profile, passing through an intermediate Wigner semi-circle profile. The first crossover is analogous to a crystal-to-liquid transition, where the 'crystal' phase is characterized by sharp peaks in the density profile, and the 'liquid' phase has a smooth Wigner semi-circular density profile without such peaks. To quantify these transitions, we computed Lindemann's ratio, which compares the fluctuations in particle positions to the average gaps between successive particles. As observed in the active DBM [108], we also found that the density profile in the steady state retains the shape of the Wigner semi-circle even at sufficiently large activity. However, at extremely high activity, the density profile transitions to a bell shape. To characterize this second crossover, we measured the deviation of the density profile from the Wigner semi-circle by computing χ. Based on these values, we constructed a 'phase' diagram in the a, $1/\gamma$ plane.

Using Hessian theory, we computed the covariances of particle positions in the small activity (small v_0) limit, which allowed us to calculate the variance of interparticle gaps. Closed-form expressions for the variance of particle positions and interparticle gaps were obtained in the long persistence time limit (small γ) for large system sizes. These theoretical expressions remain valid at sufficiently large v_0 but require a very large persistence

time limit (see Figs. 4.9 and 4.10). The active CM model exhibits some distinctive behaviors compared to the active DBM. As a manifestation of the short-range interactions in this model, the fluctuations of particles, both at the edges and in the bulk, decay with system size as $\sim 1/N$. This contrasts with the active DBM, where long-range interactions cause the bulk fluctuations to decay as $\sim 1/N$, but edge fluctuations decay as $\sim 1/N^{2/3}$ [109]. By comparing the fluctuations in particle positions with other existing length scales, we also identified the crossover regions from weakly active to intermediate active, and finally to strongly active regimes. The transition from weakly active to intermediate active occurs at $v_0 \sim \mathcal{O}(1)$, while the transition to the strongly active regime takes place at $v_0 \sim \mathcal{O}(N)$. The analytical computation of particle position covariances was also extended to finite γ, yielding exact results up to a summation.

This study has numerous interesting extensions and outlooks. The very first task would be to analytically comprehend the bell-shaped density profile emerging in the large activity limit in both the active DBM and active CM models. It's now evident that, for both models, the density profile maintains its passive structure even at sufficiently large activity. The next question arises: does a similar behavior occur in other many-particle interacting systems, such as the harmonically confined Riesz gas [97]? Additionally, what happens to this robustness if one shortens the range of interactions [99]?

Chapter 5

Conclusions

In this thesis, we investigated the equilibrium and non-equilibrium properties of strongly interacting systems in one dimension. Specifically, we focused on the Riesz gas, where the particles interact through pairwise repulsive power-law interactions of the form $\sim 1/r^k$, with r representing the distance between two particles. This repulsive interaction is counterbalanced by an overall confining harmonic potential. Special values of k correspond to some important models such as the Dyson's log-gas ($k = 0^+$) [29, 30], the 1-D one-component plasma ($k = -1$) [47–50], the Calogero-Moser model ($k = 2$) [60, 61, 65, 68], 3-D Coulomb gas confined in one dimension ($k = 1$) [169], hard rods ($k \to \infty$) [78, 80]. Experimental realizations of this model in cold atom systems have now become possible (ions [88–90], dipolar Bose gas [91, 92], coupled lasers [93]). Since power-law interactions describe a broad range of physical systems, including gravitational systems [18, 27], Coulomb systems [14, 15] and 2D hydrodynamics [19], it is important to understand the physics of this Riesz gas. A coarse-grained description of these models in thermal equilibrium has been developed [97]. The saddle point method was then used to compute the average density profiles for the general $k > -2$. While most studies focus on mean density, examining fluctuations is important for a complete characterization of the system.

In the first part of the thesis, we analyzed the microscopic properties of these systems in thermal equilibrium by studying the statistics of the gap between successive particles. We found a power-law system-size dependence for the variance of the bulk gap as N^{-b_k}. Specifically, for the mid-gap, we conjectured the k-dependence of the exponent b_k and verified it via direct Monte-Carlo simulations. The conjecture was further validated through

two (semi)analytical techniques: the microscopic Hessian and the quadratic approximation of the associated field theory. It is important to re-emphasize that the entropy, which was irrelevant in determining the density profile, plays a significant role in fluctuations in the range $-1 < k < 0$. We expect that the microscopic Hessian theory can be used to compute the connected correlators of the form $\langle x_i x_j \rangle - \langle x_i \rangle \langle x_j \rangle$ for all $k > -2$, except in the range $-1 < k < 0$. For the log-gas ($k = 0^+$) and Calogero-Moser ($k = 2$) models, the Hessian theory accurately captures these correlations at low temperatures ($T \sim \mathcal{O}(1)$) [75]. However, this has not yet been verified for general k, and it would be interesting to investigate further [170]. We anticipate that the microscopic Hessian technique can be applied to any many-particle interacting system where the fluctuations of the gaps decrease more rapidly than their averages as the system size increases. The field theory approach that we have used in the all-to-all coupled Riesz gas to compute the system size scaling for the variance of the bulk gap can easily be utilized in the SR Riesz gas studied in Ref. [99].

After studying the mean and variance of gaps between successive particles in the bulk, we moved on to study the system-size scaling of their distributions. As in the log-gas, we found that the distribution of s (gap scaled by its mean) in 1DOCP converges very quickly with system size N but fails to generalize the Wigner surmise for log-gas. We found the distribution of $\tilde{s}$ (gap scaled by its fluctuations), $\tilde{P}_N(\tilde{s})$, to be more universal than the distribution $P_N(s)$ in the sense that $\tilde{P}_N(\tilde{s})$ is independent of system size except for $-1 < k < 0$, whereas $P_N(s)$ is system-size independent only for $k = -1$ and $k = 0^+$. The scaling behavior of the distributions is summarized in Fig. 2.1.

In the second part of this thesis, we analyzed how the density profile changes as the range of interaction is varied in systems with power-law interactions. To adjust the range of interaction, we varied the parameter d, which represents the maximum number of particles a given particle can interact with on either side (see Eq. (3.1)). Specifically, we considered two model systems: the 1DOCP and the log-gas described by the energy function given in Eq. (3.3). We found that as the parameter $f(= d/N)$ is varied from 1 to 0, the density profiles in both models transition from a finitely supported profile to an infinitely extended Gaussian profile. Starting from the microscopic energy function given in Eq. (3.3), we derived the saddle point equations (in Appendix. A.3) that the equilibrium

density profile must satisfy for any values of $f \in (0, 1)$. Here, we want to emphasize that these saddle point equations are valid for general Riesz gas (described in Eq. (3.1)) for any $k \in (-2, 1)$. Interestingly, we found that the density profile for any finite f in the large N limit exhibits the same system-size scaling as in the all-to-all coupling case, although the scaling functions explicitly depend on the parameter f. For the 1DOCP model, we solved the saddle point equations and found exact analytical expressions for the scaling functions across the entire range of f. For the log-gas, solving the relevant SPEs is more challenging. We demonstrated the density crossover numerically and provided approximate analytical solutions only in the limits $f \to 1$ and $f \to 0$. It is important to point out that the approximations used to solve the saddle point equations for the log-gas in the $f \to 1$ and $f \to 0$ limits are also valid for FR Riesz gas (described in Eq. (3.1)) with $k \in (0, 1)$. Therefore, the problem of finding the equilibrium density profile in these two limits for $k \in (0, 1)$ can similarly be mapped to a problem in the corresponding all-to-all coupling domain, with the constraint that a specific number of particles remain inside a finite region while the rest stay outside. However, these problems for $k \in (0, 1)$ in the all-to-all coupling domain have not yet been solved, except for the log-gas case [39]. Nevertheless, computing the density profile in the finite-range Riesz gas for any $-2 < k < 1$ seems to be a difficult and challenging task. Extending our gap statistics analysis to the finite-range Riesz gas would be particularly interesting. Investigating how 'level repulsion' in the log-gas or 'level clustering' in the 1DOCP changes with variations in interaction range would be a compelling problem to explore.

In the final part of this thesis, we explored a non-equilibrium setup involving N run-and-tumble particles confined in a one-dimensional harmonic trap. The particles interact through pairwise repulsive inverse-square law interactions (force $\sim 1/x^3$), forming an active version of the Calogero-Moser model. In the steady state, as the system's activity increased, we observed intriguing crossovers in the density profile: from a profile with multiple sharp peaks reminiscent of a crystal to a smooth Wigner semi-circle resembling a liquid, and finally to a bell-shaped density profile. To analytically understand these crossovers, our collaborators L. Touzo, P. L. Doussal, and G. Schehr from the University of Paris City and Sorbonne University, respectively derived a formula for the variance of particle positions in the small noise limit. They used the Hessian approach, similar to the

method applied in the active Dyson's Brownian motion in Ref. [109]. The covariance of particle positions has also been computed which leads to the computation of the variance of interparticle separations.

Our study could be extended to the harmonically confined Riesz gas described in Eq.(1.3) for $k > 0$. For the active Dyson's Brownian motion model (corresponding to $k = 0^+$) and active Calogero-Moser model (corresponding to $k = 2$), many analytical results have been obtained because the eigenvalues and eigenfunctions of their Hessian matrices are known [168]. However, these are not known for other values of k. Despite this, the covariance of particle positions can still be computed by numerically inverting the Hessian matrix [98]. Investigating the gap distributions in the active Dyson's Brownian motion or active 1DOCP would be particularly interesting [110].

Appendix A

Appendix

A.1 Numerical details

In this Appendix, we provide details of our numerical computations. In chapter 2, we compute the mean and variance of the bulk gap using Monte Carlo (MC) simulations. For a given processor, we disregard about initial 10^6 MC cycles. By MC cycle, we mean $\mathcal{O}(N)$ Metropolis steps. We then collect data of about 10^6 samples. This process is simultaneously executed in around $N/2$ processors thereby making the number of samples to be around 10^8. Needless to mention, the exact numbers depend on whether we achieve satisfactory convergence of our results for a given N and k. For all the spacing distributions (which contain a total of $(N-1)$ gaps), we have used 10^6 MC samples. Both J_0 and J are taken to be unity for log-gas ($k = 0^+$) and for any other values of $k > -2$ respectively. To determine the density profiles in chapter. 3, we compute the histograms of particle positions obtained through MC simulations at inverse temperature $\beta = 1$. For each case, the system is allowed to thermalize over 10^6 MC cycles initially. We perform averages over 10^7 samples to determine the density profiles. In chapter 4, the Euler method [171] is used to evolve the positions of the particles in the active Calogero-Moser model, following the equation of motion given in Eq. (4.2). To ensure that the particles in the underlying systems do not cross during the evolution, we chose a time step of $dt \sim 10^{-5}$. Starting from any initial configuration, the particles are evolved for a long time, $t \sim \mathcal{O}(10^5)$, to ensure that the system reaches a steady state. All physical quantities such as the density profiles, the variance of particle positions, and variance

of interparticle gaps in the steady state are obtained by averaging over approximately $\sim 10^{11}$ samples of steady-state configurations.

A.2 System size scaling of the matrix elements M and H

In chapter. 2, we were interested in finding the system size scaling of the variance of gap between successive particles. The variance of the bulk gap and the coarse-grained bulk gap are described by MH and FT respectively and these are in turn governed by the matrices H and M respectively. Since they quantify similar physical quantities it is natural to compare the matrices element wise which is shown in Table A.1. We notice

	M_{ij}		H_{ij}	
Range of k	$i=j$	$\lvert i-j\rvert \sim \mathcal{O}(1)$	$i=j$	$\lvert i-j\rvert \sim \mathcal{O}(1)$
$k>1$	N^2	0	N^2	N^2
$0<k<1$	N^{1+k}	N^{1+k}	N^{1+k}	N^{1+k}
$-1<k<0$	$N^{\frac{2(1+k)}{(k+2)}}$	N^{1+k}	N	N^{1+k}
$-2<k<-1$	$N^{\frac{2(1+k)}{(k+2)}}$	N^{1+k}	N	N^{1+k}

Table A.1: System size dependence of the matrix elements M_{ij} and H_{ij} for different values of i and j. As we are interested mainly in the bulk part of the system we ignore such terms where $(i-j) \sim \mathcal{O}(N)$.

that the elements of matrices H and M have similar system size scaling for $0<k<1$, while for $k>1$ off-diagonal terms and for $-2<k<0$ the diagonal terms differ. The variance of the bulk gap is found by the numerical inversion of these matrices H and M. The scaling behavior of the elements of the inverse matrices is presented in Table. (A.2)

We observe that the inverse of the dominant term in the matrix M gives the scaling similar to the variance calculated by the numerical inversion of these matrices. This leads us to the conjecture for the variance given in Eq. (2.9). It is clear from Table. A.2 that except in the regime $-1<k<0$ the microscopic Hessian theory captures the system size dependence of variance of bulk gap whereas the quadratic field theory gives correct exponent b_k (consistent with MC simulation) for all $k>-2$.

	M_{ij}^{-1}		H_{ij}^{-1}	
Range of k	$i=j$	$\lvert i-j\rvert \sim \mathcal{O}(1)$	$i=j$	$\lvert i-j\rvert \sim \mathcal{O}(1)$
$k>1$	N^{-2}	0	N^{-2}	N^{-2}
$0<k<1$	$N^{-(1+k)}$	$N^{-(1+k)}$	$N^{-(1+k)}$	$N^{-(1+k)}$
$-1<k<0$	$N^{\frac{-2(1+k)}{(k+2)}}$	$N^{\frac{-2(1+k)}{(k+2)}}$	$N^{-(1+k)}$	$N^{-(1+k)}$
$-2<k<-1$	$N^{-(1+k)}$	$N^{-(1+k)}$	$N^{-(1+k)}$	$N^{-(1+k)}$

Table A.2: System size dependence of the matrix elements M_{ij}^{-1} and H_{ij}^{-1} for different values of i and j. Again we ignore such terms where $(i-j) \sim \mathcal{O}(N)$.

A.3 Field theoretic description of FR Riesz gas and the derivation of the saddle point equations

In this Appendix, we provide the derivation of the saddle point equations both for 1DOCP and log-gas described by the energy functions given in Eq. (3.3). As mentioned at the beginning of Sec. 3.2, for both the models with $0 < f < 1$ the support of the equilibrium density profile should consist of three regimes over which they behave differently. Such regimes naturally appear because the interaction felt by a particle in these three regimes is different since the number of other particles available to which it can interact, is different. Recall, we denote these regimes as the central part, the left edge part and the right edge part which are supported over the following regions $[-\ell_N, \ell_N]$, $[-b_N, -\ell_N)$ and $(\ell_N, b_N]$, respectively, with $0 < \ell_N < b_N$. On average, the central part contains $|1-2f|$ fraction of particles and the two edge parts contain the rest of the fraction of particles equally divided. Consequently, the free energy functional defined in Eq. (3.6) now reads

$$\bar{\Psi}[\rho_N(x)] = \Psi[\rho_N(x)] - \mu_1 \left(\int_{-\ell_N}^{\ell_N} dx \rho_N(x) - |1-2f| \right) \\ - \mu_2 \left(\int_{-b_N}^{-\ell_N} dx \rho_N(x) - \frac{(1-|1-2f|)}{2} \right) - \mu_3 \left(\int_{\ell_N}^{b_N} dx \rho_N(x) - \frac{(1-|1-2f|)}{2} \right), \tag{A.1}$$

where μ_1, μ_2 and μ_3 are the chemical potentials that ensure the following normalizations

$$\begin{aligned} &\int_{-\ell_N}^{\ell_N} \rho_N(x)\ dx = |1-2f| \ \text{ and} \\ &\int_{-b_N}^{-\ell_N} \rho_N(x)\ dx = \int_{\ell_N}^{b_N} \rho_N(x)\ dx = \frac{(1-|1-2f|)}{2}, \end{aligned} \tag{A.2}$$

in the central, the left edge and the right edge parts respectively. Due to the inversion symmetry of the microscopic energy function $\mathscr{E}(\{x_i\})$ in Eq. (3.3), we expect the equilibrium density profile to be symmetric about the origin (the center of the trap) which implies $\mu_2 = \mu_3$ in equilibrium.

The free energy functional defined in Eq. (3.4) is a combination of energy and entropy functionals $\Psi[\rho_N(x)] = \mathscr{E}[\rho_N(x)] - \beta^{-1}\mathcal{S}[\rho_N(x)]$. The entropy $\mathcal{S}[\rho_N(x)]$ can be computed by 'counting' the number of microscopic configurations compatible with a given density profile $\rho_N(x)$ which essentially provides $\mathcal{S}[\rho_N(x)] = -N\int dx \rho_N(x)\log\rho_N(x)$ [30, 36]. To find an expression for the energy functional $\mathscr{E}[\rho_N(x)]$ corresponding to the energy function in Eq. (3.3), we first notice that the functional $\mathscr{E}[\rho_N(x)]$ has the form

$$\mathscr{E}[\rho_N(x)] = \frac{N}{2}\int_{-b_N}^{b_N} x^2 \rho_N(x) dx + \mathscr{E}_I[\rho_N(x)], \tag{A.3}$$

where the first term comes from the confining potential in Eq. (3.3) and the second term $\mathscr{E}_I[\rho_N(x)]$ represents contribution from the interaction potential. To find the equilibrium density profile for large N, one needs to solve the following saddle point equation

$$\frac{\delta\bar{\Psi}[\rho_N(x)]}{\delta\rho_N(x)}\Big|_{\rho_N(x)=\varrho_N(x)} = 0, \tag{A.4}$$

subject to the normalisation conditions in Eq. (A.2) which arise by equating the derivatives of $\bar{\Psi}[\rho_N(x)]$ with respect ot μ_1 and μ_2 to zero, respectively.

As mentioned in Sec. 3.2, we numerically observe [from Figs. (3.2, 3.3) for 1DOCP and Figs. (3.4, 3.5) for log-gas] that the density profile possesses scaling form (see Eq. (3.11))with a N-dependent length scale $L_N \sim N^\alpha$ where α is given in Eq. (3.8). Using this scaling form in the expression of the free energy, it is easy to notice that the energy $\mathscr{E}[\rho_N(x)] \simeq N\int_{-b_N}^{b_N}(x^2/2)\ \rho_N(x)\ dx + \mathscr{E}_I[\rho_N(x)]$ scales as $N^{2\alpha+1}$, whereas the en-

tropy contribution scales as N. Therefore, for large N one can neglect the contribution of the entropy term in the saddle point calculation. The SPE in Eq. (A.4) now explicitly reads

$$\frac{Nx^2}{2} + \frac{\delta \mathscr{E}_I[\rho_N(x)]}{\delta \rho_N(x)}\bigg|_{\rho_N(x)=\varrho_N(x)} = \begin{cases} \mu_1 & \text{for} \quad -\ell_N \leq x \leq \ell_N \\ \mu_2 & \text{for} \quad \ell_N < |x| \leq b_N. \end{cases} \tag{A.5}$$

In the large N limit the functional $\mathscr{E}_I[\rho_N(x)]$ for a fixed f can be computed (for both the models) following the procedure in [97]. Since the form of the energy functional $\mathscr{E}_I[\rho_N(x)]$ turns out to be different for $1/2 \leq f \leq 1$ and $0 < f < 1/2$, we present the derivation of the SPEs for these two cases separately in the next subsections.

A.3.1 For $1/2 \leq f \leq 1$:

Note in this case $N/2 \leq d \leq N-1$. We first rewrite the interaction part of the energy function $\mathscr{E}(\{x_i\})$ in Eq. (3.3) as

$$\mathscr{E}_I(\{x_i\}) = \frac{1}{2}\left[\sum_{\substack{i=1 \\ i\neq j}}^{N}\sum_{j=1}^{N} - \sum_{i=1}^{N-d-1}\sum_{j=i+d}^{j=N} - \sum_{i=d+2}^{N}\sum_{j=1}^{j=i-d}\right] V(|x_i - x_j|). \tag{A.6}$$

Recalling the definition $\rho_N(x) = \frac{1}{N}\sum_{i=1}^{N}\delta(x-x_i)$, it is easy to convert the different terms into integrals as

$$\begin{aligned} \mathscr{E}_I[\rho_N(x)] =& \frac{N^2}{2}\int_{-b_N}^{b_N} dx \int_{-b_N}^{b_N} dx'\; V(x-x')\; \rho_N(x)\rho_N(x') \\ &- \frac{N^2}{2}\int_{-b_N}^{-\ell_N} dx \int_{x+\bar{\mathcal{D}}_x}^{b_N} dx'\; V(x-x')\; \rho_N(x)\; \rho_N(x') \\ &- \frac{N^2}{2}\int_{\ell_N}^{b_N} dx \int_{-b_N}^{x-\mathcal{D}_x} dx'\; V(x-x')\; \rho_N(x)\; \rho_N(x'), \end{aligned} \tag{A.7}$$

where $V(x)$ is specified in Eq. (3.3). The distances $\mathcal{D}_x$ and $\bar{\mathcal{D}}_x$ depend on density profile $\rho_N(x)$ as

$$\int_{x-\mathcal{D}_x}^{x} \rho_N(x')dx' = f = \int_{x}^{x+\bar{\mathcal{D}}_x} \rho_N(x')dx'. \tag{A.8}$$

These equations define $\mathcal{D}_x$ and $\bar{\mathcal{D}}_x$ that represent the distance one has to move starting from x to find f fraction of particles on the left and right side, respectively. Note these quantities, being an addition to the function of x, are also functionals of $\rho_N(x)$. In the following, we will refer to them as functions of x.

Note that, in writing down the interaction energy part $\mathscr{E}_I$ of the energy functional, we have ignored possible self-energy contribution [36, 130]. The reason behind this is that, in the large N limit the self-energy term remains subdominant compared to other terms in the free energy. Such self energy contribution for ATAC log-gas ($f = 1$) was shown to be of order $\sim N \int dx \rho_N(x) \log(\rho_N(x))$ in Ref. [36]. While writing the expression of $\mathscr{E}_I[\rho_N(x)]$, given a particle at x we are integrating x' over a region including the point x. For the log-gas interaction, two particles cannot stay at the same point. Hence the region near point x should be excluded in the integration of x' in the log-gas case. However for 1DOCP, one does not face any such problem. In order to correct for that, one needs to subtract a self energy contribution which for large N can be estimated as

$$\mathscr{E}_{\text{self}} \sim N^2 \int_{-b_N}^{b_N} dx \rho_N(x) \int_{x-\epsilon_x}^{x+\epsilon_x} dx' \rho_N(x') V(|x - x'|). \tag{A.9}$$

Here ϵ_x represents the smallest gap between two particles at position x, which in the large N limit for a given density profile $\rho_N(x)$ is given by $\epsilon_x \approx \frac{1}{N\rho_N(x)}$ [30]. After a few straightforward algebraic steps, the self-energy term for the log-gas ($V(x) = -\log(|x|)$) simplifies to

$$\mathscr{E}_{\text{self}} \sim N \int_{-b_N}^{b_N} \rho_N(x) \log[\rho_N(x)] dx + \text{constant}. \tag{A.10}$$

This term, however, is much smaller than the bulk interaction energy term of $\mathcal{O}(fN^2)$ in the large N limit. Hence, one can neglect the self energy contribution in the saddle point calculation for a fixed arbitrary value of f.

To obtain the SPE (A.5) explicitly, we perform functional derivative of $\mathscr{E}[\rho_N(x)]$ and for that we use the following results

$$\frac{\delta \mathcal{D}_x}{\delta \rho_N(z)} = -\frac{1}{\rho_N(x - \mathcal{D}_x)} \Theta(z - x + \mathcal{D}_x) \Theta(x - z). \tag{A.11}$$

$$\frac{\delta \bar{\mathcal{D}}_x}{\delta \rho_N(z)} = -\frac{1}{\rho_N(x + \bar{\mathcal{D}}_x)} \Theta(x + \bar{\mathcal{D}}_x - z) \Theta(z - x). \tag{A.12}$$

Performing the functional derivatives and using the above equations, we finally get the SPEs in all three regimes. The equation in the central regime $-\ell_N \leq x \leq \ell_N$ is given by

$$N\frac{x^2}{2} + N^2 \int_{-b_N}^{b_N} V(x'-x)\ \varrho_N(x')\ dx' \\ - \frac{N^2}{2}\Big[\int_{-b_N}^{-\ell_N} V(\bar{\mathcal{D}}_{x'})\ \varrho_N(x')\ dx' + \int_{\ell_N}^{b_N} V(\mathcal{D}_{x'})\ \varrho_N(x')\ dx'\Big] = \mu_1. \tag{A.13}$$

The SPEs in the left regime $-b_N \leq x < -\ell_N$ and the right regime $\ell_N < x \leq b_N$ are, respectively,

$$N\frac{x^2}{2} + N^2 \int_{-b_N}^{b_N} V(x'-x)\ \varrho_N(x')\ dx' - \frac{N^2}{2}\ \Big[2\int_{x+\bar{\mathcal{D}}_x}^{b_N} V(x'-x)\varrho_N(x')dx' \\ + \int_{-b_N}^{x} V(\bar{\mathcal{D}}_{x'})\varrho_N(x')dx' + \int_{\ell_N}^{x+\bar{\mathcal{D}}_x} V(\mathcal{D}_{x'})\varrho_N(x')dx'\Big] = \mu_2. \tag{A.14}$$

and

$$N\frac{x^2}{2} + N^2 \int_{-b_N}^{b_N} V(x'-x)\ \varrho_N(x')\ dx' - \frac{N^2}{2}\ \Big[2\int_{-b_N}^{x-\mathcal{D}_x} V(x'-x)\varrho_N(x')dx' \\ + \int_{x}^{b_N} V(\mathcal{D}_{x'})\varrho_N(x')dx' + \int_{x-\mathcal{D}_x}^{-\ell_N} V(\bar{\mathcal{D}}_{x'})\varrho_N(x')dx'\Big] = \mu_2. \tag{A.15}$$

Note in the ATAC ($f \to 1$) limit, the central part grows and both the edge regions shrink to the edge points of the central part. The terms inside the square brackets of Eqs. (A.13 - A.15) go to zero and consequently the SPEs corresponding to the edge parts reduce to the SPE of the central part evaluated at the edge points with $\mu_2 = \mu_1$.

A.3.2 For $0 < f < 1/2$

In this case $0 < d \leq N/2$, we rewrite the microscopic energy function $\mathscr{E}(\{x_i\})$ in Eq. (3.3) as

$$\mathscr{E}_I(\{x_i\}) = \frac{1}{2}\left[\sum_{\substack{i=1\\ i\neq j}}^{d}\sum_{j=1}^{i+d} + \sum_{\substack{i=d+1\\ i\neq j}}^{N-d}\sum_{j=i-d}^{j=i+d} + \sum_{\substack{i=N-d+1\\ i\neq j}}^{N}\sum_{j=i-d}^{j=N}\right] V(|x_i - x_j|). \tag{A.16}$$

In terms of the empirical density $\rho_N(x) = \frac{1}{N}\sum_{i=1}^{N}\delta(x-x_i)$, we convert the double sums in the above equation to double integrals and find

$$\begin{aligned}\mathscr{E}_I[\rho_N(x)] = \frac{N^2}{2}\int_{-b_N}^{-\ell_N} dx \int_{-b_N}^{x+\bar{\mathcal{D}}_x} dx' V(x-x')\rho_N(x)\rho_N(x') \\ + \frac{N^2}{2}\int_{-\ell_N}^{\ell_N} dx \int_{x-\mathcal{D}_x}^{x+\bar{\mathcal{D}}_x} dx'\ V(x-x')\ \rho_N(x)\ \rho_N(x') \\ + \frac{N^2}{2}\int_{\ell_N}^{b_N} dx \int_{x-\mathcal{D}_x}^{b_N} dx' V(x-x')\rho_N(x)\rho_N(x'),\end{aligned} \tag{A.17}$$

where the distance functions $\mathcal{D}_x$ and $\bar{\mathcal{D}}_x$ are defined in Eq. (A.8). In this case also we have neglected the self energy contribution for $V(x) = -\log(|x|)$. As can be seen from Eq. (A.10), this contribution can be neglected for $0 < f < 1/2$ also as long as it is kept fixed at a non-zero value (however small it could be) in the $N \to \infty$ limit. Inserting the above form for $\mathscr{E}_I[\rho_N(x)]$ in Eq. (A.5), one can get the SPEs for $0 < f < 1/2$. The SPE in the left regime $-b_N \le x < -\ell_N$ is given by

$$\begin{aligned}\frac{Nx^2}{2} + N^2\int_{-b_N}^{x+\bar{\mathcal{D}}_x} V(x'-x)\ \varrho_N(x')\ dx' \\ - \frac{N^2}{2}\left[\int_{-b_N}^{x} V(\bar{\mathcal{D}}_{x'})\varrho_N(x')\ dx' + \int_{-\ell_N}^{x+\bar{\mathcal{D}}_x} V(\mathcal{D}_{x'})\varrho_N(x')\ dx'\right] = \mu_2,\end{aligned} \tag{A.18}$$

and in the right regime $\ell_N < x \le b_N$ we get

$$\begin{aligned}\frac{Nx^2}{2} + N^2\int_{x-\mathcal{D}_x}^{b_N} V(x'-x)\ \varrho_N(x')\ dx' \\ - \frac{N^2}{2}\left[\int_{x}^{b_N} V(\mathcal{D}_{x'})\ \varrho_N(x')\ dx' + \int_{x-\mathcal{D}_x}^{\ell_N} V(\bar{\mathcal{D}}_{x'})\ \varrho_N(x')\ dx'\right] = \mu_2.\end{aligned} \tag{A.19}$$

In the central regime $-\ell_N \leq x \leq \ell_N$ we get

$$\begin{aligned}
&\frac{Nx^2}{2}+N^2\int_{x-\mathcal{D}_x}^{x+\bar{\mathcal{D}}_x} V(x'-x)\ \varrho_N(x')\ dx' \\
&\quad-\frac{N^2}{2}\left[\int_{x-\mathcal{D}_x}^{x} V(\bar{\mathcal{D}}_{x'})\ \varrho_N(x')\ dx'+\int_{x}^{x+\bar{\mathcal{D}}_x} V(\mathcal{D}_{x'})\ \varrho_N(x')\ dx'\right] \\
&\quad+\frac{N^2}{2}\int_{-b_N}^{-\ell_N}\left[V(x'-x)-V(\bar{\mathcal{D}}_{x'})\right]\Theta(x'+\bar{\mathcal{D}}_{x'}-x)\ \varrho_N(x')\ dx' \\
&\quad+\frac{N^2}{2}\int_{\ell_N}^{b_N}\left[V(x'-x)-V(\mathcal{D}_{x'})\right]\Theta(x-x'+\mathcal{D}_{x'})\ \varrho_N(x')\ dx'=\mu_1.
\end{aligned} \tag{A.20}$$

A.4 Explicit solution of the saddle point equation for FR 1DOCP

In this Appendix, we provide details on solving the SPEs of the 1DOCP model for arbitrary $f \in (0,1]$. We present the solutions in different regions for $1/2 \leq f \leq 1$ and $0 < f < 1/2$ separately.

A.4.1 The saddle point calculation for $1/2 \leq f \leq 1$:

The SPE for this case in the central region $[-\ell_N, \ell_N]$ is given in Eq. (A.13) whereas the SPEs on the left part $[-b_N, -l_N)$ and right part $(l_N, b_N]$ are given in Eqs.(A.14) and (A.15) respectively with $V(x) = -|x|$. From numerical results in Fig. 3.2, we observe that both the length scales ℓ_N and b_N are $\sim \mathcal{O}(N)$ and the equilibrium density indeed has the scaling form $\varrho_N(x) = \frac{1}{N}\tilde{\varrho}_f\left(\frac{x}{N}\right)$. Hence it is natural to work in the scaling variable $y = x/N$ and with the scaled density profile $\tilde{\varrho}_f(y)$. The SPE in the central regime can be written as

$$\begin{aligned}
&\frac{y^2}{2}-\int_{-\tilde{b}}^{\tilde{b}}|y'-y|\ \tilde{\varrho}_f(y')\ dy' \\
&\quad+\frac{1}{2}\Big[\int_{-\tilde{b}}^{-\tilde{\ell}}\bar{\delta}_{y'}\ \tilde{\varrho}_f(y')\ dy'+\int_{\tilde{\ell}}^{\tilde{b}}\delta_{y'}\tilde{\varrho}_f(y')\ dy'\Big]=\tilde{\mu}_1,
\end{aligned} \tag{A.21}$$

where $y = x/N$, $\tilde{b} = b_N/N$, $\tilde{\ell} = \ell_N/N$ and $\tilde{\mu}_1 = \mu_1/N^3$. The SPE on the left edge part can be written in terms of the scaled quantities as

$$\frac{y^2}{2} - \int_{-\tilde{b}}^{\tilde{b}} |y' - y|\ \tilde{\varrho}_f(y')\ dy' + \frac{1}{2}\left(2\int_{y+\bar{\delta}_y}^{\tilde{b}} |y' - y|\tilde{\varrho}_f(y')\ dy' + \int_{-\tilde{b}}^{y} \bar{\delta}_{y'}\tilde{\varrho}_f(y')\ dy' + \int_{\tilde{\ell}}^{y+\bar{\delta}_y} \delta_{y'}\tilde{\varrho}_f(y')\ dy'\right) = \tilde{\mu}_2. \quad \text{(A.22)}$$

where $\tilde{\mu}_2 = \mu_2/N^3$. A similar equation can be written for the right edge part as well. Note that in writing the above equations we have assumed that the functions $\mathcal{D}_x$ and $\bar{\mathcal{D}}_x$ [defined in Eq. (A.8)] have scaling forms $\bar{\mathcal{D}}_{x=Ny} = N\bar{\delta}_y$ and $\mathcal{D}_{x=Ny} = N\delta_y$, respectively.

From Fig. 3.2 we further observe that the scaled density profile is piece-wise uniform. This leads us to make the following ansatz for the scaled density profile as

$$\tilde{\varrho}_f(y) = \begin{cases} \tilde{\varrho}_{\text{edge}} \text{ for } -\tilde{b} \le y < -\tilde{\ell} \\ \tilde{\varrho}_{\text{mid}} \text{ for } -\tilde{\ell} \le y \le \tilde{\ell} \\ \tilde{\varrho}_{\text{edge}} \text{ for } \tilde{\ell} < y \le \tilde{b}. \end{cases} \quad \text{(A.23)}$$

Our next task is to express the SPEs in terms of the above ansatz for $\tilde{\varrho}_f(y)$ and solve for the six unknown constants $\tilde{\varrho}_{\text{mid}}$, $\tilde{\varrho}_{\text{edge}}$, $\tilde{\ell}$, $\tilde{b}$, $\tilde{\mu}_1$ and $\tilde{\mu}_2$. To proceed further, we first need to determine the y dependence of the functions δ_y and $\bar{\delta}_y$. Recall that these functions determine the lengths, starting from y, one needs to cover on the left or right to find f fraction of particles. They are defined as

$$\int_{y-\delta_y}^{y} \tilde{\varrho}_f(y')dy' = \int_{y}^{y+\bar{\delta}_y} \tilde{\varrho}_f(y')dy' = f. \quad \text{(A.24)}$$

Note these equations are scaled versions of Eq. (A.8). For the particle at $y' = -\tilde{b}$, the distance $\bar{\delta}_{y'}$ is $(\tilde{\ell} + \tilde{b})$ since exactly f fraction of total particles are present inside $[-\tilde{b}, \tilde{\ell}]$ and the remaining $(1-f)$ fraction of particles stay inside $(\tilde{\ell}, \tilde{b}]$. As the equilibrium density is equal to $\tilde{\varrho}_{\text{edge}}$ both in the left part $[-\tilde{b}, -\tilde{\ell})$ and in the right part $(\tilde{\ell}, \tilde{b}]$, the distance $\bar{\delta}_{y'}$ for any $y' \in [-\tilde{b}, -\tilde{\ell}]$ is exactly equal to $(\tilde{\ell} + \tilde{b})$. Similar arguments hold for $\delta_{y'}$ when $y' \in [\tilde{\ell}, \tilde{b}]$. As a result $\delta_{y'}$ for any $y' \in [\tilde{\ell}, \tilde{b}]$ is also equal to $(\tilde{\ell} + \tilde{b})$. The function δ_y is

defined only over the domain $[\tilde{\ell}, \tilde{b}]$ and $\bar{\delta}_y$ over $[-\tilde{b}, -\tilde{\ell}]$. They have the following explicit forms

$$\begin{aligned} \bar{\delta}_y &= (\tilde{b} + \tilde{\ell}) \quad \text{for } -\tilde{b} \leq y \leq -\tilde{\ell} \\ \delta_y &= (\tilde{b} + \tilde{\ell}) \quad \text{for } \tilde{\ell} \leq y \leq \tilde{b}. \end{aligned} \tag{A.25}$$

Inserting the form of $\tilde{\varrho}_f(y)$ from Eq. (A.23) and the forms of δ_y and $\bar{\delta}_y$ from Eq. (A.25) in the SPE (A.21), and performing the integrals one finds

$$\Big(\frac{1}{2} - \tilde{\varrho}_{\text{mid}}\Big) y^2 - \tilde{\varrho}_{\text{mid}} \tilde{\ell}^2 = \tilde{\mu}_1, \quad \text{for} \quad -\tilde{\ell} \leq y \leq \tilde{\ell}. \tag{A.26}$$

Since this equation is valid for all $-\tilde{\ell} \leq y \leq \tilde{\ell}$, the coefficients of all the powers of y must vanish individually, which in turn implies

$$\tilde{\varrho}_{\text{mid}} = \frac{1}{2}, \ \tilde{\ell} = (2f - 1) \text{ and } \tilde{\mu}_1 = -\tilde{\varrho}_{\text{mid}} \tilde{\ell}^2. \tag{A.27}$$

We now focus on solving the SPEs on the edges. We start with the SPE on the left edge part given in Eq. (A.22), where once again we insert the ansatz for $\tilde{\varrho}_f(y)$ from Eq. (A.23) and the forms of δ_y and $\bar{\delta}_y$ from Eq. (A.25). After performing the integrals we get

$$\Big(1 - \tilde{\varrho}_{\text{edge}}\Big) \frac{y^2}{2} + 2\tilde{\ell} \left(\tilde{\varrho}_{\text{mid}} - \frac{\tilde{\varrho}_{\text{edge}}}{2} \right) y - \tilde{\varrho}_{\text{edge}} \frac{\tilde{\ell}^2}{2} = \tilde{\mu}_2. \tag{A.28}$$

This equation is valid for any $y \in [-\tilde{b}, -\tilde{\ell})$. Consequently, the coefficients of all the powers of y must vanish individually which provides

$$\tilde{\varrho}_{\text{edge}} = 1, \ \tilde{\varrho}_{\text{mid}} = \frac{\tilde{\varrho}_{\text{edge}}}{2} = \frac{1}{2} \text{ and } \tilde{\mu}_2 = -\tilde{\varrho}_{\text{mid}} \tilde{\ell}^2. \tag{A.29}$$

From Eq. (A.27) and Eq. (A.29) we notice $\tilde{\mu}_1 = \tilde{\mu}_2$. One can perform a similar calculation for the right part and find exactly the same expressions for the constants as in Eq. (A.29). Combining Eqs. (A.27) and (A.29) we get the values of all the constants appearing in Eq. (A.23)

$$\tilde{\varrho}_{\text{edge}} = 1, \quad \tilde{\varrho}_{\text{mid}} = \frac{1}{2}, \quad \tilde{b} = f, \quad \tilde{\ell} = (2f - 1), \tag{A.30}$$

and thus completely specify the scaled density profile $\tilde{\varrho}_f(y)$ defined in Eq. (A.23).

A.4.2 The saddle point calculation for $0 < f < 1/2$:

In this case, there are $(1-2f)$ fraction of particles in the central region and f fractions of particles on either side of it in equilibrium. The SPEs in all three regions, center, left and right, can be read off from Eqs. (A.18- A.20) with $V(x) = -|x|$. One can rewrite these equations in terms of the scaled variable $y = x/N$ which will turn out to be convenient as shown below. As discussed in Sec. 3.3.1 (see Eq. (3.20)), we expect that for $0 < f < 1/2$ the saddle point (scaled) density profile should have the following form:

$$\tilde{\varrho}_f(y) = (1-2f)\delta(y) + \tilde{\varrho}_{\rm edge}\mathbb{1}_{[-\tilde{b},\tilde{b}]}(y). \tag{A.31}$$

Our task is to find the density value $\tilde{\varrho}_{\rm edge}$ and the size $\tilde{b}$ of the support. For that we first rewrite the SPE from Eq. (A.18) in terms of scaling variable $y = x/N$ on the left part $-\tilde{b} \le y < 0_-$:

$$\begin{aligned}\frac{y^2}{2} \underbrace{- \int_{-\tilde{b}}^{0_-} |y-y'|\tilde{\varrho}_f(y')dy'}_{T_2} \quad \underbrace{- \int_{0_-}^{y+\bar{\delta}_y} (y'-y)\tilde{\varrho}_f(y')dy'}_{T_3} \\ + \underbrace{\frac{1}{2}\int_{-\tilde{b}}^{y} \bar{\delta}_{y'}\tilde{\varrho}_f(y')dy'}_{T_4} + \underbrace{\frac{1}{2}\int_{0_-}^{y+\bar{\delta}_y} \delta_{y'}\tilde{\varrho}_f(y')dy'}_{T_5} - \tilde{\mu}_2 = 0.\end{aligned} \tag{A.32}$$

Note, while writing the above saddle point equation we have assumed that $\tilde{\ell} = \ell_N/N \to 0$ as $N \to \infty$. We will later show that $\ell_N \sim \sqrt{\log N}$ [see Eq. (3.30)] and for the time being we assume $\tilde{\ell} \to 0$ and proceed. Also note that we have assumed that the functions $\bar{\mathcal{D}}_x$ and $\mathcal{D}_x$ have the following scaling $\bar{\mathcal{D}}_{x=yN} = N\bar{\delta}_y$ and $\mathcal{D}_{x=yN} = N\delta_y$. Explicit forms of these functions will be determined later.

The next task is to insert the ansatz from Eq. (A.31) for the scaled density profile in Eq. (A.32), and evaluate different integrals in this equation. The second term in the

L.H.S. of Eq. (A.32) can be evaluated easily and one finds

$$T_2 = -\int_{-\tilde{b}}^{0-} |y - y'|\tilde{\varrho}_f(y')dy' = -\tilde{\varrho}_{\rm edge}\Big[y^2 + y\tilde{b} + \frac{\tilde{b}^2}{2}\Big]. \tag{A.33}$$

To evaluate the other terms we first need to find the y dependence of δ_y and $\bar{\delta}_y$. It turns out that the y dependence of $\bar{\delta}_y$ and δ_y are different for $1/3 \leq f < 1/2$ and $0 < f < 1/3$. This happens because for $1/3 \leq f < 1/2$, the fraction of particles $(1-2f)$ in the central region is smaller than the fraction f of particles on either edge part, whereas for $0 < f < 1/3$, the fraction in the central part is larger than f. Hence, from this point, one requires to consider the two cases separately.

$1/3 \leq f < 1/2$:

In order to determine y dependence of δ_y and $\bar{\delta}_y$, we first need to investigate the x dependence of $\mathcal{D}_x$ and $\bar{\mathcal{D}}_x$. As shown in Fig. 3.3(b), the density profile in the central part can be described by a Gaussian distribution function of the unscaled variable x. On the other hand from Fig. 3.3(a), we observe that the density profile outside the central part is constant and to be consistent with the ansatz for the scaled profile in Eq. (A.31), the value of the constant should be $\frac{\tilde{\varrho}_{\rm edge}}{N}$. It is easy to see that for $x = -b_N$ one has to move to point $x = -\ell_N$ *i.e.* by a distance $\bar{\mathcal{D}}_{-b_N} = b_N - \ell_N$ on the right to find f fraction of particles. Now if we start from a point x slightly above $x = -b_N$, one has to reach a point $\bar{X}(x) = x + \bar{\mathcal{D}}_x$ inside the central region $[-\ell_N, \ell_N]$ in order to find f fraction of particles on the right. As the point x moves towards right starting from $x = -b_N$, the image point $\bar{X}(x)$ also moves towards right and for $1/3 \leq f < 1/2$ there will be a point $x = -x_f$ for which the image point will touch the right boundary of the central region *i.e.* $\bar{X}(-x_f) = \ell_N$. It is easy to see that for $-b_N \leq x < -x_f$, $\bar{X}(x)$ can be obtained by solving

$$\int_{-\ell_N}^{\bar{X}(x)} \rho_{\rm central}(x')dx' = (b_N + x)\frac{\tilde{\varrho}_{\rm edge}}{N}, \tag{A.34}$$

where $\rho_{\rm central}(x)$ is density profile in the central part described by a Gaussian function as shown in Fig. 3.3(b) [see Eq. (3.19) and Eq. (3.27)]. Since the central region contains $(1-2f)$ fraction of particles, $|\bar{X}(x)| < \ell_N$ for $-b_N \leq x < -x_f$ and $\bar{X}(-x_f) = \ell_N$. Hence,

one finds the following expression for x_f

$$x_f = \frac{(3f-1)N}{\tilde{\varrho}_{\rm edge}} + \ell_N. \tag{A.35}$$

Now as the point x moves further right of $-x_f$, the corresponding image point $\bar{X}(x)$ enters the right edge region where the density profile is again uniform with value $\frac{\tilde{\varrho}_{\rm edge}}{N}$. So it becomes straightforward to show that $\bar{\mathcal{D}}_x = x_f + \ell_N$ *i.e.* independent of x for $-x_f \le x < -\ell_N$. Now as x enters the region $[-\ell_N, \ell_N]$, we expect $\bar{\mathcal{D}}_x$ should again start depending on x and should change rapidly by large amount over a small distance $2l_N$ such that $\bar{X}(\ell_N) = b_N$, the rightmost point of the support of the full density profile. Performing a similar estimate as done for the range $-b_N \le x < -x_f$, one can show that $\bar{\mathcal{D}}_x = x_f + \frac{N}{\tilde{\varrho}_{\rm edge}} \int_{-\ell}^{x} \rho_{\rm central}(x')dx' - x$ for $-\ell_N \le x \le \ell_N$. Collecting the functional forms of $\bar{\mathcal{D}}_x$ from different regions we, for $1/3 \le f < 1/2$, have

$$\bar{\mathcal{D}}_x = \begin{cases} \bar{X}(x) - x & \text{for} \quad -b_N \le x \le -x_f \\ x_f + \ell_N & \text{for} \quad -x_f \le x \le -\ell_N \\ x_f + \frac{N}{\tilde{\varrho}_{\rm edge}} \int_{-\ell_N}^{x} \rho_{\rm central}(x')dx' - x & \text{for} \quad -\ell_N \le x \le \ell_N, \end{cases} \tag{A.36}$$

where x_f is given in Eq. (A.35) and $\bar{X}(x)$ is determined from the solution of Eq. (A.34). In the large N limit the length function $\bar{\mathcal{D}}_x$ can be written in terms of the scaling variable $y = x/N$ as $\bar{\mathcal{D}}_{x=Ny} = N\bar{\delta}_y$ where

$$\bar{\delta}_y = \begin{cases} -y & \text{for} \quad -\tilde{b} \le y \le -\tilde{x}_f \\ \tilde{x}_f & \text{for} \quad -\tilde{x}_f \le y \le 0_- \\ \tilde{b} & \text{for} \quad y = 0_+, \end{cases} \tag{A.37}$$

with

$$\tilde{x}_f = \frac{x_f}{N} = \frac{(3f-1)}{\tilde{\varrho}_{\rm edge}} \quad \text{for } \frac{1}{3} \le f < \frac{1}{2}. \tag{A.38}$$

One can perform a similar analysis to find the y dependence of δ_y. Using the fact that the saddle point density profile should be symmetric about the origin (center of the trap),

one can write

$$\delta_y = \begin{cases} y & \text{for } \tilde{x}_f \le y \le \tilde{b} \\ \tilde{x}_f & \text{for } 0_+ \le y \le \tilde{x}_f \\ \tilde{b} & \text{for } \quad y = 0_-. \end{cases} \tag{A.39}$$

Now we are in a position to evaluate the 3rd, 4th and 5th terms on the L.H.S. of Eq. (A.32). We now insert the ansatz for the density profile from Eq. (A.31) and, $\bar{\delta}_y$ and δ_y from Eqs. (A.37, A.39), respectively, in the expressions of these terms and perform the integrals. Since y dependence of $\bar{\delta}_y$ is different in different ranges of y, one needs to evaluate the integrals for y falling in different ranges separately. We first focus on the third term T_3 for $-\tilde{b} \le y \le -\tilde{x}_f$, in Eq. (A.32). To evaluate this term, we first note that for $-\tilde{b} \le y \le -\tilde{x}_f$, the image point $\bar{Y}(y) = y + \bar{\delta}_y$ satisfies $0_- < \bar{Y}(y) < 0_+$ (which in terms of unscaled variable reads $-\ell_N < \bar{X}(x) < \ell_N$. Hence we put $y' = 0$ in the integrand and approximate T_3 as $T_3 \approx y \int_{0_-}^{y+\bar{\delta}_y} \tilde{\varrho}_f(y')dy'$. Note that, the integral $\int_{0_-}^{y+\bar{\delta}_y} \tilde{\varrho}_f(y')dy'$ represents exactly the same fraction of particles inside the region $[-\tilde{b}, y]$. This is because one has to acquire the same fraction of particles that one loses when one moves from $-\tilde{b}$ to y $(< -\tilde{x}_f)$ so that one finds f fraction of particles between y to $y + \bar{\delta}_y$. For $-\tilde{x}_f \le y < 0_-$, it is straightforward to evaluate the integral T_3. One can evaluate the integral T_4 in the two different ranges of y also separately and once again straightforwardly. One finally has

$$T_3 = \begin{cases} y(\tilde{b} + y)\tilde{\varrho}_{edge} & \text{for } \quad -\tilde{b} \le y \le -\tilde{x}_f \\ y(1-2f) - \tilde{\varrho}_{\rm edge}\Big[\frac{(y+\tilde{x}_f)^2}{2} - y(y+\tilde{x}_f)\Big] & \text{for } \quad -\tilde{x}_f \le y < 0_-, \end{cases} \tag{A.40}$$

$$T_4 = \begin{cases} \frac{\tilde{\varrho}_{\rm edge}}{4}\big(\tilde{b}^2 - y^2\big) & \text{for } \quad -\tilde{b} \le y \le -\tilde{x}_f \\ \frac{\tilde{\varrho}_{\rm edge}}{4}\big(\tilde{b}^2 - \tilde{x}_f^2\big) + \frac{\tilde{x}_f \tilde{\varrho}_{\rm edge}}{2}\big(y + \tilde{x}_f\big), & \text{for } \quad -\tilde{x}_f \le y < 0_-, \end{cases} \tag{A.41}$$

To compute the fifth term T_5 in Eq. (A.32) one needs to be careful and we discuss the computation for the two ranges $-\tilde{b} \le y \le -\tilde{x}_f$ and $-\tilde{x}_f \le y < 0_-$ separately. We first

focus on the first regime, in which the integral is

$$T_5 = \frac{1}{2}\int_{0_-}^{\bar{Y}(y)} \delta_{y'}\tilde{\varrho}_f(y')dy', \tag{A.42}$$

where $\bar{Y}(y) = y + \bar{\delta}_y < 0_+$. Although the range of the integral $[0_-, \bar{Y}(y)]$ is very small (in fact infinitesimal), the integral would produce a finite contribution because the (scaled) density profile in this range is a delta function and the function $\bar{\delta}_y$ changes rapidly by a large amount which, in fact, appears to be a discontinuous change in the $N \to \infty$ limit. In order to find the contribution of the integral we rewrite the integral T_5 in terms of the unscaled variables as

$$T_5 = \frac{1}{2N}\int_{-\ell_N}^{\bar{X}(x)} \mathcal{D}_{x'}\rho_{\rm central}(x')dx'. \tag{A.43}$$

Recall that for large N, there are $(1-2f)N$ particles in the central part out of which $n = \tilde{\varrho}_{\rm edge}(b_N + x)$ particles stay inside $[-\ell_N, \bar{X}(x)]$. In terms of the microscopic positions of these particles, the integral in Eq. (A.43) can be written as

$$T_5 = \frac{1}{2N}\int_{-\ell_N}^{\bar{X}(x)} \mathcal{D}_{x'}\frac{1}{N}\left\langle \sum_{i=1}^{N}\delta(x'-x_i)\right\rangle_{\rm eq} dx' = \frac{1}{2N^2}\sum_{i=fN+1}^{fN+n}\langle \mathcal{D}_{x_i}\rangle_{\rm eq}\,. \tag{A.44}$$

It is easy to see that for the left-most particle inside the central region $[-\ell_N, \ell_N]$ labeled by $i = fN+1$, the distance $\langle \mathcal{D}_{x_i}\rangle_{\rm eq} \approx b_N$ since exactly f fraction of particles are present inside the left edge region $[-b_N, -\ell_N)$. For the next particle labeled by $i = fN+2$, the distance $\langle \mathcal{D}_{x_i}\rangle_{\rm eq} \approx (b_N - \bar{d})$ with $\bar{d} = 1/(N\rho_{\rm edge}) = \frac{1}{\tilde{\varrho}_{\rm edge}}$. Since the density inside $[-b_N, -\ell_N)$ is uniform $\rho_{\rm edge}$, the equilibrium separation between two consecutive particles inside $[-b_N, -\ell_N)$ is $\bar{d}$. Hence for a particle labeled by $i \in [fN+1, fN+n]$ with $n = \tilde{\varrho}_{\rm edge}(b_N + x)$, the distance $\langle \mathcal{D}_{x_i}\rangle_{\rm eq} \approx b_N - (i - fN - 1)\bar{d}$. Putting this form in Eq. (A.44) and performing the summation one finds

$$T_5 \approx \frac{1}{2N^2}\sum_{j=0}^{n-1}(b - j\ \bar{d}) \approx \frac{1}{4}\tilde{\varrho}_{\rm edge}(\tilde{b}^2 - y^2) \quad \text{for} \quad -\tilde{b} \le y \le -\tilde{x}_f. \tag{A.45}$$

We now evaluate the 5^{th} integral T_5 in Eq. (A.32) for $-\tilde{x}_f \le y < 0_-$. For y in this range, one finds $0_+ \le \bar{Y}(y) < \tilde{x}_f$. Hence we decompose the integral as

$$T_5 = \underbrace{\frac{1}{2}\int_{0_-}^{0_+} \delta_{y'}\tilde{\varrho}_f(y')dy'}_{T_{51}} + \underbrace{\frac{1}{2}\int_{0_+}^{\bar{Y}(y)} \delta_{y'}\tilde{\varrho}_f(y')dy'}_{T_{52}}. \tag{A.46}$$

Note that the first term in the above equation, denoted by T_{51}, has the same form as the integral in Eq. (A.42) except that now the upper limit is 0_+. As done for the integral in Eq. (A.42), the integral in Eq. (A.46) once again can be expressed in terms of the unscaled variables as

$$T_{51} = \frac{1}{2N}\int_{-\ell_N}^{\ell_N} \mathcal{D}_{x'}\ \rho(x')dx' = \frac{1}{2N}\int_{-\ell_N}^{\ell_N} \mathcal{D}_{x'}\ \rho_{\text{central}}(x')dx'. \tag{A.47}$$

which can again be evaluated as

$$T_{51} = \frac{1}{2N}\int_{-\ell_N}^{\ell_N} \mathcal{D}_{x'}\frac{1}{N}\left\langle \sum_{i=1}^{N}\delta(x'-x_i)\right\rangle_{\text{eq}} dx' = \frac{1}{2N^2}\sum_{i=fN+1}^{(1-f)N}\langle \mathcal{D}_{x_i}\rangle_{\text{eq}}\,, \tag{A.48}$$

where for a particle labeled by $i \in [fN+1,(1-f)N]$, the distance $\langle \mathcal{D}_{x_i}\rangle \approx b_N - (i - fN - 1)\bar{d}$. Putting this form in Eq. (A.48) and performing the summation one finds

$$T_{51} \approx \frac{1}{2N^2}\sum_{j=0}^{(1-2f)N-1}(b - j\ \bar{d}) = \frac{1}{2}(1-2f)\Big[\tilde{b} - \frac{\bar{d}}{2}(1-2f)\Big]. \tag{A.49}$$

We now have to evaluate the remaining term T_{52} on the R.H.S. of Eq (A.46). We first note that for $-\tilde{x}_f \le y < 0_-$, the image point lies within $0_+ \le \bar{Y}(y) < \tilde{x}_f$ and from Eq. (A.39) we observe that $\delta_y = \tilde{x}_f$. Putting this form of δ_y and $\tilde{\varrho}_f(y) = \tilde{\varrho}_{\text{edge}}$ inside the integral T_{52} in Eq. (A.46) and performing the integral, we get

$$T_{52} = \frac{1}{2}\tilde{\varrho}_{\text{edge}}\tilde{x}_f(y+\tilde{x}_f). \tag{A.50}$$

Hence, collecting the results from Eqs. (A.45), (A.49) and (A.50), we finally have

$$T_5 = \begin{cases} \frac{1}{4}\tilde{\varrho}_{\rm edge}(y+\tilde{b})(\tilde{b}-y) & \text{for } -\tilde{b} \le y \le -\tilde{x}_f, \\ \frac{1}{2}(1-2f)\Big[\tilde{b} - \frac{(1-2f)}{2\tilde{\varrho}_{\rm edge}}\Big] + \frac{1}{2}\tilde{\varrho}_{\rm edge}\tilde{x}_f(y+\tilde{x}_f), & \text{for } -\tilde{x}_f \le y < 0_-. \end{cases} \tag{A.51}$$

Now we have values of all the integrals in Eq. (A.32). Putting the expressions of the integrals from Eqs. (A.33), (A.40),(A.41),(A.51), we rewrite Eq. (A.32) as

$$\begin{aligned} \Big(1-\tilde{\varrho}_{\rm edge}\Big)\frac{y^2}{2} &\approx \tilde{\mu}_2, && \text{for } -\tilde{b} \le y \le -\tilde{x}_f, \\ (\ \ 1-\tilde{\varrho}_{\rm edge})\frac{y^2}{2} + \tilde{\varrho}_{\rm edge}\Big(\frac{f}{\tilde{\varrho}_{\rm edge}} - \tilde{b}\Big)y - \frac{\tilde{\varrho}_{\rm edge}}{4} & \Big[\tilde{b}^2 - \Big(\frac{3f-1}{\tilde{\varrho}_{\rm edge}}\Big)^2\Big] \\ + \frac{1}{2}(1-2f)\Big[\tilde{b} - \frac{(1-2f)}{2\tilde{\varrho}_{\rm edge}}\Big] &\approx \tilde{\mu}_2, && \text{for } -\tilde{x}_f \le y < 0_-. \end{aligned} \tag{A.52}$$

Equating coefficients of different powers of y to zero individually in both the regions of y and solving the resulting equations, we find

$$\tilde{\varrho}_{\rm edge} = 1, \quad \tilde{b} = Jf \quad \text{and} \quad \tilde{\mu}_2 = 0, \tag{A.53}$$

as announced in Eq. (3.25). Following a similar procedure, it is straightforward to check that one would get the same solution for $\tilde{\varrho}_f(y)$ if one solves the saddle point equation in the right part ($0^+ < y \le \tilde{b}$). We thus get the full solution of the scaled density profile $\tilde{\varrho}_f(y)$ given in Eq. (A.31).

$0 < f < 1/3$:

Having discussed the saddle point calculation for $1/3 \le f < 1/2$, we now move to the $0 < f < 1/3$ case. To find $\bar{\mathcal{D}}_x$ one can follow a similar analysis as done in Eq. (A.36) and get

$$\bar{\mathcal{D}}_x = \begin{cases} \bar{X}(x) - x & \text{for } \ -b_N \le x \le x_f^* \\ \ell_N + \frac{N}{\tilde{\varrho}_{\rm edge}}\int_{x_f^*}^{x} \rho_{\rm central}(x')dx' - x & \text{for } \ x_f^* < x \le \ell_N, \end{cases} \tag{A.54}$$

where x_f^* is the special position such that it's image point $\bar{X}(x_f^*)$ on right is equal to ℓ_N. It is easy to see that $\bar{X}(x)$ satisfies

$$\int_{\max(x,-\ell_N)}^{\bar{X}(x)} \rho_{\rm central}(x')dx' = \frac{[b_N + \min(x, -\ell_N)]\tilde{\varrho}_{\rm edge}}{N}. \tag{A.55}$$

From the above equation, one finds that x_f^* should satisfy

$$\int_0^{x_f^*} \rho_{\rm central}(x')dx' = \frac{1-4f}{2}, \tag{A.56}$$

from which it is easy to see that $|x_f^*| < \ell_N$ for $0 < f < 1/3$. Also note that for $-b_N \le x \le x_f^*$, the image point $\bar{X}(x)$ falls in the range $[-\ell_N, \ell_N]$ *i.e.* $|\bar{X}(x)| \le \ell_N$. Additionally, using the definition of x_f^* from Eq. (A.56) in Eq. (A.54), one can see that $\bar{\mathcal{D}}_x \to (b_N - \ell_N)$ as $x \to \ell_N$. Hence, it is easy to see that for large N, $\bar{\mathcal{D}}_x$ behaves as $\bar{\mathcal{D}}_x = N\bar{\delta}_{x/N}$ where

$$\bar{\delta}_y = \begin{cases} -y & \text{for} \quad -\tilde{b} \le y < 0_- \\ \tilde{b} & \text{for} \quad y = 0_+. \end{cases} \tag{A.57}$$

Note the y dependence of $\bar{\delta}_y$ for $0 < f < 1/3$ is same as $\bar{\delta}_y$ for $1/3 \le f < 1/2$ given in Eq. (A.37) with $\tilde{x}_f = 0$. Hence, the analysis of the SPE (A.32) is almost same as for the $1/3 < f < 1/2$ case with $\tilde{x}_f = 0$. Hence the calculations for T_3, T_4 and T_5 in the range $\tilde{b} \le y \le -\tilde{x}_f$ for the previous case ($1/3 \le f < 1/2$) would go through and the expressions of these terms for $0 < f < 1/3$ can be easily obtained by putting $\tilde{x}_f = 0$ in the expressions of these integrals. Hence, for $0 < f < 1/3$ the SPE (A.32) gets simplified to

$$(1 - \tilde{\varrho}_{\rm edge})\frac{y^2}{2} \approx \tilde{\mu}_2, \tag{A.58}$$

which once again implies $\tilde{\varrho}_{\rm edge} = 1$, and $\tilde{\mu}_2 \approx 0$. The value for $\tilde{b}$ can be determined from the normalisation $\int_{-\tilde{b}}^{0_-} \tilde{\varrho}_f(y)dy = f$ and it yields $\tilde{b} \approx f$ as in Eq. (A.53). One can follow the same procedure to solve the saddle point equation on the right part and arrive at the same solution for $\tilde{\varrho}_f(y)$.

A.5 Crossover in the density profiles in Riesz gas models for other values of k

In chapter 3, we explored the crossovers in the density profiles for FR 1DOCP and log-gas, which correspond to the FR Riesz gas with $k = -1$ and $k = 0^+$ respectively. For other values of $k > -2$ in Eq. (3.1), we observe similar crossovers in the density profile with respect to f as observed for the 1DOCP and log-gas models. In this section, we briefly demonstrate such crossover. Based on the behavior of the density profiles due to the variation in f, one can categorize them into three k regimes.

(i) $k > 1$: In this case, we find that for any fixed $f \in (0, 1]$ the density profile for large N remains same as in the ATAC ($f = 1$) case. The density profile posses the same scaling form $\varrho_N(x) = (1/N^{\alpha_k})\tilde{\varrho}_f(x/N^{\alpha_k})$ with $\alpha_k = k/(k + 2)$ and does not depend on f. This happens because for $k > 1$, the free energy functional $\Psi[\rho_N(x)]$ (in leading order in N) is local as the dominant contribution comes from the self energy contribution. In Fig. A.1(a), we plot the scaled density profile for this case that is obtained numerically.

(ii) $0 < k < 1$: In this range of models, the ATAC case ($f = 1$) was studied in Ref. [97] and the SR case ($f = 0$) was studied in Ref. [99]. In these studies, it was observed that in both the limits of f, the equilibrium density profile is finitely supported and possesses the same scaling form $\varrho_N(x) = (1/N^{\alpha_k})\tilde{\varrho}_f(x/N^{\alpha_k})$ as in the $k > 1$ case. However, in this case the exponent α_k takes different values for $f = 1$ and $f = 0$ [97, 99]. Consequently, the shape of the density profile differs. We numerically observe from Fig. A.1(b) that with decreasing f from one, the density profile seems to smoothly change from the ATAC profile to the SR profile.

(iii) $-2 < k < 0$: Unlike the previous cases, in this range of k, we observe that the density profile undergoes a drastic change of shape as f is reduced from 1 to 0. Crossover in the density profiles in this case is demonstrated in Fig. A.1(c) and Fig. A.1(d). For $-1 < k \leq 0$, the structural shift in the density profile takes place through a transition from a dome-shaped profile at $f = 1$ to a bell-shaped profile in the $f \to 0$ limit (see Fig. A.1(c)). The particular case of log-gas ($k \to 0$) falls in this regime which has been studied in detail in Sec. 3.4. For $-2 < k < -1$, the crossover in density profile, shown in Fig. A.1(d), is qualitatively similar to the 1DOCP ($k = -1$) case discussed in Sec. 3.3

of the main text. In the ATAC limit ($f = 1$), the density profile has a shape of 'U' with integrable divergences at the edges. As f is decreased from 1, two narrow density profiles with density values higher than that of the central part appear at the edges. The edge parts approach each other with decreasing f further until they touch each other at the center of the trap at $f = 1/2$. When f is decreased further, a fraction of particles gets accumulated at the center of the trap and the rest of the fraction pushed away creating two holes (regions deprived of particles) symmetrically placed on both sides of the central peak.

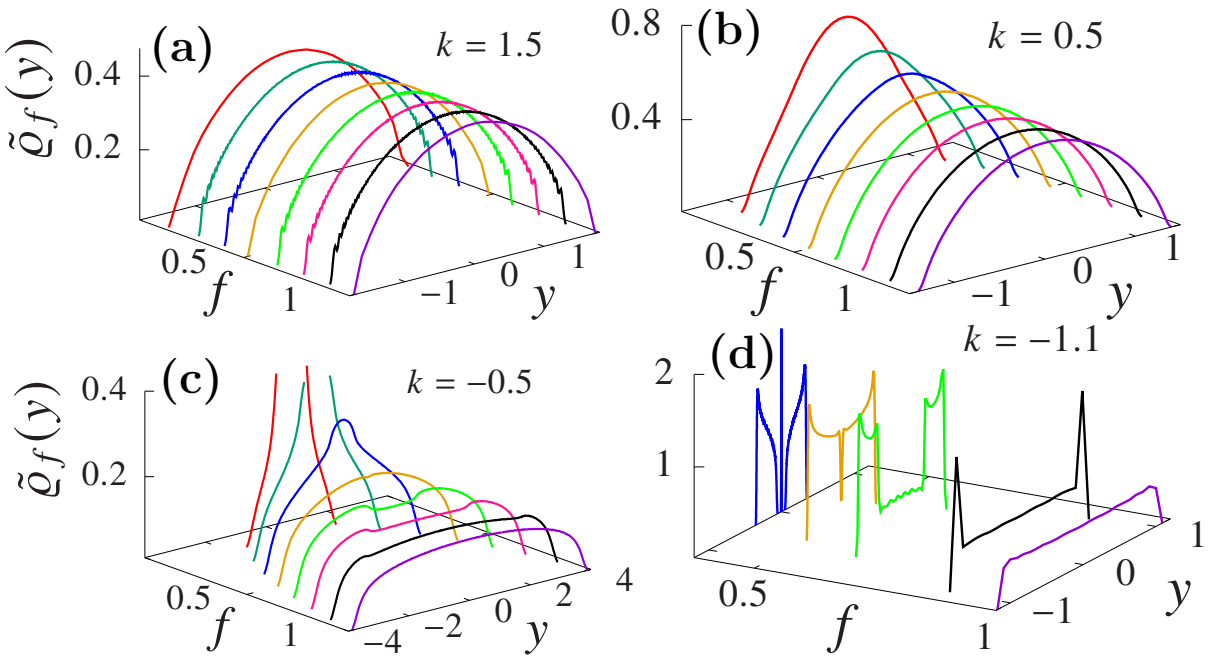

Figure A.1: This figure demonstrates how the density profiles change from one shape to another as f is reduced from 1 to 0 for four representative values of k: (a) $k = 1.5$, (b) $k = 0.5$, (c) $k = -0.5$ and (d)$k = -1.1$, chosen from the following ranges $k > 1$, $0 < k < 1$, $-1 < k < 0$ and $-2 < k < -1$. For each case except $k = -1.1$, we have plotted scaled density profiles $\varrho_f(y)$ for 8 values of f: $f = n/8$ with $n = 8, 7, ..., 1$ (from violet to red). To avoid congestion, for $k = -1.1$ we show density profiles only for five values of f corresponding to $n = 8, 7, 5, 4$ and 3 (from violet to blue). For $k = 1.5$ there is neither a change in the support nor in the shape. For $k = 0.5$, with decreasing f the repulsion among the particles reduces which causes them to gather near the centre of the trap. Consequently, the profile get squeezed from a dome shape at $f = 1$ to a hill shape at $f \to 0$. For $k = -0.5$, the equilibrium density profile changes drastically as compared to the previous two cases. The profile shows a crossover from a dome-shaped profile at $f \to 1$ limit to a bell-shaped profile at $f \to 0$. Near $f = 0$, the peaks of the bell-shaped profiles on the z-axis are cut in order to display the features of the density profiles for f close to 1. For $k = -1.1$, the density profile changes from a 'U' shaped profile at $f = 1$ to a bell-shaped profile at $f = 0$ passing through different other interesting shapes at intermediate values of f.

Bibliography

[1] R. K. Pathria and P. D. Beale, Statistical Mechanics (3rd ed.), Academic Press, 2011.

[2] M. Kardar, Statistical Physics of Particles, Cambridge University Press, 2007.

[3] C. J. Hood, T. W. Lynn, A. C. Doherty, A. S. Parkins and H. J. Kimble, The atom-cavity cicroscope: single atoms bound in orbit by single photons, Science, 287, 1447 (2000).

[4] W. S. Bakr, J. I. Gillen, A. Peng, S. Föolling and Markus Greiner, A quantum gas microscope for detecting single atoms in a Hubbard-regime optical lattice, Nature, 462, 74 (2009).

[5] M. L. Mehta, Random Matrices, 2nd ed., Academic Press, New York (1991).

[6] P. J. Forrester, Log-Gases and Random Matrices, Princeton University Press, Princeton, NJ (2010).

[7] M. V. Berry and M. Tabor, Level clustering in the regular spectrum, Proc. R. Soc. Lond. A. 356, 375 (1977).

[8] O. Bohigas, M. J. Giannoni and C. Schmit, Characterization of chaotic quantum spectra and universality of level fluctuation laws, Phys. Rev. Lett. 52, 1 (1984).

[9] F. M. Izrailev, Simple models of quantum chaos: Spectrum and eigenfunctions, Physics Reports, 196, 299 (1990).

[10] F. Haake, Quantum Signatures of Chaos, Springer Berlin, Heidelberg (2010).

[11] P. Bourgade, L. Erdos, H. Yau, Universality of general β-ensembles, Duke Math. J. 163, 1127 (2014).

[12] M. Riesz, Riemann Liouville integrals and potentials, Acta Sci. Math. 9, 1 (1938).

[13] M. Lewin, Coulomb and Riesz gases: The known and the unknown, J. Math. Phys. 63, 061101 (2022).

[14] D. J. Griffiths, Introduction to Electrodynamics (4th ed.), Pearson, 2013.

[15] A. Zangwill, Modern Electrodynamics, Cambridge University Press, 2013.

[16] A. Campa, T. Dauxois and S. Ruffo, Statistical mechanics and dynamics of solvable models with long-range interactions, Phys. Rep. 480, 57 (2009).

[17] F. Bouchet, S. Gupta and D. Mukamel, Thermodynamics and dynamics of systems with long-range interactions, 389, 4389 (2010).

[18] T. Padmanabhan, Statistical mechanics of gravitating systems, Phys. Rep. 188, 285 (1990).

[19] J. Miller, Statistical mechanics of Euler equations in two dimensions, Phys. Rev. Lett. 65, 2137 (1990).

[20] I. Ispolatov and E. G. D. Cohen, Phase transitions in systems with $1/r^{\alpha}$ attractive interactions, Phys. Rev. E 64, 056103 (2001).

[21] T. Dauxois, S. Ruffo, E. Arimondo and M. Wilkens, Dynamics and thermodynamics of systems with long-range interactions, Berlin, Heidelberg (2002).

[22] A. Campaa and A. Giansanti, Canonical and microcanonical partition functions in long-range systems with order parameter space of arbitrary dimension, Physica A. 340, 170 (2004).

[23] L. Casettia and M. Kastner, Partial equivalence of statistical ensembles and kinetic energy, Physica A. 384, 318 (2007).

[24] L. Casetti and C. Nardini, A solvable model of a self-gravitating system, J. Stat. Mech. 2010, P05006 (2010).

[25] A. Gabrielli, M. Joyce and B. Marcos, Quasistationary states and the range of pair interactions, Phys. Rev. Lett. 105, 210602 (2010).

[26] I. Latella and A. Pérez-Madrid, Local thermodynamics and the generalized Gibbs-Duhem equation in systems with long-range interactions, Phys. Rev. E 88, 042135 (2013).

[27] B. Marcos, Collisional relaxation of two-dimensional self-gravitating systems, Phys. Rev. E 88, 032112 (2013).

[28] A. Campa, T. Dauxois, D. Fanelli and S. Ruffo, Physics of Long-Range Interacting Systems, Oxford University Press, 2014.

[29] F. J. Dyson, Statistical theory of the energy levels of complex systems. I, J. Math. Phys. 3, 140 (1962).

[30] F. J. Dyson, Statistical theory of the energy levels of complex systems. II, J. Math. Phys. 3, 157 (1962).

[31] P. Forrester and J. B. Rogers, Electrostatics and the zeros of the classical polynomials J. Rogers, SIAM J. Math. Anal. 17(2), 461 (1986).

[32] E. P. Wigner, On the distribution of the roots of certain symmetric matrices, Annals of Mathematics, 67, 325 (1958).

[33] C. A. Tracy and H. Widom, Level-spacing distributions and the Airy kernel, Commun. Math. Phys. 159, 151 (1994).

[34] C. A. Tracy and H. Widom, On orthogonal and symplectic matrix ensembles, Commun. Math. Phys. 177, 727 (1996).

[35] D. S. Dean and S. N. Majumdar, Large deviations of extreme eigenvalues of random matrices, Phys. Rev. Lett. 97, 160201 (2006).

[36] D. S. Dean and S. N. Majumdar, Extreme value statistics of eigenvalues of Gaussian random matrices, Phys. Rev. E 77, 041108 (2008).

[37] S. N. Majumdar and G. Schehr, Top eigenvalue of a random matrix: large deviations and third order phase transition, J. Stat. Mech. 2014, P01012 (2014).

[38] S. N. Majumdar, C. Nadal, A. Scardicchio, and P. Vivo, Index distribution of Gaussian random matrices, Phys. Rev. Lett. 103, 220603 (2009).

[39] R. Marino, S. N. Majumdar, G. Schehr and P. Vivo, Phase transitions and edge scaling of number variance in Gaussian random matrices, Phys. Rev. Lett. 112, 254101 (2014).

[40] F. D. Cunden, P. Facchi, M. Ligabò and P. Vivo, Third-order phase transition: random matrices and screened Coulomb gas with hard walls, J. Stat. Phys. 175, 1262 (2019).

[41] F. D. Cunden, P. Facchi, M. Ligabò, and P. Vivo, Universality of the third-order phase transition in the constrained Coulomb gas, J. Stat. Mech. 2017, 053303 (2017).

[42] D. S. Dean, P. Le. Dousaal, S. N. Majumdar and G. Schehr, Noninteracting fermions at finite temperature in a d-dimensional trap: Universal correlations, Phys. Rev. A 94, 063622 (2016).

[43] D. S. Dean, P. Le. Dousaal, S. N. Majumdar and G. Schehr, Noninteracting fermions in a trap and random matrix theory, J. Phys. A: Math. Theor. 52, 144006 (2019).

[44] D. S. Dean, P. Le. Dousaal, S. N. Majumdar and G. Schehr, Nonequilibrium dynamics of noninteracting fermions in a trap, EPL, 126, 20006 (2019).

[45] P. Kazakopoulos and P. Mertikopoulos, A. L. Moustakas, G. Caire, Living at the edge: A large deviations approach to the outage MIMO capacity, IEEE Transactions on Information Theory, 57, 1984 (2011).

[46] M. R. Douglas, Large N gauge theory — Expansions and transitions, Nuclear Physics B - Proceedings Supplements, 41, 66 (1995).

[47] A. Lenard, Exact statistical mechanics of a one dimensional system with Coulomb forces, J. Math. Phys. 2, 682 (1961).

[48] R. J. Baxter, Statistical mechanics of a one-dimensional Coulomb system with a uniform charge background, Math. Proc. Camb. Phil. Soc. 59, 779 (1963).

[49] A. Dhar, A. Kundu, S. N. Majumdar, S. Sabhapandit and G. Schehr, Exact extremal statistics in the classical 1D Coulomb gas, Phys. Rev. Lett. 119, 060601 (2017).

[50] A. Dhar, A. Kundu, S. N. Majumdar, S. Sabhapandit and G. Schehr, Extreme statistics and index distribution in the classical 1d Coulomb gas, J. Phys. A: Math. Theor. 51, 295001 (2018).

[51] M. Baus and J. P. Hansen, Statistical mechanics of simple Coulomb systems, Physics Reports, 59(1), 1 (1980).

[52] P. Choquard, H. Kunz, P. A. Martin and M. Navet, One-dimensional Coulomb systems, In: Bernasconi J., Schneider T. (Eds) physics in one dimension, Springer Series in Solid-State Sciences, vol 23. Springer, Berlin, Heidelberg (1981).

[53] S. Prager, The one-dimensional plasma, Adv. Chem. Phys. 4, 201 (1962).

[54] D. S. Dean, R. R. Horgan, A. Naji and R. Podgornik, Effects of dielectric disorder on van der Waals interactions in slab geometries, Phys. Rev. E 81, 051117 (2010).

[55] G. Téllez and E. Trizac, Screening like charges in one-dimensional Coulomb systems: Exact results, Phys. Rev. E 92, 042134 (2015).

[56] A. Flack, and S. N. Majumdar and G. Schehr, Truncated linear statistics in the one dimensional one-component plasma, J. Phys. A: Math. Theor. 54, 435002 (2021).

[57] A. Flack, S. N. Majumdar and G. Schehr, Gap probability and full counting statistics in the one dimensional one-component plasma, J. Stat. Mech. 5, 053211 (2022).

[58] F. D. Cunden, P. Facchi, M. Ligab‘o and P. Vivo, Universality of the weak pushed-to-pulled transition in systems with repulsive interactions, J. Phys. A: Math. Theore. 51, 35LT01 (2018).

[59] F. Calogero, Solution of a three-body problem in one dimension, J. Math. Phys. 10, 2191 (1969).

[60] F. Calogero, Ground state of a one-dimensional N-body system, J. Math. Phys. 10, 2197 (1969).

[61] F. Calogero, Solution of the one-dimensional N-body problems with quadratic and/or inversely quadratic pair potentials, J. Math. Phys. 12, 419 (1971).

[62] B. Sutherland, Exact results for a quantum many-body problem in one dimension, Phys. Rev. A 4, 2019 (1971).

[63] B. Sutherland, Exact results for quantum many-body problem in one dimension. II, Phys. Rev. A 5, 1372 (1972).

[64] B. Sutherland, Exact ground-state wave function for a one-dimensional plasma Phys. Rev. Lett. 34, 1083 (1975).

[65] F. Calogero, Exactly solvable one-dimensional many body problems, Lett. Nuovo Cimento 13, 411 (1975).

[66] J. Moser, Three integrable Hamiltonian systems connected with isospectral deformations, Advances in Mathematics, 16, 197 (1975).

[67] E. Bogomolny, O. Giraud and C. Schmit, Random matrix ensembles associated with Lax matrices, Phys. Rev. Lett. 103, 054103 (2009).

[68] A. P. Polychronakos, The physics and mathematics of Calogero particles, J. Phys. A: Math. Theor. 39, 12793 (2006).

[69] J. A. Joseph, J. E. Thomas, M. Kulkarni and A. G. Abanov, Observation of shock waves in a strongly interacting Fermi gas, Phys. Rev. Lett. 106, 150401 (2011).

[70] M. Kulkarni and A. G. Abanov, Hydrodynamics of cold atomic gases in the limit of weak nonlinearity, dispersion, and dissipation, Phys. Rev. A 86, 033614 (2012).

[71] A. G. Abanov and P. B. Wiegmann, Quantum hydrodynamics, the quantum Benjamin-Ono equation, and the Calogero model, Phys. Rev. Lett. 95, 076402 (2005).

[72] M. Kulkarni and A. Polychronakos, Emergence of the Calogero family of models in external potentials: duality, solitons and hydrodynamics, J. Phys. A: Math. Theor. 50, 455202 (2017).

[73] A. G. Abanov, A. Gromov and M. Kulkarni, Soliton solutions of a Calogero model in a harmonic potential, J. Phys. A: Math. Theor. 44, 295203 (2011).

[74] S. B. Kiran, D. A. Huse and M. Kulkarni, Spatiotemporal spread of perturbations in power-law models at low temperatures: Exact results for classical out-of-time-order correlators, Phys. Rev. E 104, 044117 (2021).

[75] S. Agarwal, M. Kulkarni and A. Dhar, Some connections between the classical Calogero-Moser model and the log-gas, J. Stat. Phys. 176, 1463 (2019).

[76] L. Tonks, The Complete Equation of State of One, Two and Three-Dimensional Gases of Hard Elastic Spheres, Phys. Rev. 50, 955 (1936).

[77] E. B. Saff and A. B. J. Kuijlaars, Distributing many points on a sphere, Math. Intell. 19, 5 (1997).

[78] J. K. Percus, Equilibrium state of a classical fluid of hard rods in an external field, J. Stat. Phys. 15, 505, (1976).

[79] J. L. Lebowitz and J. K. Percus, Kinetic equations and density expansions: exactly solvable one-dimensional system, Phys. Rev. 155, 122 (1967).

[80] J. Kethepalli, D. Bagchi, A. Dhar, M. Kulkarni and A. Kundu, Finite temperature equilibrium density profiles of integrable systems in confining potentials, Phys. Rev. E 107, 044101 (2023).

[81] X. Cao, V. B. Bulchandani and J. E. Moore, Incomplete thermalization from trap-induced integrability breaking: Lessons from classical hard rods, Phys. Rev. Lett. 120, 164101 (2018).

[82] M. Saffman, T. G. Walker, and K. Mølmer, Quantum information with Rydberg atoms, Rev. Mod. Phys. 82, 2313 (2010).

[83] A. Browaeys, D. Barredo and T. Lahaye, Experimental investigations of dipole–dipole interactions between a few Rydberg atoms, J. Phys. B: At. Mol. Opt. Phys. 49, 152001 (2016).

[84] A. Browaeys and T. Lahaye, Many-body physics with individually controlled Rydberg atoms, Nature Physics, 16, 132 (2020).

[85] I. Bloch, J. Dalibard and W. Zwerger, Many-body physics with ultracold gases, Rev. Mod. Phys. 80, 885 (2008).

[86] C. Gross and I. Bloch, Quantum simulations with ultracold atoms in optical lattices. Science, 357, 995 (2017).

[87] M. Chalony, J. Barré, B. Marcos, A. Olivetti and D. Wilkowski, Long-range one-dimensional gravitational-like interaction in a neutral atomic cold gas, Phys. Rev. A 87, 013401 (2013).

[88] J. Zhang, G. Pagano, P. W. Hess, A. Kyprinanids, P. Becker, H. Kalpan, A. V. Groshkov, Z. -X. Gong and C. Monroe, Observation of a many-body dynamical phase transition with a 53-qubit quantum simulator, Nature. 551, 601 (2017).

[89] J. M. Brown and A. Carrington, Rotational spectroscopy of diatomic molecules, Cambridge University Press, Cambridge, UK (2003).

[90] L. L. Yan, W. Wan, L. Chen, F. Zhou, S. J. Gong, X. Tong and M. Feng, Exploring structural phase transitions of ion crystals, Scientific reports, 6, 21547 (2016).

[91] M. Lu, N. Q. Burdick, S. H. Youn and B. L. Lev, Strongly dipolar Bose-Einstein condensate of Dysprosium, Phys. Rev. Lett. 107, 190401 (2011).

[92] A. Griesmaier, J. Werner, S. Hensler, J. Stuhler and T. Pfau, Bose-Einstein condensation of Chromium, Phys. Rev. Lett. 94, 160401 (2005).

[93] M. Fridman, R. Pugatch, M. Nixon, A.r A. Friesem and N. Davidson, Measuring maximal eigenvalue distribution of Wishart random matrices with coupled lasers, Phys. Rev. E 85, 020101(R) (2012).

[94] S. Giorgini, L. P. Pitaevskii and S. Stringari, Theory of ultracold atomic Fermi gases, Rev. Mod. Phys. 80, 1215 (2008).

[95] A. Griesmaier, J. Stuhler, T. Koch, M. Fattori, T. Pfau and S. Giovanazzi, Comparing contact and dipolar interactions in a Bose-Einstein condensate, Phys. Rev. Lett. 97, 250402 (2006).

[96] K. K. Ni, S. Ospelkaus, D. Wang, G. Quéméner, B. Neyenhuis, M. H. G. de Miranda, J. L. Bohn, J. Ye and D. S. Jin, Dipolar collisions of polar molecules in the quantum regime, Nature, 464, 1324 (2010).

[97] S. Agarwal, A. Dhar, M. Kulkarni, A. Kundu, S. N. Majumdar, D. Mukamel and G. Schehr, Harmonically confined particles with long-range repulsive interactions, Phys. Rev. Lett. 123, 100603 (2019).

[98] S. Santra, J. Kethepalli, S. Agarwal, A. Dhar, M. Kulkarni and A. Kundu, Gap statistics for confined particles with power-law interactions, Phys. Rev. Lett. 128, 170603 (2022).

[99] A. Kumar, M. Kulkarni and A. Kundu, Particles confined in arbitrary potentials with a class of finite-range repulsive interactions, Phys. Rev. E 102, 032128 (2020).

[100] A. Pandey, A. Kumar and S. Puri, Finite-range Coulomb gas models. I. Some analytical results, Phys. Rev. E 101, 022217 (2020).

[101] R. Allez, J. P. Bouchaud and A. Guionnet, Invariant Beta ensembles and the Gauss-Wigner crossover, Phys. Rev. Lett. 109, 094102 (2012).

[102] R. Allez, J. P. Bouchaud, S. N. Majumdar and P. Vivo, Invariant β-Wishart ensembles, crossover densities and asymptotic corrections to the Marčenko–Pastur law, J. Phys. A: Math. Theor. 46, 015001, (2013).

[103] S. Santra and A. Kundu, Crossover in densities of confined particles with finite range of interaction, J. Phys. A: Math. Theor. 57, 245003 (2024).

[104] D. Bagchi, Thermal transport in the Fermi-Pasta-Ulam model with long-range interactions, Phys. Rev. E 95, 032102 (2017).

[105] D. Bagchi, Heat transport in long-ranged Fermi-Pasta-Ulam-Tsingou-type models, Phys. Rev. E 104, 054108 (2021).

[106] F. Andreucci, S. Lepri, S. Ruffo and A. Trombettoni, Nonequilibrium steady states of long-range coupled harmonic chains, Phys. Rev. E 108, 024115 (2023).

[107] R. Dandekar, P. L. Krapivsky and K. Mallick, Dynamical fluctuations in the Riesz gas, Phys. Rev. E 107, 044129 (2023).

[108] L. Touzo, P. L. Doussal and G. Schehr, Interacting, running and tumbling: The active Dyson Brownian motion, Euro. Phys. Lett. 142, 61004 (2023).

[109] L. Touzo, P. L. Doussal and G. Schehr, Fluctuations in the active Dyson Brownian motion and the overdamped Calogero-Moser model, Phys. Rev. E 109, 014136 (2024).

[110] A. Flack, P. L. Doussal, S. N. Majumdar and G. Schehr, Out-of-equilibrium dynamics of repulsive ranked diffusions: The expanding crystal, Phys. Rev. E 107, 064105 (2023).

[111] F. J. Dyson, A Brownian-motion model for the eigenvalues of a random matrix, J. Math. Phys. 3, 1191 (1962).

[112] J. Bun, J. P. Bouchaud, S. N. Majumdar, and M. Potters, Instanton approach to large N Harish-Chandra-Itzykson-Zuber integrals, Phys. Rev. Lett. 113, 070201 (2014).

[113] J. Gustavsson, Gaussian fluctuations of eigenvalues in the GUE, Annales de l' Institut Henri Poincare (B) Probability and Statistics, 41, 151 (2005).

[114] R. D. H. Rojas, C. S. H. Calva and I. P. Castillo, Universal behavior of the full particle statistics of one-dimensional Coulomb gases with an arbitrary external potential, Phys. Rev. E 98, 020104(R) (2018).

[115] J. Kethepalli, M. Kulkarni, A. Kundu, S. N. Majumdar, D. Mukamel and G. Schehr, Harmonically confined long-ranged interacting gas in the presence of a hard wall, J. Stat. Mech. 2021, 103209 (2021).

[116] J. Kethepalli, M. Kulkarni, A. Kundu, S. N. Majumdar, D. Mukamel G. Schehr, Edge fluctuations and third-order phase transition in harmonically confined long-range systems, J. Stat. Mech. 2022, 033203 (2022).

[117] J. Kethepalli, M. Kulkarni, A. Kundu, S. N. Majumdar, D. Mukamel, G. Schehr, Full counting statistics of 1d short-range Riesz gases in confinement, arXiv:2403.18750.

[118] M. F. Parsons, F. Huber, A. Mazurenko, C. S. Chiu, W. Setiawan, K. W. Brown, S. Blatt and M. Greiner, Site-resolved imaging of fermionic ^{6}Li in an optical lattice, Phys. Rev. Lett. 114, 213002 (2015).

[119] L. W. Cheuk, M. A. Nichols, M. Okan, T. Gersdorf, V. V. Ramasesh, W. S. Bakr, T. Lompe and M. W. Zwierlein, Quantum-gas microscope for fermionic atoms, Phys. Rev. Lett. 114, 193001 (2015).

[120] E. Haller, J. Hudson, A. Kelly, D. A. Cotta, B. Peaudecerf, G. D. Bruce and S. Kuhr, Single-atom imaging of fermions in a quantum-gas microscope, Nature Physics, 11, 738 (2015).

[121] C. Gross and W. S. Bakr, Quantum gas microscopy for single atom and spin detection, Nature Physics, 17, 1316 (2021).

[122] S. Kuhr, Quantum-gas microscopes: a new tool for cold-atom quantum simulators, National Science Review, 3, 170 (2016).

[123] C. G. Broyden, The convergence of a class of double-rank minimization algorithms 1. General considerations, IMA J. Appl. Math. 6, 76 (1970).

[124] R. Fletcher, A new approach to variable metric algorithms, The Computer Journal, 13, 317 (1970).

[125] R. J. Duffin, Yukawa potential theory, J. Math. Anal. Appl. 35, 105–130 (1971).

[126] N. W. Ashcroft and N. D. Mermin, Solid State Physics, Brooks/Cole, Belmont, CA, USA (1976).

[127] D. C. Brydges, A rigorous approach to Debye screening in dilute classical Coulomb systems, Comm. Math. Phys. 58, 313 (1978).

[128] D. C. Brydges, and P. Federbush, Debye screening, Comm. Math. Phys. 73, 197 (1980).

[129] J. P. Hansen and I. R. McDonald, Theory of Simple Liquids: With Applications to Soft Matter, Academic Press, Amsterdam, Netherlands (2013).

[130] E. Sandier, S. Serfaty, 2D Coulomb gases and the renormalized energy, arXiv:1201.3503 (2013).

[131] S. Serfaty, Microscopic description of log and Coulomb gases, arXiv:1709.04089 (2017).

[132] R. Bauerschmidt, P. Bourgade, M. Nikula and H. T. Yau, Local density for two-dimensional one-component plasma, Commun. Math. Phys. 356, 189 (2017).

[133] L. Bétermin, L. Šamaj, I. Travěnec, Three-dimensional lattice ground states for Riesz and Lennard-Jones type energies, Stud. Appl. Math. 150, 69 (2022).

[134] I. Kylänpää, F. Cavaliere, N. T. Ziani, M. Sassetti and E. Räsänen, Thermal effects on the Wigner localization and Friedel oscillations in many-electron nanowires, Phys. Rev. B 94, 115417 (2016).

[135] N. T. Ziani, F. Cavaliere, K. G. Becerra and M. Sassetti, A short review of one-dimensional Wigner crystallization, Crystals, 11, 20 (2021).

[136] S. Ramaswamy, The mechanics and statistics of active matter, Annu. Rev. Condens. Matter Phys. 1, 323 (2010).

[137] J. Tailleur and M. E. Cates, Statistical mechanics of interacting run-and-tumble bacteria, Phys. Rev. Lett. 100, 218103 (2008).

[138] K. Malakar, V. Jemseena, A. Kundu, V. K. Krishnamurthy, S. Sabhapandit, S. N. Majumdar, S. Redner and A. Dhar, Steady state, relaxation and first-passage properties of a run-and-tumble particle in one-dimension, J. Stat. Mech. 2018, 043215 (2018).

[139] A. Dhar, A. Kundu, S. N. Majumdar, S. Sabhapandit and G. Schehr, Run-and-tumble particle in one-dimensional confining potentials: Steady-state, relaxation, and first-passage properties, Phys. Rev. E 99, 032132 (2019).

[140] U. Basu, S. N. Majumdar, A. Rosso, S. Sabhapandit and G. Schehr, Exact stationary state of a run-and-tumble particle with three internal states in a harmonic trap, J. Phys. A: Math. Theor. 53, 09LT01 (2020).

[141] Francesco Mori, Pierre Le Doussal, Satya N. Majumdar and Grégory Schehr, Universal survival probability for a d-dimensional run-and-tumble particle, Phys. Rev. Lett. 124, 090603 (2020).

[142] P. Singh and S. Santra and A. Kundu, Extremal statistics of a one-dimensional run and tumble particle with an absorbing wall, J. Phys. A: Math. Theor. 55, 465004 (2022).

[143] A. K. Hartmann, S. N. Majumdar, H. Schawe and G. Schehr, The convex hull of the run-and-tumble particle in a plane, J. Stat. Mech. 2020, 053401 (2020).

[144] P. Singh, A. Kundu, S. N. Majumdar and H. Schawe, Mean area of the convex hull of a run and tumble particle in two dimensions, J. Phys. A: Math. Theor. 55 225001 (2022).

[145] S. Chandrasekhar, Stochastic problems in physics and astronomy, Rev. Mod. Phys. 15, 1 (1943).

[146] J. R. Furling, S. N. Majumdar and A.Comtet, Convex hull of N planar Brownian motions: Exact results and an application to Ecology, Phys. Rev. Lett. 103, 140602 (2009).

[147] T. Vicsek, A. Czirók, E. Ben-Jacob, I. Cohen and O. Shochet, Novel type of phase transition in a system of self-driven particles, Phys. Rev. Lett. 75, 1226 (1995).

[148] S. Hubbard, P. Babak, S. T. Sigurdsson and K. G. Magnússon, A model of the formation of fish schools and migrations of fish, Ecol. Model. 174, 359 (2004).

[149] J. Toner, Y. Tu and S. Ramaswamy, Hydrodynamics and phases of flocks, Annals of Physics, 318, 170 (2005).

[150] A. B. Slowman, M. R. Evans and R. A. Blythe, Jamming and attraction of interacting run-and-tumble random walkers, Phys. Rev. Lett. 116, 218101 (2016).

[151] A.P. Solon, Y. Fily, A. Baskaran, M. E. Cates, Y. Kafri, M. Kardar and J. Tailleur, Pressure is not a state function for generic active fluids, Nature physics, 11, 673 (2015).

[152] Y. Fily and M. C. Marchetti, Athermal phase separation of self-propelled particles with no alignment, Phys. Rev. Lett. 108, 235702 (2012).

[153] M. E. Cates and J. Tailleur, Motility-induced phase separation, Annu. Rev. Condens. Matter Phys. 6, 219 (2015).

[154] I. Mukherjee and A. Raghu and P. K. Mohanty, Nonexistence of motility induced phase separation transition in one dimension, SciPost Phys. 14, 165 (2023).

[155] G. Thompson, J. Tailleur, M. E. Cates and R. A. Blythe, Lattice models of nonequilibrium bacterial dynamics, J. Stat. Mech. 2011, P02029 (2011).

[156] S. Put, J. Berx and C. Vanderzande, Non-gaussian anomalous dynamics in systems of interacting run-and-tumble particles, J. Stat. Mech. 2019, 123205 (2019).

[157] A. Das, A. Dhar and A. Kundu, Gap statistics of two interacting run and tumble particles in one dimension, J. Phys. A: Math. Theor. 53, 345003 (2020).

[158] R. Dandekar, S. Chakraborti and R. Rajesh, Hard core run and tumble particles on a one-dimensional lattice, Phys. Rev. E 102, 062111 (2020).

[159] P. Singh and A. Kundu, Crossover behaviours exhibited by fluctuations and correlations in a chain of active particles, J. Phys. A: Math. Theor. 54, 305001 (2021).

[160] M. J. Metson, M. R. Evans and R. A. Blythe, Tuning attraction and repulsion between active particles through persistence, Euro Phys. Lett. 141, 41001 (2023).

[161] M. J. Metson, M. R. Evans and R. A. Blythe, From a microscopic solution to a continuum description of active particles with a recoil interaction in one dimension, Phys. Rev. E 107, 044134 (2023).

[162] S. Santra, P. Singh and A. Kundu, Tracer dynamics in the active random average process, J. Stat. Mech. 2024, 063204 (2024).

[163] S. Paul, A. Dhar and D. Chaudhuri, Dynamical crossovers and correlations in a harmonic chain of active particles, arXiv:2402.11358 (2024).

[164] R. Mukherjee, S. Saha, T. Sadhu, A. Dhar and S. Sabhapandit, Hydrodynamics of a hard-core non-polar active lattice gas, arXiv:2405.19984 (2024).

[165] H. Spohn, Exact solutions for KPZ-type growth processes, random matrices, and equilibrium shapes of crystals, Physica A. 369, 71 (2005).

[166] F. A. Lindemann, The calculation of molecular vibration frequencies, Phys. Z. 11, 609 (1910).

[167] L. touzo, P. L. Doussal and G. Schehr, In preparation.

[168] S. Ahmed, M. Bruschi, F. Calogero, M. A. Olshanetsky and A. M. Perelomov, Properties of the zeros of the classical polynomials and of the Bessel functions, Nuovo Cimento B 49, 173 (1979).

[169] D. H. E. Dubin, Minimum energy state of the one-dimensional Coulomb chain, Phys. Rev. E 55, 4017 (1997).

[170] C. W. J. Beenakker, Pair correlation function of the one-dimensional Riesz gas, Phys. Rev. R. 5, 013152 (2023).

[171] J. C. Butcher, Numerical Methods for Ordinary Differential Equations, Wiley, 2008.

Publications

- **List of publications included in the thesis:**

1. Saikat Santra, Jitendra Kethepalli, Sanaa Agarwal, Abhishek Dhar, Manas Kulkarni and Anupam Kundu, Gap statistics for confined particles with power-law interactions, Phys. Rev. Lett. 128, 170603 (2022).

2. Saikat Santra and Anupam Kundu, Crossover in densities of confined particles with finite range of interaction, J. Phys. A: Math. Theor. 57, 245003 (2024).

3. Saikat Santra, Léo Touzo, Chandan Dasgupta, Abhishek Dhar, Suman Dutta, Anupam Kundu, Pierre Le Doussal, Grégory Schehr and Prashant Singh, Crystal to liquid cross-over in the active Calogero-Moser model, arXiv:2411.13478 (2024).

- **List of publications not included in the thesis:**

1. Saikat Santra, Prashant Singh and Anupam Kundu, Tracer dynamics in the active random average process, J. Stat. Mech. 063204 (2024).

2. Saikat Santra and Prashant Singh, Exact fluctuation and long-range correlations in a single-file model under resetting, Phys. Rev. E 109, 034123 (2024).

3. Prashant Singh, Saikat Santra and Anupam Kundu, Extremal statistics of a one-dimensional run and tumble particle with an absorbing wall, J. Phys. A: Math. Theor.

55 465004 (2022).

4. Saikat Santra, Adhip Agarwala and Subhro Bhattacharjee, Statistics-tuned entanglement of the boundary modes in coupled Su-Schrieffer-Heeger chains, Phys. Rev. B 103, 195134 (2021).